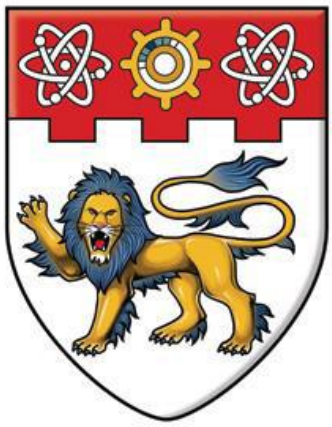

NANYANG TECHNOLOGICAL UNIVERSITY

MODELLING OF SAW STRUCTURES AND DESIGN OF SAW BIOSENSOR CIRCUITS AND DEVICES

RAHUL KISHOR

SCHOOL OF ELECTRICAL & ELECTRONIC ENGINEERING

2013

MODELLING OF SAW STRUCTURES AND DESIGN OF SAW BIOSENSOR CIRCUITS AND DEVICES

RAHUL KISHOR

School of Electrical & Electronic Engineering

A thesis submitted to the Nanyang Technological University in partial fulfilment of the requirement for the degree of Master of Engineering

2013

Acknowledgements

As I ponder over my research work for the past 2 years, it does not take me much time to realise that this dissertation materialised mainly due to the immense support and guidance of many individuals.

First, my sincere gratitude towards my supervisor Dr. Zheng Yuanjin for reposing trust in me, willing to introduce me to various multidisciplinary works and guiding me throughout my research work. His friendly attitude has been a very strong support for me to work with him. This work would not have been possible without his guidance and encouragement.

I gratefully acknowledge my co-supervisor Dr. Wang Zhenfeng and the project mates especially Seah Daphne at Singapore Institute of Manufacturing Technology (SIMTech-A*STAR) for their unwavering support and guidance, for all the useful discussions and assistance with the fabrication of SAW devices and microfluidic channels.

The technicians in VIRTUS IC Design Centre of Excellence, IC design I-II and VLSI lab are also to be acknowledged for their technical assistance and facilitation of the work environment. I would also like to thank the Economic Development Board, Singapore for providing me the IC design Postgraduate Scholarship (ICPS) to fund my study at Nanyang Technological University.

I would also like to thank my parents and my family for always being there to support me. Last but not the least; I would like to express my sincere appreciation to those, especially the postgraduate students of the circuits and systems division, who have helped me in one way or the other with my project.

Table of Contents

Summary

In this thesis, we focus upon the implementation of a biosensor and micropump using surface acoustic wave (SAW) technique. The integrated readout circuit simulation uses the electrical equivalent model for the SAW, designed using ANSYS finite element method (FEM). A micropump module using the SAW streaming effect is designed and fabricated. The two modules forms the most important sub-blocks in developing an acoustic microfluidic platform for diagnostic devices.

The biosensor consists of antibodies adhered to the surface of the transducers, which transduces a biological signal (binding of the antigen) into quantifiable electrical signals. The surface acoustic wave generated by the piezoelectric material causes this transduction. The SAW sensor has an input metal electrode known as inter-digital electrode (IDT), a sensing material and an output IDT on the piezoelectric substrate. The input IDT generates acoustic wave that travels through the piezoelectric substrate coated with the biological sensing material towards the output IDT. A change in the mass density of the film caused due to the interaction of the entity under analysis on the sensing surface changes the SAW velocity. The SAW readout circuit indirectly measures the change in the SAW velocity caused due to the biological binding event. Any change in the acoustic velocity, shifts the resonant frequency of the resonator. The subsequent circuits detect this change in the resonant frequency. SAW devices are sensitive to temperature changes. A reference SAW device compensates for the drifts due to temperature fluctuations. The difference frequency from a mixer stage (with the active and the reference SAW device as inputs) filters the frequency shifts due to temperature changes. The difference frequency holds the information of the biological binding event. A low pass filter selects the

difference frequency from the mixer output. A comparator converts the sinusoidal signal into square wave before applying to a frequency counter.

The coupling of the acoustic wave into the fluid causes fluid motion. SAW micropumps works on this principle. The microchannel material, polydimethylsiloxane (PDMS) attenuates the acoustic wave. Apart from it, many factors like the SAW device geometry, metal pattern and frequency also influence the acoustic wave generation. The simulation, fabrication and experiments of the SAW micropump were carried out.

List of Figures

List of Tables

Abbreviations

BAW- bulk acoustic wave

CM- equivalent circuit model

COM- coupling of modes

DFT-discrete Fourier transform

DNA- deoxyribonucleic acid

DOF- degree of freedom

EHD- electrohydrodynamic

EIA- enzyme immunoassay

ELISA- enzyme linked immunosorbent assay

ELFA- enzyme linked fluorescent assay

EO- electroosmotic

FEM- finite element method

GECBB- genetically engineered cell-based biosensor

GUI- graphical user interface

IDT- interdigital transducer

$LiNbO_3$ - lithium niobate

$LiTaO_3$ - lithium tantalate

LOC- lab on chip

LW- love wave

OTS- octadecyltrichlorosilane

PCR- polymerase chain reaction

PDMS- polydimethylsiloxane

PMMA- polymethylmethacrylate

PSS- periodic steady state

RSAW- Rayleigh SAW

SAW- surface acoustic wave

SH-SAW - shear horizontal surface acoustic wave

SPR- surface plasmon resonance

STW- surface transverse wave

Chapter 1 Introduction

The thesis is devoted towards a single-cartridge implementation of sensing and control functions using surface acoustic wave (SAW) technology. Section 1.1 outlines the motivation for the research. Section 1.2 describes the research objective. Section 1.3 highlights the research contribution of the author towards meeting the objectives. Finally, Section 1.4 provides a brief description of the thesis.

1.1 Motivation

Lab-on-chip(LOC) devices which consists of decentralizing lab testing down to chip format, is one of the most promising solution to improve the global health [1]. In many parts of the world, even though they have the poor healthcare facilities and drugs to treat various diseases, they still lack the diagnostic devices. However, the LOC systems have extremely difficult design criteria some of them being low cost, absence of trained personnel's, lack of electricity and transportation and storage of reagents in unrefrigerated conditions with improper handling. The last two decades witnessed a lot of research in implementing various microfluidic cells for fluid pumping, mixing, separation and concentration. There are many variants of each component available. For example, micropumps of various technologies like the centrifugal, electrohydrodynamic, electro osmotic, magnetohydrodynamic, acoustic/ultrasonic and many more are developed [2]. Instead of building each component, it is highly important to build an integrated microfluidic platform. Hence, rather than working on discrete components, building microfluidic applications requires an easy to operate and integrated microfluidic platform. Developing various applications using microfluidics from scratch incurs significant costs and time at a high economic risk. For commercialization of LOC systems, it requires a standardized platform [3]. Paralleling to the integrated circuits domain, were there are

well-matured designs and processes, a dedicated platform is necessary. To develop a diagnostics device for an application, the platform user should be easily able to integrate various cells. Various platforms are available with many advantages and disadvantages. Among the many techniques, SAW is particularly attractive. This is mainly due to its unique capability to control most of the important microfluidic functionalities like mixing, separation, pumping and pre-concentration required for a microfluidic platform. Hence, the single SAW device can perform all these functionalities which were performed by different modules. SAW as a biosensor has unique advantages over the optical sensing methods, which needs bulky and expensive off-chip components. Thus, the SAW driven microfluidic platform reduces the required components, simplifies the overall design and thereby reduces the overall cost. This provides the motivation for building a SAW based microfluidic platform.

1.2 Research objective

Today there are many number of microfluidic components following different principles, but due to difficulties involved in integration only a very few can be used to build a platform. The SAW based approach owing to its ability to manipulate fluids and sense the biomolecular interaction, is really a potential area for developing a microfluidic platform. Even though there are individual modules available for SAW manipulations, very little research is done to integrate these various components. Thus, we focus on developing a SAW based microfluidic platform on a single substrate. To achieve this objective, we first concentrate on individual SAW modules. Thus, this thesis focuses on two of the important SAW components- 1) SAW Biosensors and 2) SAW micropumps. The research objectives are:

- Derive an equivalent electrical model of the SAW device to build up the integrated readout circuits. This requires a modelling and FEM simulation of the device, to derive the parameters for the equivalent electrical model.
- SAW micropump involves fluidic actuation through closed microchannels. The microchannel materials will attenuate the acoustic waves. Hence, it requires a thorough analysis of the effect of the acoustic wave on travelling through these microchannels.
- Study the effect of SAW pumping on a microdroplet by theoretical analysis and experimental observations.

1.3 Research focus

The current work is on surface acoustic wave research with application to sensors and microfluidic pumps. The future goal is to integrate the sensing and pumping on a common substrate. Towards this, we follow a comprehensive design, modelling and experimental validation approach. Due to the multi-disciplinary fields involved, for this thesis the focus is upon two areas 1) modelling of SAW and design of readout circuits for biosensor, and 2) SAW micropump analysis and design.

Most of the literature available on SAW biosensor readout circuits has very limited explanation about the SAW circuit models. Certain works have used analytical models to solve the equivalent circuit parameters. These models however, discards many second order effects (e.g. bulk wave effects, reflections) Here, the focus is on making use of the commercial Finite element method (FEM) software ANSYS[4] to model the SAW resonator and extract the parameters after performing the harmonic simulation. The ANSYS model can represent even the second order effects like reflections present in the

SAW device. ANSYS is used to design the device parameters- exact inter-digital electrode (IDT)/reflectors width and spacing required. The integrated circuit simulation uses this SAW model. Furthermore, the frequency shift with respect to mass changes is simulated.

FEM was used in the past for modelling periodic structures and simple devices with few IDT electrodes [5]. However, these days with improved computational resources at lower cost, prompts the need to take advantage of whole structure simulation using FEM, which considers the second order effects. The transient simulation performs velocity corrections and curve fitting places the IDT's in the correct position for maximum coupling.

ANSYS transient simulation analyzes the acoustic energy transferred to the fluid by different SAW structures. Delay lines with varied number of IDT pairs, frequency and IDT designs ($\lambda/4$, $\lambda/8$) to account for finger reflections and focussed IDT structures for efficient fluidic manipulations are simulated. The primary aim of the micropump is to design structures to transfer maximum energy to the fluid. The microchannel material attenuates the acoustic energy. Hence, the effect of acoustic attenuation of the microchannel materials is studied. FEM Analysis is done to study the effect channel length, height and frequency of acoustic wave on the acoustic attenuation. The results, along with modified IDT designs can help to deliver maximum energy to liquid and thus create better fluidic manipulations using acoustics. Different IDT structures are fabricated, characterized and experimentally observed in studying the acoustic micropumping phenomenon.

1.4 Organization of the thesis

The thesis consists of six chapters with the organization as follows:

1 Chapter 1 is a preamble of the work, providing the introduction and motivation behind the thesis, along with the major contribution and thesis.

2 Chapter 2 presents a comprehensive literature review on the different kinds of biosensors, its issues and the advantages of the SAW biosensing system. It also presents the different micropump techniques available and highlights the advantages of the acousto-fluidic pumps over other techniques.

3 Chapter 3 involves the device modelling and simulation, which involves parameter extraction of lumped circuit models from ANSYS.

4 Chapter 4 presents the SAW readout circuit principle, the architecture and the design specifications. The cadence simulation results obtained will be presented.

5 Chapter 5 covers the SAW micropump design, fabrication and experimental results. An analysis of the acoustic attenuation of PDMS microchannels is also studied.

6 Chapter 6 presents the conclusion of this thesis, and recommendations for future work. The thesis ends with the bibliography section.

Chapter 2 Literature Review

2.1 Conventional methods for molecular detection

Typical approaches for detecting and recognizing molecules use specific microbiological and biochemical identifications. Fig 1 shows the conventional approaches.

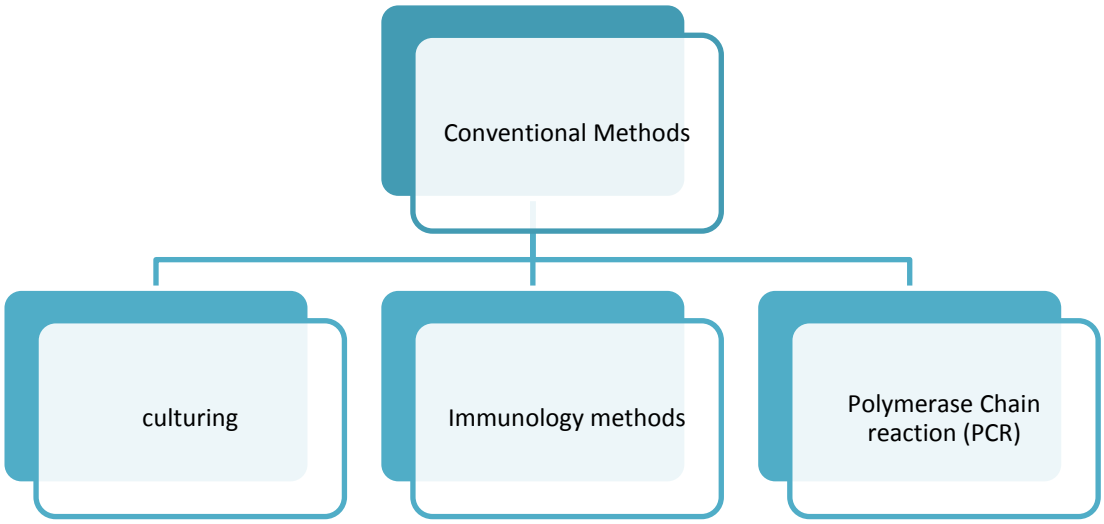

Figure 1: Conventional methods for molecular detection

Culturing remains the most consistent and precise method for detecting pathogens. This involves strengthening the signal by growing a colony of cells from a single cell. Due to slow growth rate process, it takes several days to get the results. For instance, L.Monoctyogens need 7 days to produce results [6]. However, certain bacteria strains enter an inactive state and hence cannot be cultured. This may cause an underestimation of the actual pathogen concentration. Thus, manual labour and time delay for obtaining results sets a major drawback for culturing techniques. This is not acceptable for many industrial applications, especially in food sector. The immunological methods depend on the affinity of the antibodies (e.g. monoclonal, polyclonal and recombinant) to bind to the

antigens. These days there are a variety of immunoassays available and this has fostered immunology detection to a highly reliable and sensitive form of detection methodology. Some of the immunological techniques are enzyme immunoassay (EIA), enzyme linked immunosorbent assay (ELISA), flow injection immunoassay and enzyme linked fluorescent assay (ELFA) and immunomagnetic separation. However, these methods fail to meet real time detection of microorganisms. Also, non-specific binding and difficulty in identifying specific antibody to a pathogen are the common problems encountered in these kind of assays[7].With the advent of polymerase chain reaction (PCR), it became possible to detect a single bacterium. This method is an in-vitro technique for enzymatic amplification of target nucleic acid sequences using a specific pair of primers and a heat-stable deoxyribonucleic acid (DNA) polymerase. This is an extremely sensitive technique, which can perform amplification beginning with a single copy of DNA, thus this method has the capability to identify a single bacteria. The amplification of the target rather than the signal reduces the number of false positives and thus makes the method more reliable. However, the method is very expensive and requires skilled personnel's to conduct the tests. Thus, the traditional methods have the problems, which restrict its usage as a point-of-care device. This fosters the need to develop a technology that should be sensitive, specific, reliable and rapid also at the same time simple to operate. In addition, it should be capable for an in situ real-time monitoring at a low cost. Biosensor satisfies all the above-mentioned requirements and hence suitable for a point-of-care device. Table 2-1, provides a comparison of the above mentioned detection techniques.

Detection method	**Culturing [8]**	**Immunology based methods [8]**	**PCR [8]**	**Biosensors [9]**
Sensitivity (CFU/ml)	1	1000	1 (real time)	100

*CFU- colony forming unit				
Specificity	High	Relatively low(depends on the affinity of antibody to an antigen)	High (amplifies target rather than the signal)	High
Response time	7-10 days for confirmation	Minutes	Hours	Minutes
Versatility	Bacteria, Virus	Proteins	DNA	Virus, DNA, Proteins, Bacteria, Spores
Size	Laboratory	Laboratory	Tabletop	Handheld
Ease of use	Extensive training, additional reagents	Extensive training, additional reagents	Careful sample preparation, extensive training and reagents	Simple, no additional reagents
Cost per test	$50- $500	$10-$50	$50- $500	< $50

Table 2-1: Comparison of different detection methods

2.2 Introduction to biosensors.

A biosensor is an analytical device, which converts a biological response into an electrical signal. Fundamentally it comprises of three major constituents: 1)the biomarker- responsible for identifying the target analyte, 2) the transducer- to transform the biological response into a quantifiable format and 3) a display or readout circuitry to inform the end-user. Fig 2 shows the schematic representation of a biosensor. The bioreceptor also known as a biomarker layer is responsible for identifying the analyte of interest from a sample, which comprises of other molecules and then produces a corresponding response. The transducer transforms the biological response generated into an electrical output. The electrical circuitry connected to the output of the transducer processes the signal into a format, which can be finally recorded, displayed and analyzed.

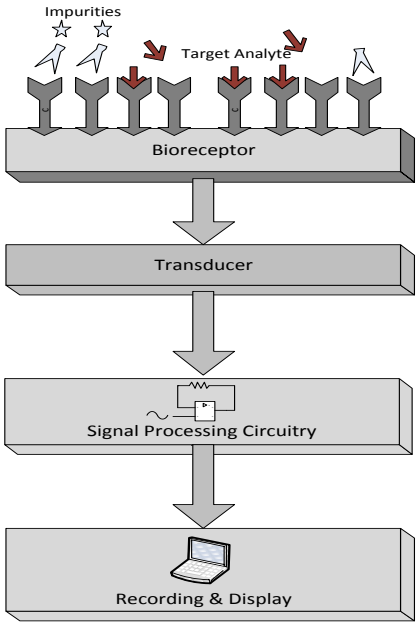

Figure 2: Biosensor: A conceptual illustration

2.3 Classification of biosensors

The bioreceptor constituent or their transduction phenomenon classifies the biosensors.

2.3.1 Bioreceptor

Bioreceptor is a biomolecule that recognizes a target molecule using a biochemical reaction. It is the basis for the sensitivity and specificity of a biosensor. Modern biotechnological techniques can produce and even modify the bioreceptor molecules. Classifications of bioreceptor are as follows:

- Antibody/Antigen
- Enzymes
- Nucleic acid/ DNA
- Cellular structures/ Cell
- Biomimetic

2.3.1.1 Antibody bioreceptors

Antibodies are Y shaped protein released by the immune system against foreign objects. They have two binding sites at the tips, which form specific sites for the antigens to bind. Antibody structure consists of two long large heavy chains and two small light chains. The connection between them is through disulphide bonds. Although the basic structure of all antibodies are the same, a small region at the tip of the protein is extremely variable, thus creating millions of antibodies with different tip structures or antigen binding sites to exist [10]. Each of these variant antibodies binds to different targets or antigens. This unique property of the antibodies explains its utility in biosensors. Immunosensors are a class of biosensors, which incorporates the antibody (antigen) as the bioreceptor molecule.

2.3.1.2 Enzymes

Enzymes form a good bioreceptor due to its precise binding capabilities and ability to act as a catalytic in the biorecognition mechanisms. Enzyme-linked immunosorbent assay (ELISA) technique makes use of the enzymes catalytic property to attain lower detection limits. The enzyme loses its catalytic activity by denaturation and dissociation into its subunits. Exposing the enzymes to varying pH, chemicals and high temperature (above 60℃) affects the activity of the enzymes.

2.3.1.3 Nucleic Acids / DNA

Nucleic acid bioreceptor is a highly specific way of detecting molecules ranging from small organic molecules to viral particles. The unique characteristic of an organism's nucleic acid leads to high specificity for detection. In the process of binding, a single strand of DNA from a target organism matches with another strand of DNA adhered on the surface. The complementary base pairs would combine and thus confirm the identity

of the molecule. The base pairing between the strands: A (adenine) with T (thymine) and C (cytosine) with G (guanine) forms the basic detection principle. A target molecule with a certain nucleic acid base sequence is detected by synthesizing a complementary base pair known as a probe.

2.3.1.4 Cellular bioreceptors

In this biorecognition method, either the entire cell or a specific component in the cell can act as a biomarker by binding to the targets. The cells ability to identify and react to external factors makes them useful in biosensors. Some important characteristics of the cells makes them very attractive for biorecognition, they are:

- The diverse processes occurring within a cell generates signals for many interactions.
- It detects many unknown targets.
- The inherent signal amplification due to the cellular transduction phenomena ensures very low detection thresholds

However, they face certain challenges. The normal functioning of a cell requires a specific environmental condition. A significant drawback of the cellular recognition is a lower specificity due to generation of the same response for multiple biochemical pathways. The use of genetically engineered cell based biosensors (GECBB) circumvents the above-mentioned problem.

2.3.2 Transducer

The transducer has a major role for determining the sensitivity of a biosensor. However it doesn't influence the specificity which is mainly dealt by the biorecognition element [11]. These days many types of transducers develop. However, the most popular and common

methods are the optical, electrochemical and mass based transduction methods. Each of which can be further subdivided into different subclasses. Label and label-free methods forms another classification. Labels are additional reagents (like fluorescent dyes) which attach to the target or the probe molecule to increase the signal level for detection. Label–free methods are more preferable for hand held diagnostic devices, as it requires lesser reagents. Hence, the sensitivity of the device should be high for low-level signal generated by the label free methods.

2.3.2.1 Optical based sensors

The fundamental components include a source of light, a precise light beam generating components, a modulating agent, a sensing surface and detecting components. Optical device utilizes the evanescent wave to detect and measure the adsorbed molecular layer. Change in reflectivity, interference patterns, absorption or fluorescence are various ways to monitor optical signal changes. Different optical sensing formats rely on such fundamental property shifts. Some of them include total internal reflection fluorescence, surface plasmon resonance (SPR) etc.

Optical sensors are compact, prone to lesser noise effects and highly flexible. In addition, the distinctive feature about the optical sensing is its high sensitivity and hence uses very low amounts of reagents. Owing to the sensitivity, the surface plasmon resonance and fluorescence are the most generally used methods in optical detection.

Surface plasmon resonance (SPR):

Fig 3 shows the SPR principle. This method relies on the reflectance spectroscopy for detection. Charge density oscillations or plasmons are generated on the surface of a metal, when they are optically illuminated and this forms the fundamental sensing

phenomenon[12]. The presence of an interface formed by media having opposite dielectric constants gives rise to such charge wave resonance. Metal/dielectric forms such an interface, where the excited electrons in the metals create the plasmons. Conventional SPR makes use of either p-polarized or transverse mode (TM) wave, which travels through a prism and meets the metal surface at a specific angle. This creates a charged oscillation at the metal/ dielectric interface. Two methods followed for achieving resonance are –

- Varying the incident light frequency or wavelength by keeping the incident light angle fixed at or above the critical angle.
- Varying the incident angle by fixing the wavelength or frequency[13].

The occurrence of the resonance leads to an increase in the absorption of the incident light with a simultaneous decrease in the reflected light. This reduction in the reflected light is the basis for detection.

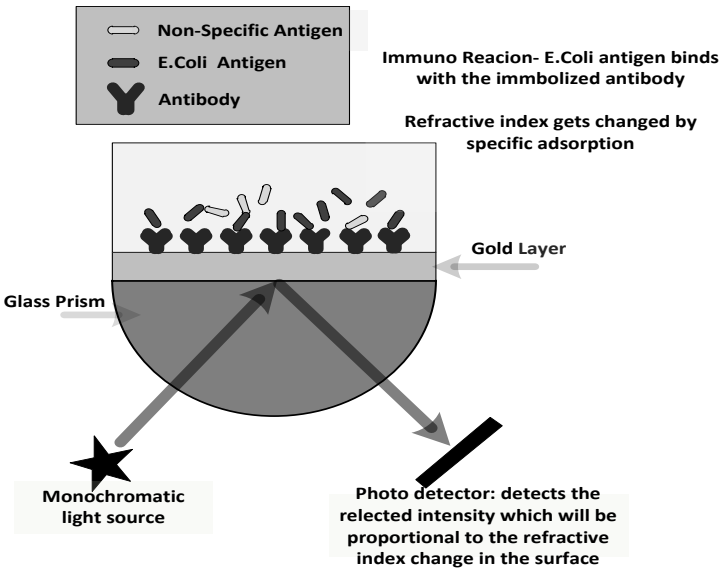

Figure 3: Surface plasmon resonance principle

2.3.2.2 Electrochemical sensors

Traditional biosensors employ the electrochemical transducers for sensing. The electrode or the buffer undergoes some electrical property shift due to the immunoreactions; this change in property is the underlying fundamental principle for sensing the target. A quantitative measurement of the analyte involves measuring the voltage, current or impedance changes caused by the immuno-interactions. Thus combining the specificity of the conventional immunoassay with the low cost and detection limits of the system offers great advantages for this method. However, it suffers from sensitivity and specificity limitations when compared to optical methods. Therefore, they require coupling with other biosensing techniques for enhanced detection. In immunoassays and immunosensors, as most antibodies and antigens are intrinsically unable to act as redox partners, there is a need for integration of labels to the immunocomplex to promote an electrochemical reaction. Conventional electrochemical transducers are either the potentiometric or the amperometric types.

In potentiometric-based detection, the transducer converts the biorecognition process into a voltage signal. A voltmeter with high impedance can measure the electrical potential difference between the two electrodes without drawing any current. However, they suffer from the disadvantage due to the very small change in the potential that arises out of the interaction between antibody and its antigen. More interference from the sample matrix renders the signal ineffective. Thus, the reliability and sensitivity of such sensors are limited.

In amperometric sensing, the oxidation or the reduction of an electro-active species at the electrode surface creates free electrons. Thus, a current linearly proportional to the concentration is generated and detected. These sensors have high sensitivity and provide

fast and reliable result. However, they suffer from poor selectivity, due to the inability to differentiate between species, which undergoes an electrochemical reaction step at the electrode.

2.3.2.3 Mass-sensitive sensors

Property changes due to mass changes are the basis behind this transduction. The excitation of a piezoelectric crystal with an electrical signal causes it to vibrate at a certain frequency, with the maximum response obtained when the electrical signal frequency matches the crystals resonant frequency. The resonance frequency depends on two factors mainly: the mass of the crystal and the applied electrical signal frequency. The increase in mass loading due to a biomolecular interaction gives rise to a proportional drift in the crystal resonant frequency. Circuits to detect such frequency deviation can provide a quantitative estimate of the target analyte mass. Quartz is the most commonly used piezoelectric substrate. The vibration modes classify the mass-sensitive sensors into surface acoustic wave (SAW) and bulk acoustic wave (BAW) sensors.

Mass loading on a piezoelectric sensor surface, due to the interaction of the deposited bioreceptor to the corresponding analyte molecule, causes a shift in the resonance frequency. The frequency drift increases with the squared resonant frequency. Thus, the response of mass sensitive devices improves with the operating frequency, for a given surface density [14]. Detection techniques for mass based sensing are relatively simple as it involves no complicated interface systems, economical and achieves high sensitivity and selectivity with a direct label-free analysis. However, apart from mass other external parameters also known as non-gravimetric effects influence the piezoelectric sensors. Table 2-2, provides a comparison of the various transducers mentioned above.

Transducer	Optical: Surface plasmon resonance [15]	Electrochemical: Amperometric [16]	Mass based: Surface acoustic wave [9]
Sensitivity (CFU/mL)	10^2-10^3	10^7	10^5
Specificity	High	Less	High
Size	Relatively bigger due to the optical setup (prism)	Smaller than the optical detection methods	Very small - Handheld
Cost	Expensive due to the optics involved	Low	Low
Response time	Minutes	Minutes	Minutes
Complexity	Optics involved in quite complex	Easy to use	Easy to use

Table 2-2: Comparison of various transducers

2.4 SAW biosensors

Acoustic microsensor in the widest sense describes significantly a wide variety of devices that uses the acoustic waves in its operating principle [13]. It differs based on the nature of wave propagation. These waves undergo changes when interacting with the surrounding medium. The sensing applications measures the acoustic or the electrical signals generated. A conventional acoustic wave sensor generates a standing wave by reflecting two opposite directed travelling waves, produced due to reflectors. The velocity of the acoustic wave and the dimension of the structures (defines wavelength) together, defines the frequency of the standing wave. SAW are electro-elastic waves with the energy concentrated within nanometre depths from the surface of piezoelectric substrates. The stress free conditions on the surface of a crystal gives rise to the surface acoustic modes. Commonly used piezoelectric materials for making SAW sensors are: Quartz, lithium niobate ($LiNbO_3$) or lithium tantalate ($LiTaO_3$). Metal electrodes in the form of inter-digitized fingers also called as inter-digital transducer (IDT) on top of the piezoelectric substrate is used for generating and detecting the acoustic waves [17].

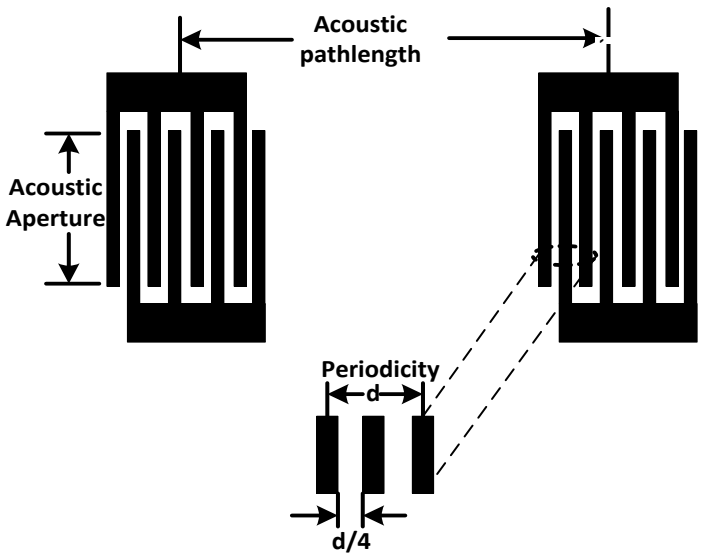

Figure 4: IDT used for acoustic wave excitation.

An IDT consists of a comb structures made most typically from a lithographically patterned thin film. Fig 4 shows the IDT for generating acoustic waves from electrical excitation. The individual electrodes are placed on the surface in an interleaved pattern. The IDT design involves metal lines which are thick enough thereby reducing the electrical resistance and thin to an extent that they do not create mechanical loading and thereby affecting the acoustic wave. Typically, the IDT's are made from aluminium. The IDT designs decide the resonant frequency, electrical impedance and bandwidth of the device. The application of a radio frequency voltage to an IDT excites it to generate an acoustic wave. The periodic variation of the input electrical signal excitation deforms the piezoelectric substrate at the same frequency, and thus the piezoelectric action gives rise to an acoustic wave. The velocity of the acoustic wave and the frequency of excitation define the wavelength of the acoustic wave. The velocity differs based on the mass loading. The periodicity of the transducer pattern (d in Fig 4) is set equal to the wavelength. Thus, the IDT finger spacing determines the center frequency:

$$f_0 = \frac{v}{d} \tag{2–1}$$

The bandwidth (BW) of the transducer is influenced by the number of IDT finger pairs and is related as

$BW \propto \frac{f_0}{N}$, where N corresponds to the number of finger pairs in an IDT.

The IDT pattern generates a broad continuum of shear transverse waves with the polarization confined to a horizontal and vertical plane to the substrate, as well as the waves travelling longitudinally. These waves propagate either within the surface or towards the bulk portion of the piezoelectric material. The modes generated is governed by factors such as the property of the piezoelectric material, its thickness, the angle of the crystal cut and even the device's dimensions[18].

One of the most important classifications of SAW sensors are based on the wave propagation modes. They are categorized as follows[19]: -

- Rayleigh type SAW devices
- Shear horizontal surface acoustic wave (SH-SAW)
- Love-wave devices

2.4.1 Rayleigh mode devices:

This is the most generally encountered mode of propagation of surface waves in the SAW based sensors. The Rayleigh mode consists of wave made of both the longitudinal and transverse motion that decreases exponentially in amplitude with increasing distance from the surface. The surface particles move in an ellipse in a plane normal to the surface and parallel to the direction of propagation. In this way, the acoustic energy is strongly confined to the surface of the device, regardless of the thickness of the complete substrate [20]. This brings in the sensitiveness of the device towards changes in mass, conductivity, pressure etc, as this creates changes in the wave properties. However, the

Rayleigh SAW (RSAW) devices suffer severe attenuation and high insertion losses when immersed in aqueous liquids. The normal component of the Rayleigh wave generates compressional waves which radiate into the liquid at a certain angle and causes high attenuation of the signal [21]. The SAW based microfluidic devices harness the dissipation of the wave in contact with liquid for processes like mixing, pumping etc. Hence, the RSAW is not suitable for liquid sensing. Instead, it finds application in gas detection and high frequency filters.

2.4.2 Shear horizontal surface acoustic wave (SH-SAW) or surface transverse wave (STW) devices

The Shear horizontal sensors, has the waves polarized in the horizontal direction and confined in a very thin volume from the surface. Metallic gratings are placed between the IDT's, which creates periodic disturbances for the propagating wave, this lowers the velocity of the surface wave and helps to confine the wave on the surface [22]. A transverse and parallel plane to the piezoelectric surface confines the particle displacement. Mass loading causes the reduction in the velocity and thus form a waveguide along the surface. These devices works in the frequency range of 30-300MHz. The transducer finger periodicity defines the wavelength and the velocity of the wave depends on the material forming the plate. As the wave is not attenuated by liquids, they find good applications in biosensors[23].

2.4.3 Love wave(LW) devices:

The love wave sensors also have their vibrations confined in a shear plane on the surface of the device; hence, it behaves similar to a SH-SAW sensor mentioned above. A thin film on the surface replaces the mass grating, which lowers the velocity. The gratings acts as waveguide and confines the wave to the surface. Materials like silicon dioxide or

polymethyl-methacrylate (PMMA) forms the thin waveguide layers. LW sensors are primarily used for liquid phase biosensing applications [24].

2.5 Micropumps

One of the most important features of a microfluidic system is to pump fluids controllably through the system against the resistance created by the connecting channels and various components like the mixer, filters and sensors. One classification is based on the manner in which the fluid flow and pressure are created [25]. They were either displacement or dynamic micropumps.

The set of moving boundaries in the displacement pump delivers pressure to the fluid, while the constant addition of energy to the fluid increases its momentum as in the case of a centrifugal pump or raises the pressure to pump the liquid (electroosmotic and electrohydrodynamic); this is the principle of a dynamic pump. The biggest challenge confronting all the actuation process is to surmount the large forces imparted by the surface and viscosity that restricts fluid movement at microfluidic level. At this small length scales the Reynolds number (ratio of the inertial to viscous force) is less than one. This makes the viscous force dominate and hence makes it difficult to drive the fluid. The acoustically driven microfluidics imparts an acoustic force to the fluid due to the processes of acoustic streaming and radiation pressure. This improves the flow velocity (a few cm/sec). The displacement pumps have complicated structures involving expensive mounting process. Moreover, they require large area to keep the elastic elements tractable. These drawbacks makes it less suitable for miniaturization[26].

As mentioned earlier, a general category of the dynamic micropumps based on the field that drives the fluid are electromagnetics or acoustics. The electromagnetic field imparts

momentum to the fluid. The electrohydrodynamic, electroosmotic and magneto hydrodynamic micropumps forms a classification for electromagnetics based micropump.

2.5.1 Electrohydrodynamic (EHD) pumps

This works on the influence of electrostatic fields in the ions present in the dielectric fluids. A force acts on the dielectric fluid when an electric field is given to the sample and it is given in Eq. 2-2 [27]

$$F = q_f E + P.\nabla E - \frac{1}{2}E^2\nabla\varepsilon + \nabla\left(\frac{1}{2}\rho\frac{\partial\varepsilon}{\partial\rho}E^2\right) \quad (2\text{–}2)$$

where, P is the polarization vector, q_f is the amount of free space charge, ε is the fluid permittivity and ρ is the fluid density. The first quantity, of the equation represents the Coulomb force, which is the strongest term, and it acts on the free charges. The remaining terms are the Kelvin polarization force, dielectric force acting on the liquid and electrostrictive force in the successive order. As defined in the equation, the liquid should have free space charge for the operation of the micropump. The fluid inhomogenities, dissociation or direct charge injection generates it. Two permeable conductors with contact directly to the fluid are required to pump the fluid. Electrochemical reaction occurs and it releases the ions into the fluid from the electrodes. A pressure gradient between the emitter and collector generates fluid motion. The direct dependence on the fluid property i.e. on the permittivity and conductivity restricts its applicability.

2.5.2 Electroosmotic (EO) micropumps

The electroosmosis or the electrokinetic pumping phenomenon pumps electrolyte solutions. In electroosmosis, an ionic solution moves relative to a solid boundary (channel wall) upon application of an electric field. The charges in the fluid attracting to the

charges formed in the channel wall surface create an electrical double layer. The applied electric field causes the motion of the charged species in the fluid as in Fig 5. These mobile ions drags the bulk liquid in the direction of the electric force[28].

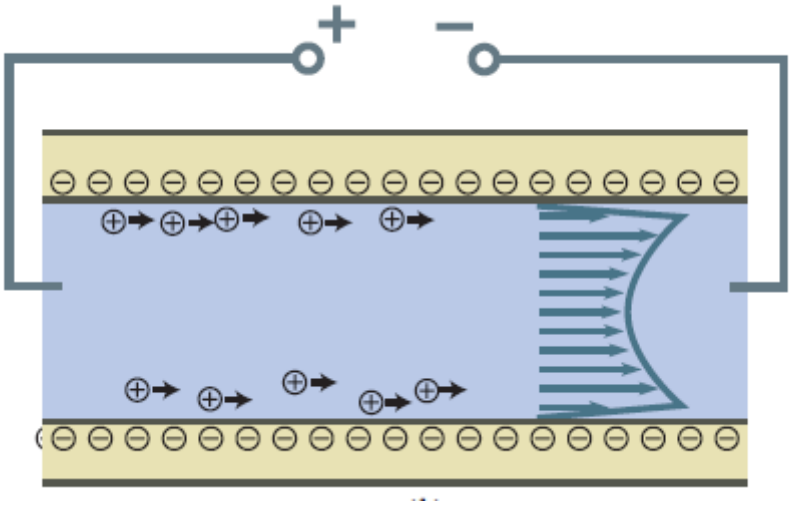

Figure 5: Electroosmotic flow- due to movement of the charged species in the liquid formed from the dielectric double layer [2]

The performance of the EO pumps depends on the 1) electric field applied, 2) solid surface charge density in contact with the fluid, 3) density of the ions and pH of the fluid.

2.5.3 Magnetohydrodynamic Pumps

These pumps (Fig 6) works on the principle of the flow generated due to Lorentz force exerted by the magnetic field and the current density produced due to the charged ions in the fluid. The maximum pressure in a rectangular channel is given by Eq.2-3 where J_x denotes the transverse current density and B_y corresponding to the magnetic flux density in the perpendicular direction.

$$\boldsymbol{P_{max} = J_x B_y L} \tag{2–3}$$

$$\boldsymbol{Q_{max} = J_x B_y \frac{\pi D_h^4}{128\mu}} \tag{2–4}$$

where l is the channel length and D_h being the hydraulic diameter[2].

The limitation imposed by this pumping technique is due to the maximum magnetic flux density possible (1T and 0.1T corresponding to miniature permanent magnets and electromagnetic coils respectively). As shown in Eq. 2-4, the dependence of the maximum flow rate to the fourth power of hydraulic diameter forms the challenge towards miniaturization. The thermal effects limit the current density.

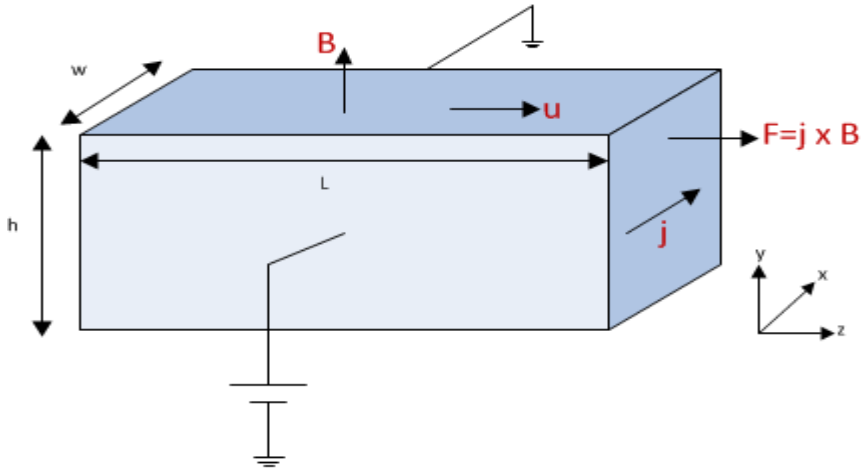

Figure 6: Schematic of magnetohydrodynamic pumps

2.5.4 Ultrasonic pumps

Conventional acoustically driven microfluidics was inferior to the electrokinetic devices. The ultrasonic waves with the bulk waves confined within the kilohertz frequency range were used for fluid pumps[29]. The significant drawbacks in the ultrasonic pumps are:

1. At such a lower frequency, the wavelength associated with the ultrasonic mechanism is larger (few mm) than the microfluidic channel length and target biomolecule.
2. Cost also comes into concern due to the use of piezoelectric materials.
3. Efficiency of the fluid-structure interactions are less.

4. Bulk acoustic wave excitation puts in stringent design consideration in mounting and application, to reduce losses or mode conversion.

2.5.5 SAW pumps

The pumps employing the surface acoustic wave has distinctive advantages: a simple structure without any moving parts, lower cost of fabrication, precise droplet controls using electronic control, high speed, programmability and the biggest advantage of, having no contacts of the electrodes with the liquid to be tested, compactness [30]- [31]. The Rayleigh wave mode in SAW is concentrated to the surface of the substrate. Due to this, the wave dispersion is very small compared to the bulk mode, thereby helping to drive the fluid consuming less power relative to other pumping methods. Thus, apart from just minimizing the microchannels and the components (like micropumps, micro reactors, micro separators etc); the SAW based microfluidics reduces the power consumption. The acoustic streaming generated due to the transfer of energy of the acoustic wave into the fluid is the driving force involved. Fig 7 shows schematically, the principle behind the acoustically induced streaming. As the SAW encounters the liquid at x=0, there is a very strong absorption of the wave into the fluid which is represented by the amplitude attenuation for x > 0. This creates a very small but finite pressure difference $2\Delta P$, which gives rise to a difference in the fluid mass density ($2\Delta\rho$) within the fluid. The pressure and density oscillate temporally and spatially with respect to their steady state values of P_0 and ρ_0 respectively. The existing pressure difference generates longitudinal waves at the surface and these waves' moves into the fluid. Due to the difference in the sound velocity in the substrate and liquid, the wave diffracts into the fluid at an angle θ_r. The angle is given by the famous Snell's law (in optics) given by Eq.2.5

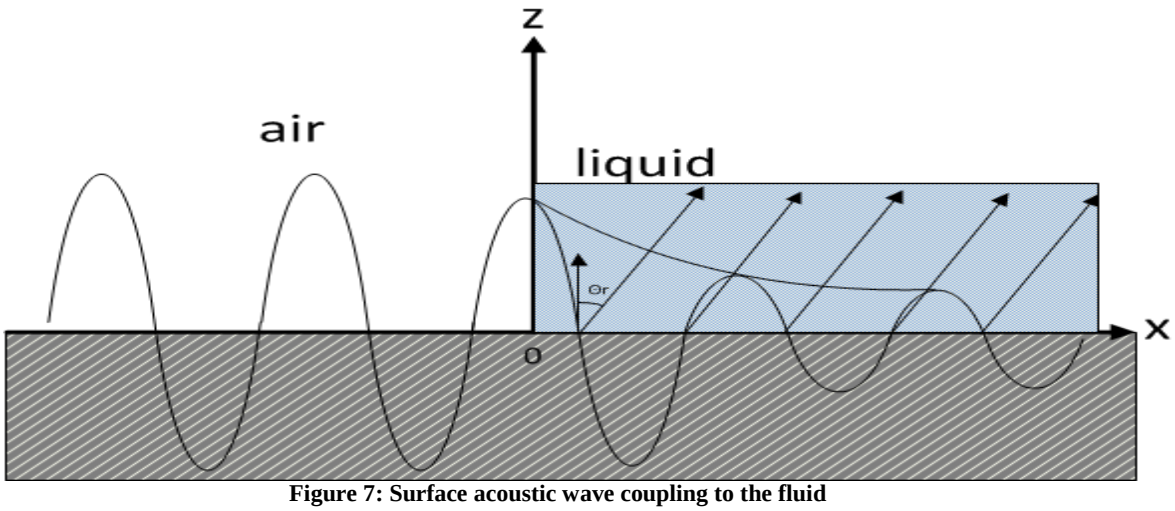

Figure 7: Surface acoustic wave coupling to the fluid

$$\theta_r = \arcsin(\frac{v_s}{v_f}) \quad (2–5)$$

where v_s and v_f denotes the velocities of the sound in the solid and the fluid medium respectively. This phenomenon is known acoustic streaming. Apart from it, the acoustic radiation pressure (P_s) is also generated and it is given by Eq.2.6.

$$\boldsymbol{P_s = \rho_0 v_s^2 \ \left(\frac{\Delta\rho}{\rho_0}\right)^2} \quad (2–6)$$

The radiation pressure acts in the direction of propagation of sound in the fluid medium. Hence, the above-mentioned two processes- acoustic streaming and radiation pressure deforms the droplet. The droplet deformation increases the contact angle with the surface and reduces the surface tension, which holds the droplet. At higher power the acoustic force overcomes the surface force and moves the droplet in the direction of the acoustic wave.[32].

Table 2-3 lists the different properties for various micropump technologies [2]. Surface acoustic wave micropump is a good fit for a point-of-care device (lower voltage, size and ability to work with most of the fluids).

Micropump	Electro hydrodynamic	Electroosmotic	Magneto hydrodynamic	SAW
Working fluid	Dielectric fluids	Wide range depends on ionic density and pH	Wide range depends on ionic density	Any fluids
Approximate size(mm^3)	10-250	100-1000	Depends on required magnetic field	5-10
Operating voltage (V)	40-600	40-1500	N/A (0.44T magnetic field)	30-40
Pressure difference(kPa)	0.25-0.4	100-10000	0.17	0.08
Flow rate(ml/min)	0.0001-10	5E-6-100	0.063	0.24
Reusable	No	No	No	Yes- no physical contacts with the liquid
Microfluidic applications	Continuous	Continuous	Continuous	Both droplet and continuous microfluidics are supported
Effects on fluid	Joule heating	Joule heating	Joule heating	Pulsed excitation- reduces fluid heating
Mixing	No	No	No	Yes, with mixing efficiency of >98% within 2 sec.

Table 2-3: Various micropump techniques

This chapter highlighted various biomolecular detection techniques. On comparing, the different detection techniques, (refer Table 2-1) biosensors are the best solution for a lab-on-chip device. Table 2-2 and 2-3 highlights the advantages of using SAW as a transducer for sensing and micropumping applications. The next chapter of the thesis focus on modelling the SAW device and uses this model for subsequent readout circuit designs.

Chapter 3 SAW Resonator Modelling

The SAW resonator is similar to a crystal resonator where the energy is confined to the surface of the piezoelectric substrate[33]. Contrary to the crystal resonators, which confines the wave into the bulk by the top and the bottom surfaces of a crystal, the reflectors placed on the surface defines the boundary for the SAW resonator. The surface emanation of the waves comes with the advantage of high frequency operation, which was the limit for the usefulness of the crystal resonators. The high frequency operating crystal resonator required thin and comparatively fragile disks, which posed serious implications on their mechanical stability. The ability to define lines for reflectors and transducers bounds the SAW resonator's high frequency operation. The high frequency operation comes with the prime advantage for most sensing application, which is, to obtain high sensitivity. The piezoelectric devices and sensors has their sensitivity proportional directly to the square of resonant frequency and inversely proportional to the surface area [34]. SAW devices possess only a very small area. Hence, uniquely combining both the features for achieving higher sensitivity, the SAW device configured in the resonator configuration forms an ideal choice for biosensing applications.

The basic principle of all resonators (acoustic, electromagnetic etc) is the same. The reflection of an oscillating wave upon itself many times forms a cavity structure. Reflection coefficient characterizes the reflection produced by such structures. Reflection coefficient need to be generally greater than 96% (in terms of wave amplitudes). The coupling of the input into the system comprising of the reflectors and the cavity is due to one or more standard inter-digital transducers (IDT). A single IDT or a pair of IDT forms a one port or a two-port resonator respectively

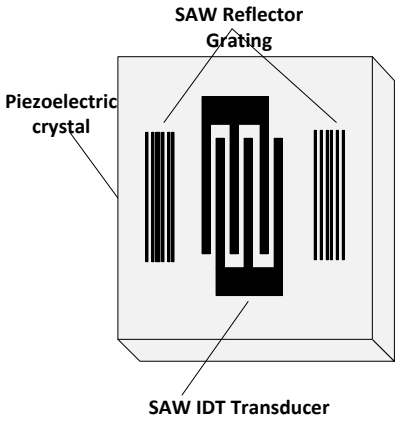

Figure 8: SAW crystal resonator with IDT placed within the cavity formed by reflectors

The SAW crystal one-port resonator shown in Fig 8, makes use of two SAW grating reflector to form a surface wave cavity. The surface waves are complex waves consisting of both transverse and longitudinal motions, which rapidly decay into the bulk of the crystal. Because of this complex mixture, the reflection of the SAW from an abrupt discontinuity is highly improbable. The use of distributed discontinuities circumvents such problems. The coherent addition of many such small reflections gives rise to almost total reflection. The operating characteristics of the cavity depend on the reflection coefficients of each reflector as well as separation between the reflectors. The IDT placed in the center provides the electromechanical coupling into and out of the structure [35]. The IDT placement should ensure that its excitation field pattern couples to the standing wave field pattern of the cavity. A radio frequency (RF) signal voltage applied into the IDT emanates surface waves into both the directions away from the IDT, which is reflected from the grating structures. Resonance defined due to constructive interference of phase is satisfied at frequency $f_c = v/2d$ (corresponding to a wavelength $\lambda_c = 2d$), where d is the inter-grating distance. Such coherent multiple reflection gives rise to standing waves within the cavity. The reflection coefficient is maximum around the center frequency and decreases to zero over a fractional bandwidth of approximately: $2/N$,

where N refers to the number of reflectors. The individual IDT contributes to the acoustic wave potential, the components from individual fingers add together to give a frequency response, which follows the sync function:$\sin X/X$, where $X = \frac{N_p \pi (f - f_0)}{f_0}$, f_0 is the transducers center frequency and N_p is the number of IDT pairs. The reflection coefficients of the distributed reflectors determine the (Quality-factor) Q of the device. Careful design of the reflectors can give Q values as high. The reduction in the energy lost in the cavity to the energy stored in the resonating structure gives rise to high Q values.

The analysis of the surface wave resonators becomes challenging due to the difficulty in characterizing the grating reflectors. The grating can be modelled by some kind of repetitively mismatched equivalent network[36].Different network models with different complexities models the same physical gratings. Transmission lines with repetitive impedance mismatched lengths can represent the grating. The grooved array includes shunt capacitance susceptance between impedance-mismatched lines, which represents reactive energy storage at the grooved edges. The phase and magnitude of the reflection coefficient can be derived from the equivalent networks using conventional network techniques. The equivalent network of an empty cavity can be obtained by connecting two grating structure equivalents (transmission line equivalent) by a length of a line, which represents the cavity region. Coupling can be employed by adding the equivalent network for the transducer into the transmission line which connects the grating reflectors[37]. We can use this equivalent network to analyze the frequency response of the resonator over a wideband. For practical purposes, the region of interest for predicting the resonators performance is mainly near the resonance. Thus, a narrow band approximation makes the full transmission-line equivalent network convenient for analysis into the simple form as shown in Fig 9.

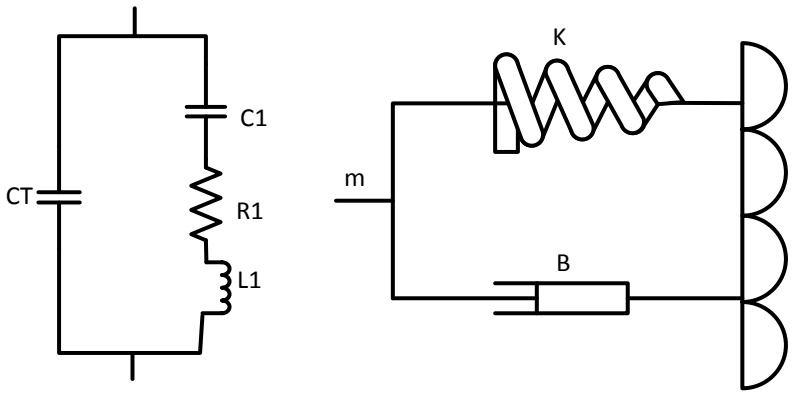

Figure 9: SAW one-port resonator equivalent circuit near resonance, with the equivalent mechanical model.

In the electrical model, C_T represents the static capacitance due to the IDT fingers in the shunt model of the isolated IDT. The resonant resistance R_1 is analogous to the crystal's mechanical resistance (B), the capacitance C_1 represents the crystal stiffness or elasticity, and the inductanceL_1 represents the total mass of the crystal and other external loadings. This parameter responds to mass loading effects. The series L_1, R_1, C_1 portion of the circuit forms the motional arm of the crystal and the capacitance C_T constitutes the static arm.

3.1 Lumped equivalent circuit parameter for one-port resonator.

The section explains the circuit parameter of Fig 9. The capacitance ratio $C_T\ /C_1$ is an important parameter in SAW resonator design, which sets the parallel and series resonant frequencies. Fig 10 shows the distance parameter notation for a one-port resonator [38]. Distance d_c represents the penetration depth into the reflection grating, where the wave has decayed to $1/e$ of its value at entry. Intuitively it acts as a virtual mirror where the SAW wave is reflected completely. The IDT static capacitance C_T is

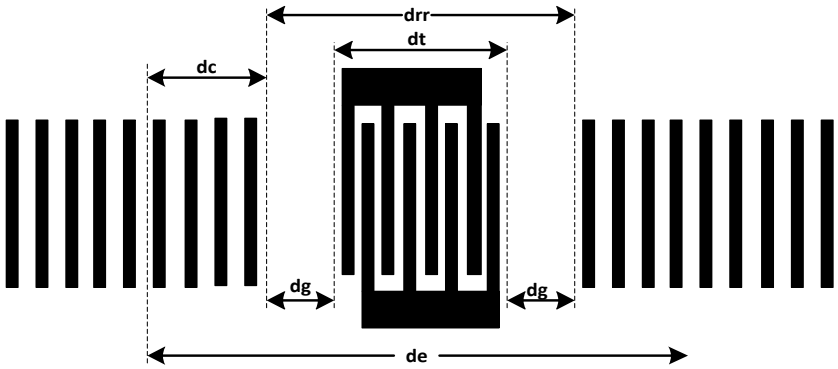

Figure 10: Important distance parameters in the design of one-port SAW resonator

$$C_T = N_P C_S = N_P C_0 W \quad (3\text{–}1)$$

Where N_P = number of IDT finger pairs, C_S = capacitance / finger pair, C_0 = capacitance/finger-pair/unit length and W = acoustic aperture. Lithium Niobate ($LiNbO_3$) has a C_0 value of 5 pF/cm, with the C_0 of quartz equal to 0.55 pF/cm.

Neglecting the IDT finger reflections, the approximate equation for the equivalent series resistance $R_1$is

$$R_1 \approx \frac{1}{G_a\,(f_0)} \frac{(1-\rho)}{(1+\rho)} \text{ Ohms} \quad (3\text{–}2)$$

Where $G_a\,(f_0) = 8K^2 f_0 C_s {N_p}^2$ = unperturbed radiation conductance at IDT center frequencyf_0, K^2 =eelectromechanical coupling constant. It represents the transmission or reception of SAW by an excited IDT. Parameter ρ - the reflection coefficient, is a dimensionless parameter representing the reflected to incident surface wave energy entering the reflection grating.

The equivalent series inductanceL_1, is given by the approximate equation Eq.3-3

$$L_1 \approx \frac{d_e}{\lambda_0} \frac{1}{(4 f_0 G_a\,(f_0))} \text{ Henries} \quad (3\text{–}3)$$

Where d_e = effective cavity length and $\lambda_0 = v/f_0$.

The equivalent series capacitance C_1 is

$$C_1 = \frac{1}{4\pi^2 {f_0}^2 L_1} \text{ Farads} \quad (3\text{–}4)$$

At series resonance, $X_{L_1} = - X_{C_1}$, and the SAW impedance is simplyR_1. The resistor R_1 is the equivalent series resistance (ESR) at series resonance. At series resonance, the resistor R_1 appears in parallel with the capacitorC_T. However, $|X_{C_T}| \gg R_1$, so the SAW essential appears resistive. The series resonance frequency (Fig 11) is

$$\omega_s = 2\pi f_s = \frac{1}{\sqrt{L_1 C_1}} \quad (3\text{–}5)$$

At frequency slightly above the series resonance, the SAW exhibits parallel resonance (Fig.11) or anti-resonance at

$$\omega_a = 2\pi f_a = \frac{1}{\sqrt{L_1 C_T}}, \text{ where } C_T = \frac{C_1 C_T}{C_1 + C_T} \quad (3\text{–}6)$$

$$f_a = f_s \sqrt{1 + \frac{C_1}{C_T}} \quad (3\text{–}7)$$

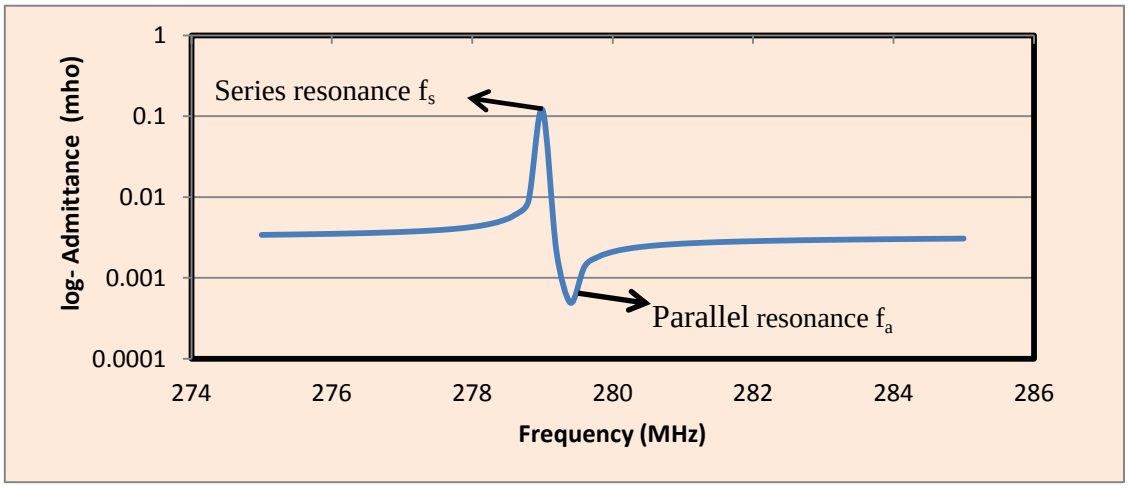

Figure 11: Admittance curve of a one-port resonator

Between f_s and f_a the impedance is inductive with the phase being 90°. This region of operation is the parallel-resonance region and this is the region of interest for a SAW configured as an oscillator. The details of will be explained in the SAW oscillator section.

3.2 SAW resonator parameter extraction

There are many ways of simulating the SAW device behaviour using techniques like Coupling of Modes (COM), Equivalent circuit model (CM), delta function etc. These models are good to provide a qualitative understanding, but fail to model the fundamental physics involved. The equivalent circuit model provides design parameters like the resonant frequency, insertion loss and bandwidth. However, the electrical model derived for the acoustic response follows many assumptions. The finite element method (FEM) is a numerical technique and it gives the most appropriate representation of the SAW device. It works on a very low level of abstraction by modelling the piezoelectric differential equations and the Maxwell's equations for electrical response. This method helps us to have a better understanding of the underlying physics. The solution of the coupled wave equations (Eq.3-8 and Eq.3-9) gives the SAW propagation characteristics: mechanical displacement (U_i) and electrical scalar potential

$$\boldsymbol{\rho \frac{\partial^2 U_i}{\partial t^2} - C_{ijkl} \frac{\partial^2 U_k}{\partial x_j \partial x_l} - e_{kij} \frac{\partial^2 \varphi}{\partial x_k \partial x_j} = 0} \tag{3–8}$$

$$\boldsymbol{e_{ikl} \frac{\partial^2 U_k}{\partial x_i \partial x_l} - e_{ik} \frac{\partial^2 \varphi}{\partial x_i \partial x_k} = 0} \tag{3–9}$$

In the above equation, ρ is the density of the mass, C_{ijkl} the stiffness constant for constant electric field, e_{kij} is the piezoelectric constant, e_{ik} is the permittivity for constant strain. The above equations with the device geometry, material properties (substrate and electrodes) and the boundary conditions solve the problem. The FEM provides the

numerical solution to this problem, by breaking down the model into small regions called as elements connected via specific points called nodes. The solution to the unknowns referred to as degree of freedom (DOF) is calculated at these nodes.

The FEM is a numerical technique, which relies on the use of a computer to solve the large number of unknowns. The solution was carried out by using ANSYS [4] which is one of the most popular finite element software available. It has a well-developed piezoelectric coupled field solver, ability to use either script files or the graphical user interface (GUI) to create model geometry, meshing and solving. The post processing and animation helps in detailed analysis of the obtained results.

3.2.1 SAW one-port resonator

The important parameter that determines the performance of the SAW resonator are the electrode/reflector width, electrode/reflector height, metallization ratio, number of IDT/reflector pairs and acoustic aperture.

Issues in FEM simulation of the SAW structure:

The SAW resonator consists of a length of approximately 500-1000λ (transducers and reflectors together), aperture width of about 50-100λ and substrate thickness of 100λ. For the SAW simulation at least 10-20 elements per wavelength is required to get a reasonably accurate result [39]. This would compute to about 2.5×10^7 elements, each element when solved for the four DOF would give 108 unknowns, and this would require large computational resources to get a solution. Hence, we use the reduced finite element model to model the SAW device.

The following assumptions help to reduce the complexity in the FEM

- Two-dimensional (2D) model: The SAW profile in the lateral direction is similar; hence, there is no much significance to consider this direction in the simulation. Thus, the model reduces to a 2D structure.
- Substrate Depth: The penetration depth is typically about three wavelengths, where the displacement dies to less than 5% of the initial value as shown in Fig 12.
- Periodicity of the structure: "If the standing waves are spatially periodic along a certain axis, we can employ a structure of one or one half wavelength of the standing wave to represent the whole resonator"[40]. This require applying proper boundary conditions i.e. either an infinite periodic boundary condition or an absorbing boundary condition.

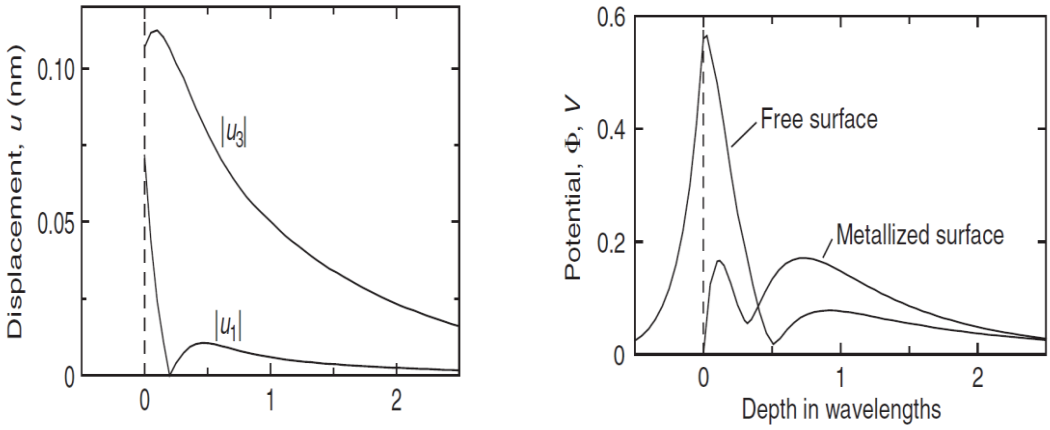

Figure 12 Acoustic displacement and electric potential on Y-Z lithium niobate [41]

Since the above-mentioned three assumptions would involve a symmetric structure, which involves equal distance between the IDT and reflector. To compensate for the second order effects in the device, there can be deviations in the symmetry. For example: to reduce the undesirable finger reflections, a standard technique is to employ split-electrode geometries[42]. Thus, the structure would contain IDT with width of λ/8 and the reflectors

of width λ/4. Considering the design criteria as mentioned in the previous works[43], it becomes importance to simulate the whole structure. Here we have considered the 2D structure assumption and the substrate depth limits. Dampers at the sides of the structure, prevents waves from reflecting from the ends and thus simulating the conditions present in the actual device. The IDT/reflector widths and the reflector-IDT spacing are determined from the transient simulation. Maximum coupling to the standing wave is obtained when the IDT's are positioned optimally i.e. when the electrodes are centred on the standing wave peaks and the distance from the edge of the reflector to the first transducer electrode follows certain conditions[44]. Adjusting the IDT position helps to attain the above-mentioned condition. IDT's optimal placement is obtained by calculating the modified positions using the curve-fitting tool of Matlab. The type of fit used is the "Sum of Sin functions" with the equation- $f(x) = a_1 \sin(b_1 x + c_1)$ as shown in Fig 13.

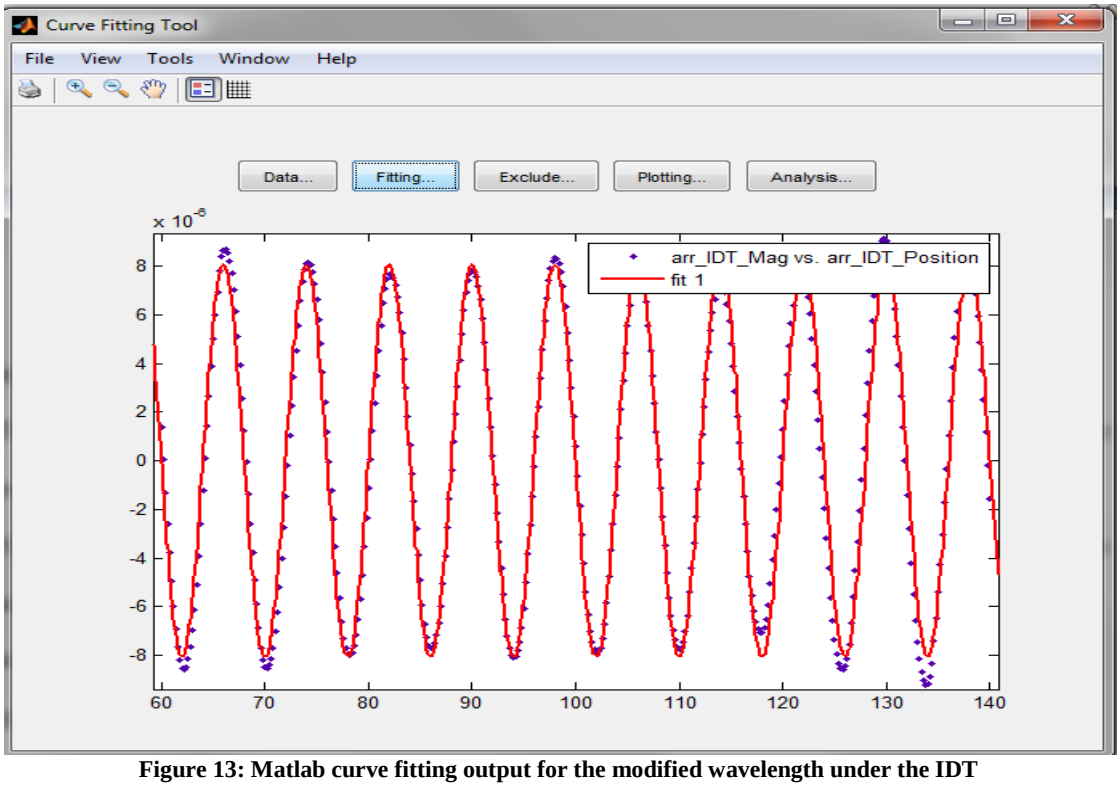

Figure 13: Matlab curve fitting output for the modified wavelength under the IDT

Table 3.1, lists the parameters used for our simulation.

Parameter	Value
IDT Pitch (λ/8 in μm)	1.195
Reflector Pitch (λ/4 in μm)	2.411
Reflector -IDT position (edge-edge $1\frac{\lambda}{8}$ in μm)	10.16
Number of IDT pairs	5.5
Number of reflectors	100

Table 3-1 SAW one port resonator simulation parameter.

3.2.2 SAW circuit parameters

SAW circuit parameters shown in Fig.9 are derived from the admittance values obtained from the ANSYS harmonic analysis.

Static capacitance (C_T) represented by Eq.3.1 is obtained using ANSYS harmonic simulation. A SAW structure with IDT extracts the charge and uses it to calculate the admittance using the following equation [45]

$$Y(\omega) = \frac{j\omega Q}{V} \tag{3–10}$$

The static capacitance is then obtained by substituting in the admittance of the capacitance equation ($Y(\omega) = j\omega C_T$). The obtained parameter is as follows:

Parameter	Value
Number of IDT pairs (N_{idt})	20
IDT Aperture (W)	50λ
Frequency (MHz)	400
Obtained Capacitance (C_t) - pF	8
Capacitance per finger per unit length (pF/cm)	8.04

Table 3-2 Static capacitance obtained from ANSYS harmonic analysis.

The obtained value of 8.04 pF/cm from ANSYS harmonic simulation agrees closely to the previously mentioned results of 5 pF/cm[38].

3.2.3 ANSYS harmonic analysis:

The structure for the harmonic analysis shown in Fig 14 consists of two element types: PLANE 223 and PLANE 183 for modelling the piezoelectric $LiNbO_3$ and Aluminium electrodes. Different material models are chosen for modelling the dampers (at the sides and the bottom surface of the structure). The dampers avoid the boundary reflections. The DAMP property is set for these materials to attenuate the SAW.

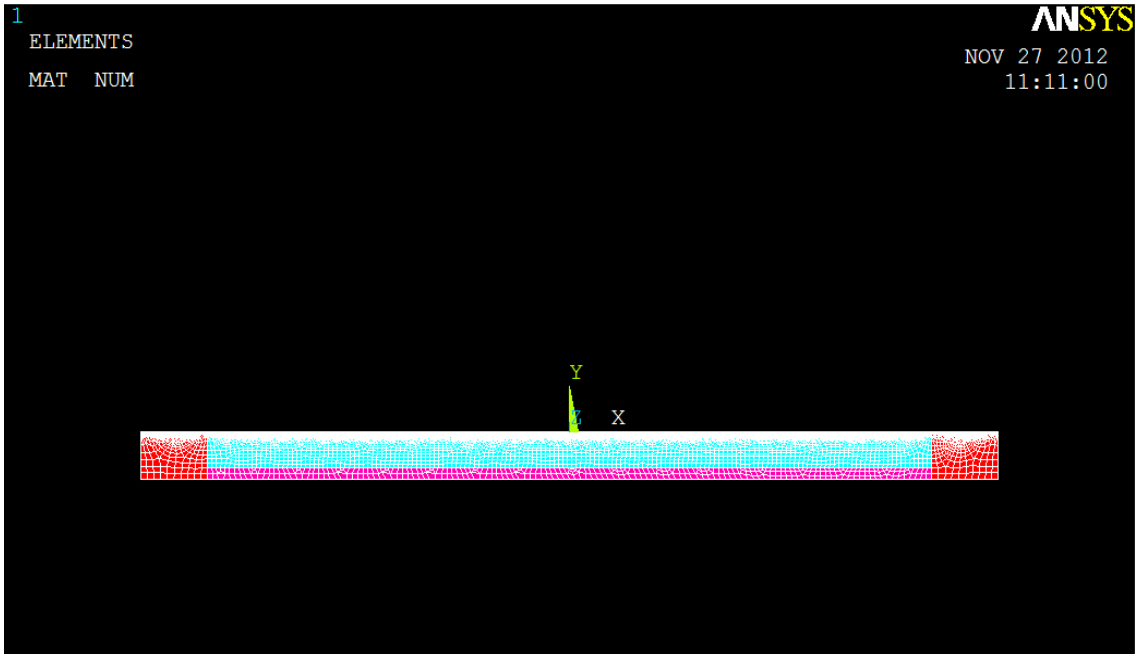

Figure 14**: SAW structure for harmonic simulation**

To reduce computation time and memory constraints, a skilled mesh as shown in Fig 15 is used. The reduced FEM theories mentioned previously is used to select the mesh sizes. The IDT electrodes and the top surface are finely meshed (12 elements per wavelength) and the bottom parts as well as the dampers are loosely meshed (two elements per wavelength). We set the following boundary conditions: 1) top: free space boundary condition is used (no constraints).2) bottom: Here we use clamped condition by setting All DOF (voltage and displacements in X and Y components) to zero. 3) The positive and negative electrodes are set to a voltage of +1V and -1V respectively. The nodes belonging

to the positive and negative electrodes are coupled both for application of the voltages as well as for retrieving the sum of charges which will be accumulated in a single node and thus avoiding the task of summing the charge at each node's manually.

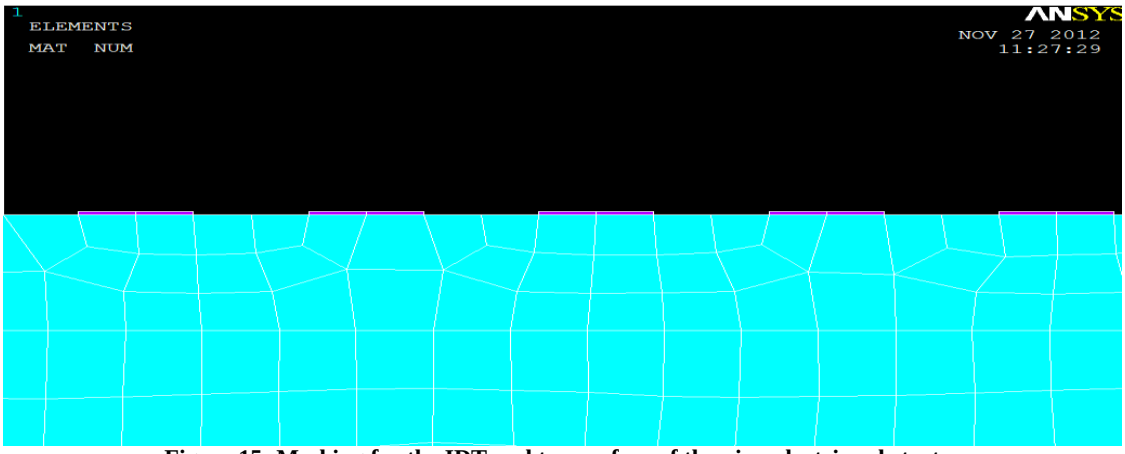

Figure 15: Meshing for the IDT and top surface of the piezoelectric substrate

3.2.4 Simulation results:

The TimeHist Post processor in ANSYS selects the charge (reaction Forces) for both the positive and negative electrodes. Fig 16 shows the simulated response of the one port resonator.

The series (f_s) and parallel (f_a) resonant frequency are 403.6 MHz and 405.6 MHz respectively. These results are used to compute the following circuit parameters.

Equivalent series capacitance (C_1) is obtained by solving Eq.3.4 with the static capacitance obtained from Table 3.2. The series capacitance is equal to 21.9 fFarads.

Equivalent series inductance (L_1) is extracted from Eq. 3.5, to be equal to 7.11 μH.

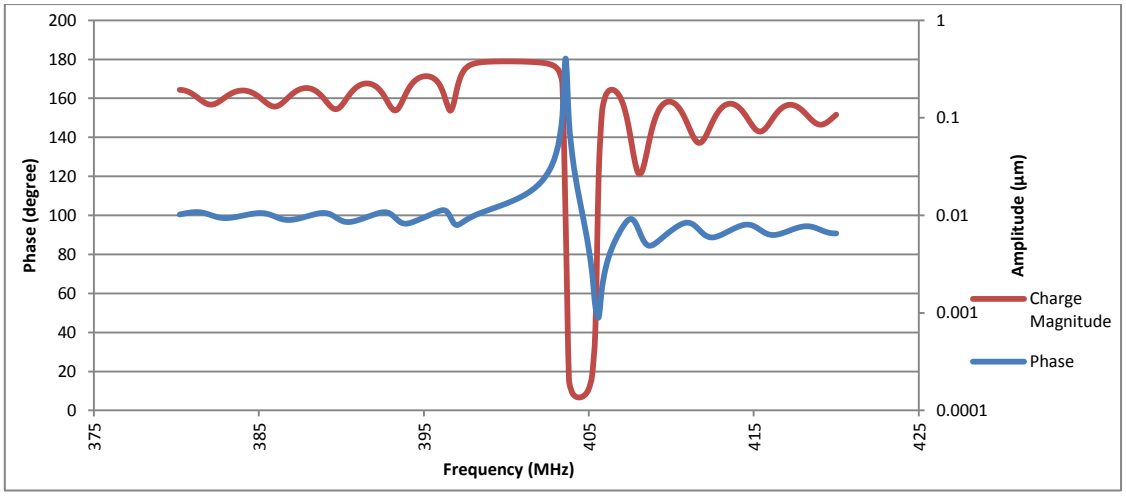

Figure 16: Harmonic response of SAW one-port resonator

Equivalent series resistance (R_1) is obtained by curve fitting the admittance of simulated response to the equivalent circuit model (Fig 9).

The admittance of the SAW circuit model is:

$$Y(\omega) = j\omega C_T + \frac{1}{R_1 + j\omega L_1 - \frac{j}{\omega C_1}} \qquad (3\text{–}11)$$

The curve fitting response for a resistance of 2 ohms shown in Fig 17 follows the simulated response. Hence, the Equivalent series resistance R_1 is approximately 1.5 ohms.

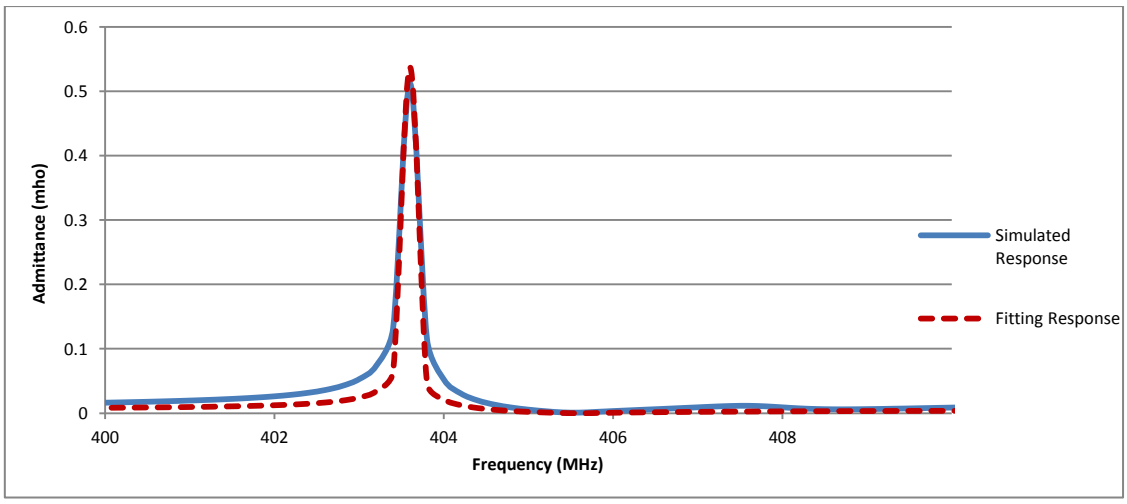

Figure 17: Curve fitting to extract the series resistance

The quality factor (Q) for the structure, which is $\omega_s L_1/R_1$ calculates to a value of 12027. The reported value of Q for LiNbO3 is around 6000. The deviation in the response after simulation is due to the influence of the damping factor. We have not considered the effect of damping due to external influences in the structure. Thus the parameters are recalculated to adhere to the expected quality factor (Q').

The unperturbed radiation conductance (G_a) is:

$$G_a = 8K^2 f_0 C_s {N_p}^2 \quad (3–12)$$

Reflection coefficient ρ is:

$$\rho = \frac{1-G_a R_1}{1+G_a R_1} \quad (3–13)$$

The effective cavity length d_e from Fig 10 can be derived from Eq.3.3. The above-mentioned equation derives a change factor to account for the parameter variations due to change in Q-Factor. Table 3.3 lists the values calculated for the parameters mentioned above.

Parameter	Values
Unperturbed radiation conductance (G_a)	0.207
Reflection coefficient (ρ)	0.526
Reflection coefficient per reflector (r)	0.0059
Change factor (α/r)	0.592

Table 3-3: Parameters for calculating the influence of Q factor change on the circuit parameters.

Based on the change factor obtained above, the modified values of the reflection coefficient (ρ') and effective cavity length (de') are calculated using Eq. 3.14-3.15:

$$\rho' = (1 - \alpha/r)\rho \quad (3–14)$$

$$\boldsymbol{d_e' = d_e/(1 + \alpha/r)} \quad (3–15)$$

Finally, the modified circuit parameters obtained from Eq.3.16-3.18 are

$$R_1' = (1 - \rho')/(1 + \rho')G_a \quad (3–16)$$

$$\boldsymbol{L_1' = d_e'/4\lambda_0 f_0 G_a} \quad (3–17)$$

$$C_1' = 1/4\pi^2 {f_s}^2 L_1' \quad (3–18)$$

Parameter	Value
Modified series resistance $(R_1' \; in \; ohms)$	3.12
Modified series inductance $(L_1' \; in \; \mu H)$	4.47
Modified series capacitance $(C_1' \; in \; fF)$	34.8

Table 3-4: Extracted SAW equivalent circuit parameters

The equivalent circuit model uses the extracted parameters shown in Table 3.4.

The focus of this chapter was to derive an equivalent circuit model for the SAW one port resonator. The model parameters were obtained from the FEM simulation of the one port SAW resonator. Until now, the derivation of the equivalent circuit parameters had many assumptions. Our FEM model on the other hand, considers even the second order effects. Thus, this model could achieve performance quite close to the actual device. The SAW readout circuit simulation uses this model.

Chapter 4 SAW Readout Circuit

The SAW interface circuits for biosensing rely on the principle that any biomolecular event gives rise to a drift in the acoustic velocity, which can give rise to a resonant frequency shift. The SAW configured as a resonator in an oscillation circuit detects the frequency shifts and thus indicates the presence of the target analyte molecule.

A non-ideal SAW device confronts various effects, and compensation gives a precise measurement of the event. The two important issues involve the temperature sensitivity of the sensor and the effects of operation in the non-gravimetric regime.

1) Temperature effects:

Unavoidable variation in temperature creates perturbations in the resonant frequency of the SAW device. However, the AT cut quartz crystal, which forms the substrate for a SAW device has remarkable temperature stability. The AT cut quartz configured to operate in the thickness shear mode, has a zero temperature coefficient of delay, owing to equal and opposite values for the expansion and velocity drifts with temperature. Quartz as a sensor is susceptible to the temperature fluctuations. When a coating is applied either or one or two surfaces of the quartz, the temperature stability drops considerably [46]. This is because of the high temperature sensitivity of the acoustic property of the coating material. The ratio of crystal thickness to the coating can aid in a rough estimation of the temperature sensitivity. The signal dependence on the liquid viscosity and density makes the sensor more vulnerable to temperature instabilities. One way to avoid such temperature effects is by compensation. A reference SAW device encounters an equal output shift as the active device (detects the biomolecular interaction) with temperature changes. The difference of the outputs from the active and the reference device will be free from any temperature variations.

2) Non-gravimetric effects:

An ideal microsensor for biosensing application relies on the microbalance principle, with mass changes alone contributing to sensor response. However, this assumption is not always valid for sensing involving liquid medium. Apart from the mass,non-gravimetric effects like the material properties of the sensor and the binding layer also affects the sensor response[19]. An acoustic load consists of a real and imaginary part. The series resonant frequency shifts is governed by the imaginary part of the acoustic load as defined by Eq. 4-1

$$\frac{\Delta fs}{f0} = -\,\mathrm{Im}\,(Zl) \tag{4–1}$$

Where Zl represents the acoustic load, fo and Δfs denotes the resonant frequency and the frequency deviations respectively. The acoustic energy dissipation in the layers represents the real part, which is proportional to the electrical resistance in the motional arm of the equivalent circuit.

$$\Delta R \infty Re\,(Zl) \tag{4–2}$$

The acoustic load Zl can be represented by the product of a mass factor (M) and an acoustic factor (V).

$$Zl = j\,M \cdot V \tag{4–3}$$

Where $M = \omega\rho h$ where $\omega = 2\pi f$ is the angular frequency, ρ is the density and h is the thickness of the coating

$$V = \frac{tan\,\varphi}{\varphi}$$

φ , is the phase shift encountered by the acoustic wave on travelling through the film.

$V = 1$, is the standard microbalance response due to gravity. In practice, the non-gravimetric effects also influence the sensor response.

For the current thesis work, the non-gravimetric effects on the sensor response are not considered; hence, the SAW behaves as an ideal microbalance, with the temperature compensation provided by the reference SAW sensor. The surface waves passing through the crystal surface causes the particles to follow an elliptical path synchronized to the surface displacement. This movement of a thin layer of the surface imparts kinetic energy increase without any energy dissipation to the wave. Thus, mass loading gives rise to a shift in the acoustic wave velocity defined by Eq.4-4[47] :

$$\frac{\Delta v}{v_0} = -(K_1 + K_2) f_0 h \rho_s) \qquad (4\text{–}4)$$

Where C_m is a mass sensitivity factor, ρ_s and h are the density and thickness respectively of the film and f_0 is the operating frequency. SAW device configured as a resonator measures the change in acoustic wave velocity. The velocity shift v_0 gives rise to a shift in the oscillator frequency from f_0 by Eq. 4-5

$$\frac{\Delta f}{f_0} = \frac{\Delta v}{v_0} \qquad (4\text{–}5)$$

An exact empirical formulae relating the resonant frequency shift to the mass loading is:

$$\Delta f = -(K_1 + K_2) {f_0}^2 \Delta m A^{-1} \qquad (4\text{–}6)$$

Where Δm is the additional mass and A is the sensing surface area.

System specification:

A mass of 100 pg on a $LiNbO_3$ substrate and at a resonant frequency of 405 MHz gives a resonant frequency shift of 1 KHz. Hence, our system detects a maximum frequency deviation of 3 MHz.

4.1 SAW oscillator

The oscillator circuit has SAW as the resonator in the feedback network. SAW biosensor configured in the resonator mode is equivalent to a normal quartz crystal. The SAW used in our projects works at a fundamental frequency of 405 MHz set by the appropriate device parameters derived in chapter 3.

Design specifications	
Supply voltage	1.8 V
Frequency	405 MHz

4.1.1 Operation

The SAW is configured in the pierce oscillator configuration as shown in Fig.18. In the parallel-resonance region, the crystal appears as an $LeRe$ circuit (Fig 19). If the R is neglected the phase shift provided by the tuned circuit is -180°. The crystal operated in the parallel resonance region generates a total phase shift of -360°.

The resonance frequency occurs at a frequency where the net impedance becomes resistive.

$$\omega 0 = \frac{1}{\sqrt{LeC_T}} \quad (4–7)$$

Where $C_T = \frac{C_1 C_2}{C_1 + C_2}$

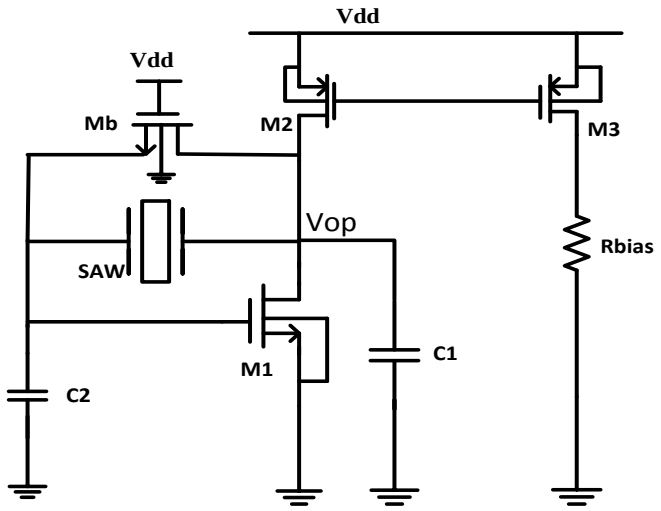

Figure 18: SAW oscillator Schematics

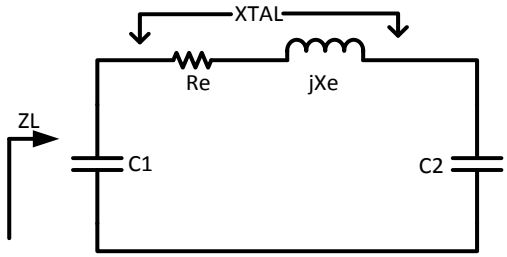

Figure 19: SAW equivalent model at parallel resonance

Following the condition of $|X2\ (\omega_0)|\ \gg\ Re$

We get,

$$Zl\ (j\omega_0)\ \approx\ \frac{[X_2(\omega_0)]^2}{Re} \tag{4–8}$$

The open loop gain at resonance is

$$Av\ (j\omega 0) =\ -g_m \cdot\ \frac{[X_2(\omega_0)]^2}{Re} \tag{4–9}$$

The voltage feedback factor is

$$\beta\ (j\ \omega_0) = \frac{jX1}{Re + j(X1 + Xe)}$$

Substituting the condition of resonance, we get,

$$\beta\ (j\omega_0)\ = -\ \frac{C1}{C2} \qquad (4\text{–}10)$$

Thus, the loop gain condition for oscillation is

$$\beta \frac{g_m}{(\omega_0)^2.Re.C_1.C_2} > 1 \qquad (4\text{–}11)$$

Circuit parameter	Equation	Value
C1	Eq 4-6	0.5pF
C2	Eq 4-6	0.5pF
gm_1	Eq 4-10	855µA/V

4.1.2 Simulation results

4.1.2.1 Transient results

This simulation results (Figs: 20, 21) shows the voltage waveform obtained at the drain of transistor M1 (Fig 18). The oscillation frequency, which was calculated by measuring the time-period for the waveform (Fig 21), was roughly equal to 405.49 MHz.

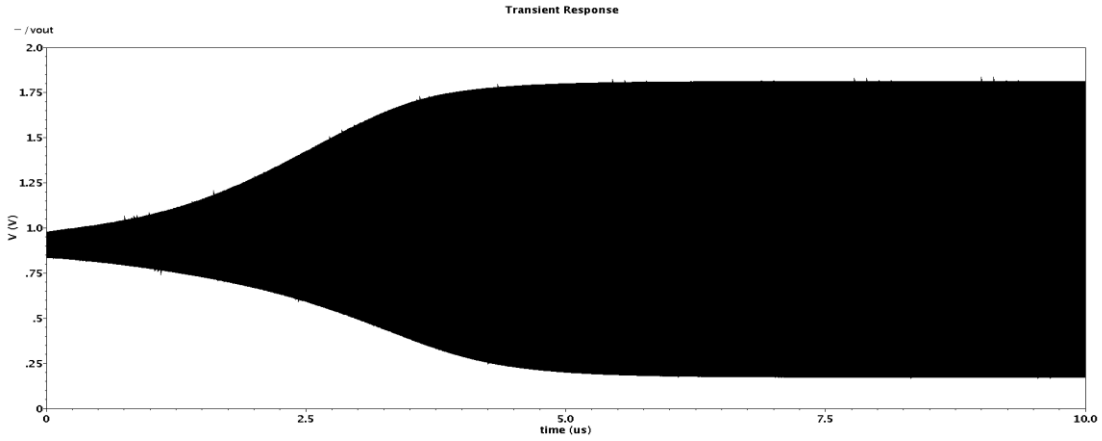

Figure 20: SAW oscillation transient

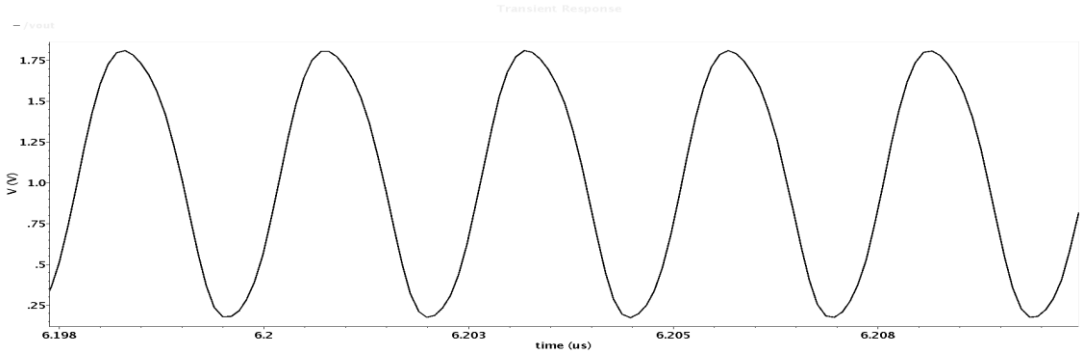

Figure 21: SAW oscillation frequency

4.1.2.2 Discrete Fourier transform (DFT) spectra

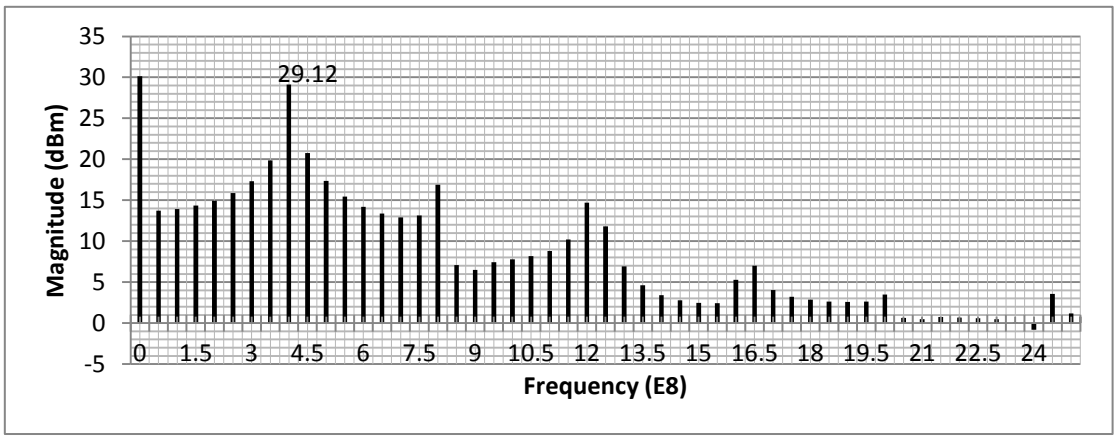

Figure 22: DFT spectra

Fig 22 displays the DFT spectra for the oscillator waveform shown in Fig 20. The plot displays a maximum value at 400 MHz compared to the remaining spectra.

4.1.2.3 Periodic steady state (PSS) and phase noise

The PSS analysis for the oscillator circuit with a beat frequency of 400 MHz and sufficient stabilization time (tstab) of 5µs assumed based on the transient behaviour resulted in an estimate of 405.573 MHz as the fundamental frequency of the oscillator. Fig 23 shows the PSS analysis waveform, i.e. the magnitude of different harmonics of the single ended output measured at the Vop net in the schematic (Fig 23). Fig 24 denotes the phase noise measured at a maximum offset of 100 MHz from the fundamental oscillation

frequency.

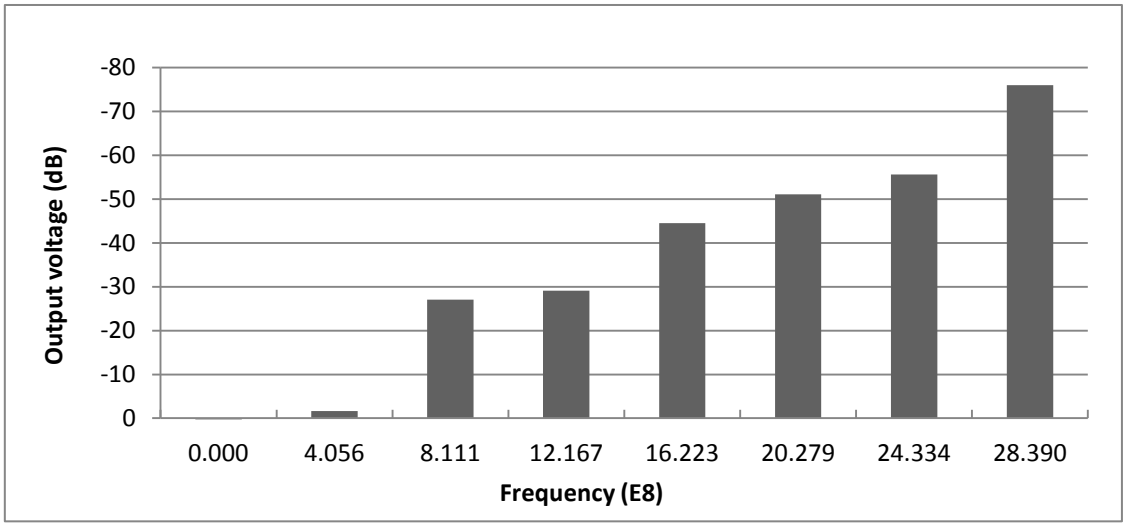

Figure 23: PSS analysis waveform

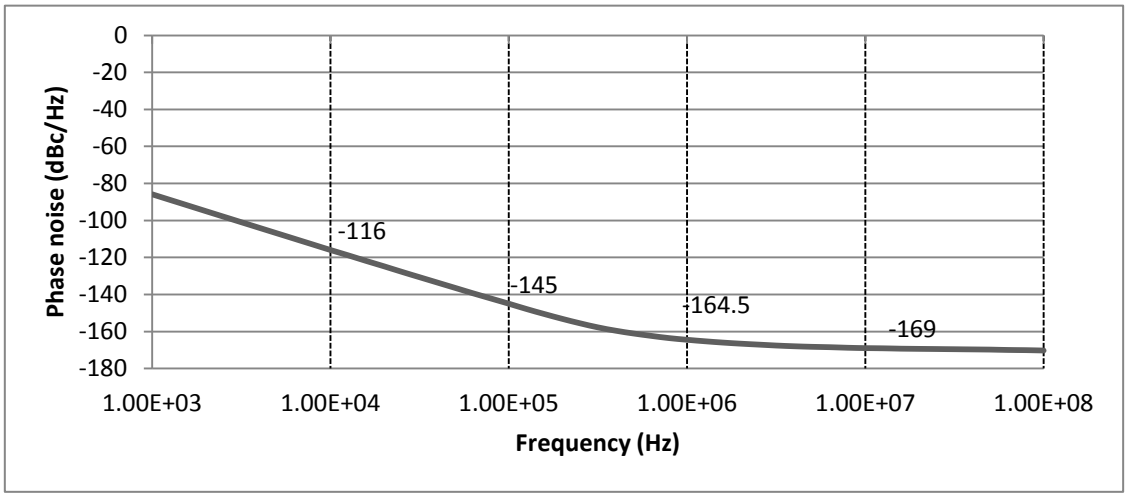

Figure 24: Phase noise

The output oscillation frequency is around 405.5 MHz, which is close to the designed value of 405 MHz, the slight deviation should be due to the tolerances in calculating the R,L and C values of the SAW resonator model from the analytical equations.

4.2 Mixer

Mixers represent one of the most important blocks in radio frequency systems for frequency conversion. In our case of SAW biosensing, the mixer serves two purposes: 1)

To remove the SAW signals variation due to temperature changes. 2) To step down the high frequency signal (405 MHz) to a low frequency, this requires less demanding circuits compared to the high frequency operating circuits.

An ideal mixer as shown in Fig 25, is a multiplier of two signals. It generates the sum and difference of the input frequencies as shown by Eq.4-12

$$Vo(t) = A_1 cos(\omega_1 t) \cdot A_2 cos(\omega_2 t) = \frac{A_1 A_2}{2} [\, cos(\omega_1 - \omega_2)t + cos(\omega_1 + \omega_2)t]$$

(4–12)

Low pass filter selects the difference frequency, which corresponds to the mass loading.

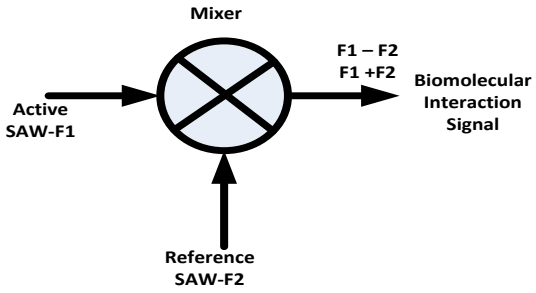

Figure 25: Mixer principle

However, a mixer is a non-linear device, which provides an output that follows the presented identity:

$$y = a\,x - b\,x^3$$

being a the mixer´s gain for the linear response and b the voltage gain for the third order non-linearity. There are passive and active mixers, but due to the higher conversion losses and high noise figures (though a better IM3 response), we go for an active mixer topology. There are two varieties of active mixer- the single and double balanced mixers.

The single balanced mixers, even though are less complex, they suffer from the low RF-IF and LO-IF rejection.

Design specifications	
Supply voltage	1.8V
Conversion gain	2 (V/V)

4.2.1 Operation

The Gilbert cell, shown in Fig 26 implements the mixer. The transistors M1 and M2 converts the Active SAW devices differential voltage signals into a current. To operate within the saturation region as required by the design, small signals should be supplied which ensures that the transistors are not driven out of saturation, else there can be substantial non-linear terms arising in the output response. The reference SAW signal applied to the transistors M3-M6 acts as the switching quad[48].

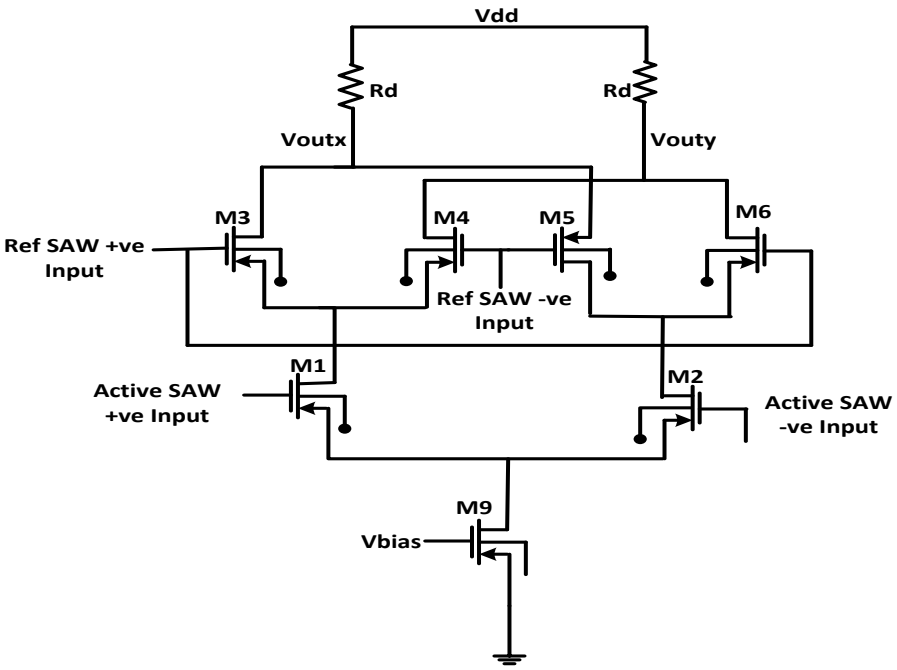

Figure 26: Gilbert mixer

Design equations:

Since the previous stage for the mixer in our system is an oscillator, which gives a differential output, we design for a differential input, single-ended output that feeds a Low pass filter. The switching transistors are set to the same W/L ratio. The ratio of the RMS output (Vout) to the input voltage (Vact-saw: the active SAW input voltage) is the conversion gain of the mixer. As the conversion gain increases, the output signal becomes more sensitive to the input signal. Port-port isolation is another important characteristic to which defines how the mixer ports (input and output) amplitude is isolated from each other. Ideal mixers possess infinite isolation. In the case of mixers used in RF communication system, this parameter is of utmost importance, as the output amplitude is the prime requirement. However, for the SAW biosensing application, the signal information is encoded into the frequency rather than on the amplitude. Hence, the requirement to satisfy a large value of port-port isolation becomes a bit more relaxed.

$$\frac{Vout}{Vin(saw)} = u(v_2) g_{m1} R_{out} \tag{4–13}$$

where v_2 is the reference SAW input signal, v_2 is a sine wave with frequency equal to the resonant frequency: ω_{lo} and $Vin(saw)$ is the active saw input signal, then[48],

$$u(v_2) = \frac{4}{\pi} sin(\omega_{lo} t) + \frac{4}{3\pi} sin(3\omega_{lo} t) + \frac{4}{5\pi} sin(5\omega_{lo} t) + \frac{4}{7\pi} sin(7\omega_{lo} t) \tag{4–14}$$

Thus the output amplitude of the product of the fundamental component of the square wave is:

$$v_o = \frac{4}{\pi} v_{saw} sin(\omega_{saw} t) sin(\omega_{lo} t)$$

$$= \frac{1}{2} * \frac{4}{\pi} v_{saw} sin[(\omega_{saw} + \omega_{lo})t] + \frac{1}{2} * \frac{4}{\pi} v_{saw} sin[(\omega_{saw} - \omega_{lo})t] \tag{4–15}$$

where v_{saw} is the output voltage obtained without switching (i.e. for a differential amplifier). This means that because of frequency translation the amplitude of each mixed frequency component is

$$v_o = \frac{2}{\pi}\, v_{saw} = v_{saw}(dB) - \ 3.9\ dB \tag{4–16}$$

Thus the gain of a CMOS mixer at one of the output frequency component is

$$\frac{v_o}{Vin(saw)} = \frac{2}{\pi} \cdot g_{m1} R_{out} \tag{4–17}$$

The design challenge was to provide an output swing for a conversion gain of two by keeping the transistors in saturation. The biasing voltages was chosen carefully (V_{gs}=0.65V and V_{ds}=0.2V) to allow for significant headroom. Shown below are the designed circuit parameters:

Circuit parameter	Equation	Value
$W/L_{1=}\ W/L_2$	assumption (10µm / 0.2 µm)	50
$I_d = I_9$	Mosfet current equation at saturation (V_{gs}=0.65V and V_{th}=0.45V)	262µA
gm_1	$\sqrt{\mu_n C_{ox}(W/L) I_d}$	2.24 mA/V
R_d	Eq.4-16	1.4 Kohms

4.2.2 Simulation results

4.2.2.1 Transient simulation results

In this response, the inputs to the mixer were the SAW input frequency of 400 MHz and the reference frequency equal to 410 MHz. Fig 27 shows the resultant transient simulation waveform at the output. After filtering the mixer output shown in Fig 27, peak amplitude of 100 mV (difference signal amplitude) was obtained for an input signal of 50 mV, which is equal to a conversion gain of two. Thus, the design gain matched the simulated

response. A parametric sweep for different amplitudes of the reference SAW signal resulted in increase in the mixer output amplitude for increasing amplitude of the reference SAW signal.

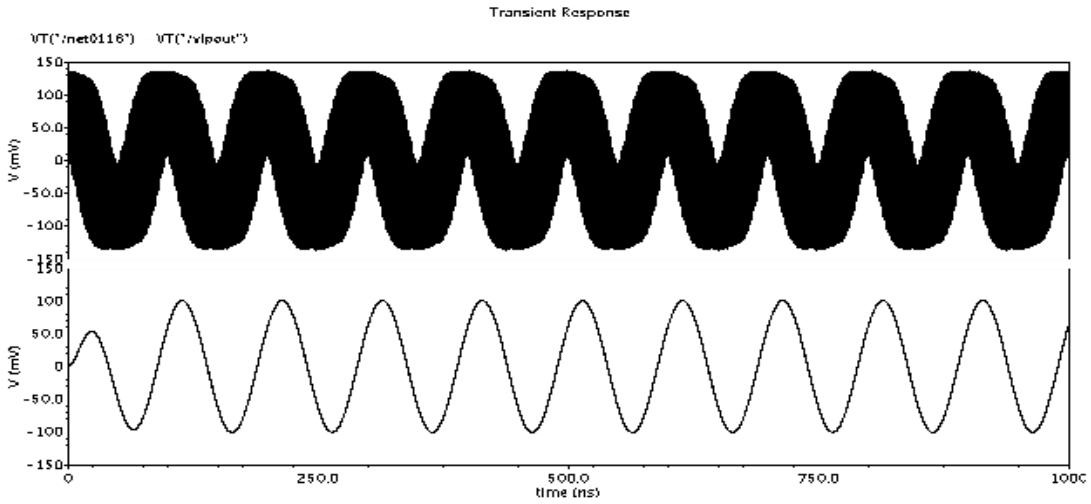

Figure 27: Mixer output signal for input signals of frequency 400 MHz (active) and 410 MHz (reference) and the filtered signal of 10 MHz

4.2.2.2 DFT of the mixer output signal

A DFT using the calculator tool on the mixer output waveform (Fig 28) shows the various spectral components. The low frequency signal of 10 MHz had a relatively higher magnitude compared to other low spectral components. This is sufficient for the SAW biosensing, which relies only on the information encoded into the frequency rather than the amplitude.

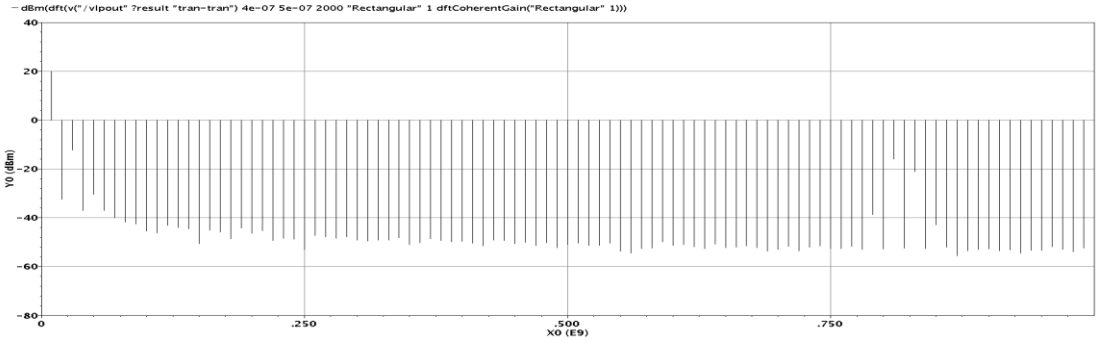

Figure 28: DFT spectra of mixer transient signal (0-1Ghz)

4.2.2.3 Conversion gain of the mixer

The following result shows the response of the mixer to varying reference signal amplitudes across the quad transistors M3-M6 of Fig 26. From Fig 29, we can see that input reference signal amplitude of 1V provides a conversion gain of two. Thus, the specification is met.

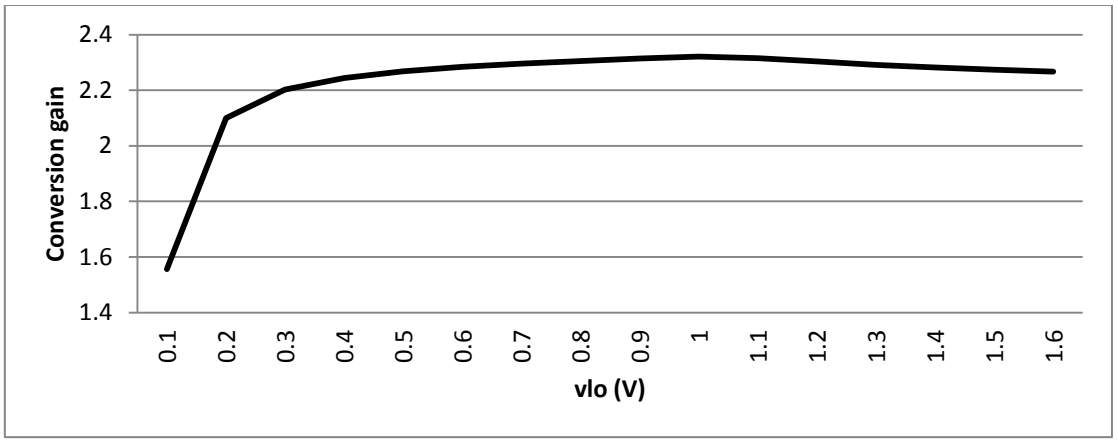

Figure 29: Output voltage with respect to varying reference signal amplitude

4.3 Op-amp for Sallen-Key low pass filter

The Sallen key topology was selected for the low pass filter design. A two-stage miller op amp used in the filter is designed for a cut-off frequency around 3 MHz with a closed loop gain equal to one.

Design specifications	
Supply voltage	1.8V
Gain-Bandwidth	3 MHz
Phase margin	60 degree
Slew rate	10 V/us

4.3.1 Operation

The two stage op-amps as shown in Fig 30, consists of a differential pair in the first stage with a high gain and a common stage which accounts for maximum swings at the output. However, the op-amp has serious instabilities when connected in a feedback configuration. The miller compensation obtained by connecting the capacitor C_c from the output to the input of the second transconductance stage provides sufficient phase margin to avoid instabilities.

The sensitivity of the sensor (1 pg /Hz) decides the cut-off frequency of the filter. The Op-Amp was designed for a $60°$ phase margin. The bias current for the differential pair was set to 22 μA. The second stage transistor M6 and M7 are scaled accordingly to meet the higher gm required for compensation.

Circuit parameter	Equation	Value
C_c	$>0.22C_L$ (for 60^0 phase margin)	2.2pF
I_5	Slew rate * C_c	22µA
$gm_{1,2}$	Gain-bandwidth * C_c	0.04mA/V
gm_6	$>10*gm_1$	0.4mA/V
I_6	gm_6^2 / ($2*U_pC_{ox}*$ W/L_6)	0.064mA

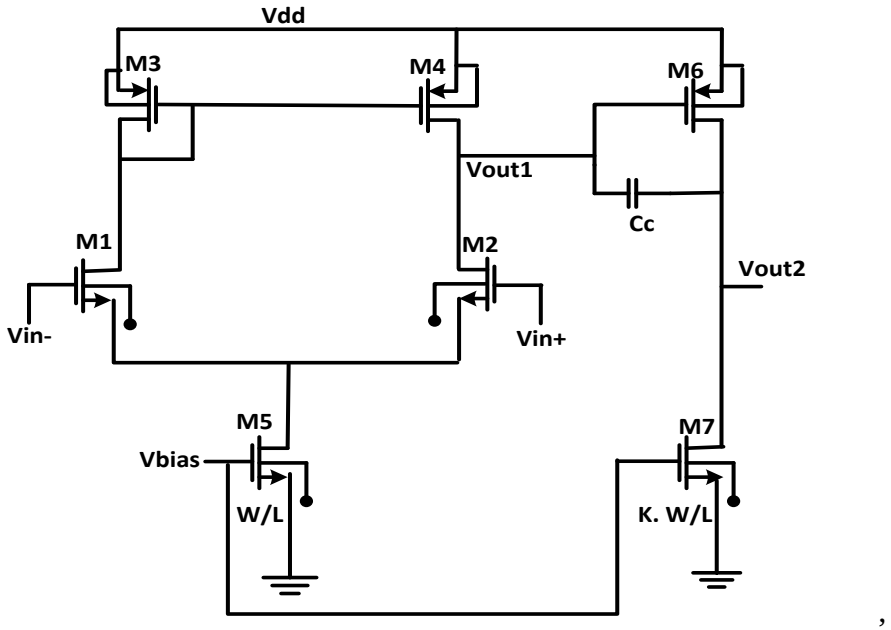

Figure 30: Miller op-Amp schematic

4.3.2 Simulation results

4.3.2.1 Frequency response.

Fig 31, 32 shows the ac magnitude and phase response for the op-amp. The op amp has a gain more than unity for the 3 MHz. The phase margin is equal to 60°. Hence, meets the design specification.

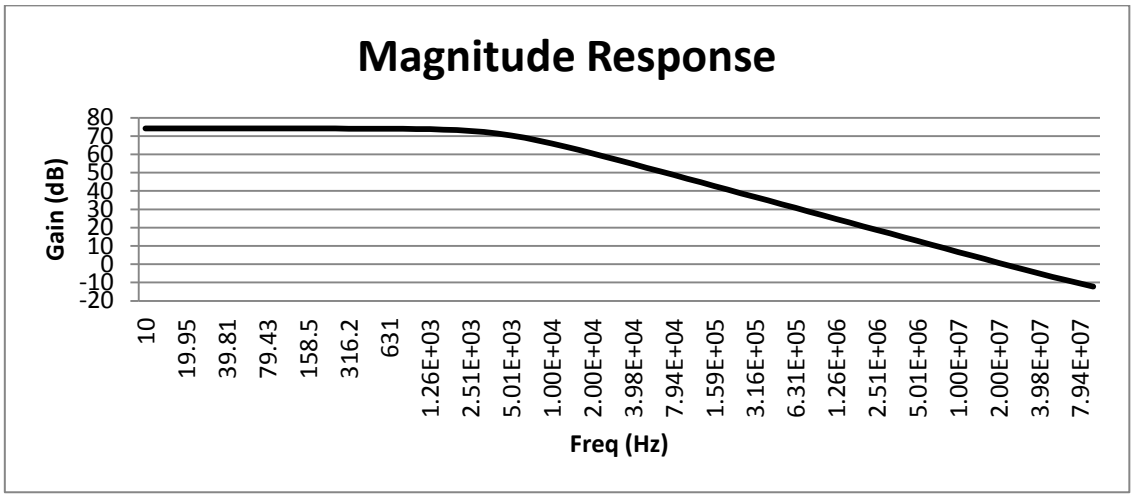

Figure 31**: Magnitude response of the op amp.**

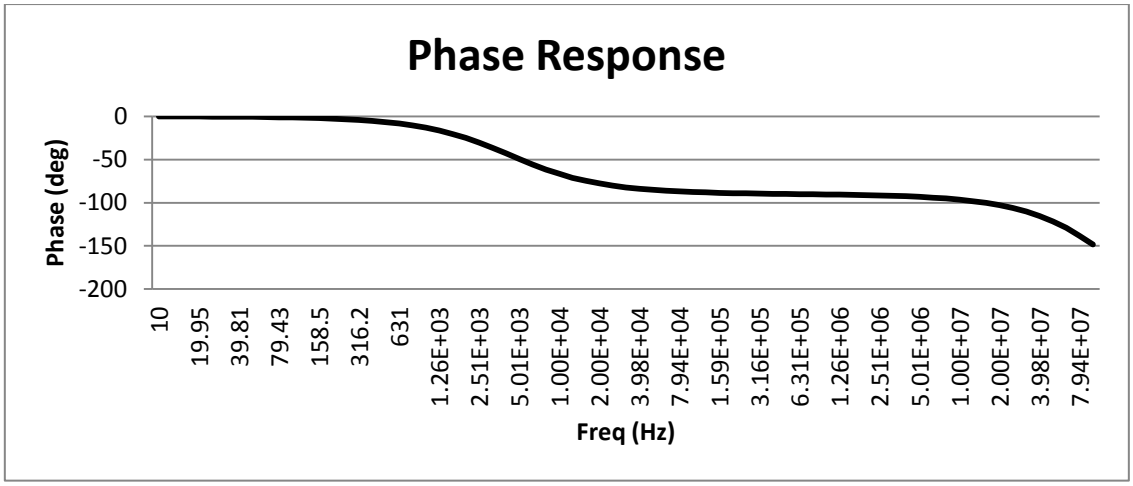

Figure 32: Phase response of the op-amp

4.4 Low pass filter

The Sallen key active Butterworth low pass filter was used. The Butterworth transfer function was selected because the requirement permits for a gradual roll-off rate rather than a sharp transition, and thereby optimizing the passband for maximum flatness[49].

Design specifications	
Supply voltage	1.8V
Filter order	2
Gain	1
Cut-off frequency (corresponds to gain > 0.95)	3 MHz
3 dB frequency	5 MHz

4.4.1 Operation

Fig 33 shows an active low pass filter. At low frequencies, where C_1 and C_f appears as open circuits, the signal is simply buffered to the output. At very high frequencies, C_1 and C_f appears as short circuits, the signal is shunted to ground at the amplifiers input and hence the output amplified value remains zero. Near the cut-off frequency, the impedance of C_1 and C_f are on the same orders of magnitude as R_1 and R_2 and the feedback through C_f provides Q enhancement of the signal [50].

The filter provides a passband gain of unity with a cut-off frequency of 3 MHz. The design was done with a passband tolerance and a maximum stopband gain. Based on the cut-off frequency and the admissible tolerance requirements, the design uses a second order filter. The design equation for calculating the values of resistancesR_1, $R_2$and capacitorsC_1, C_2 in Fig 33 is:

$$f_{-3dB} = \frac{1}{2\pi R_1 R_2 C_1 C_2} \tag{4–18}$$

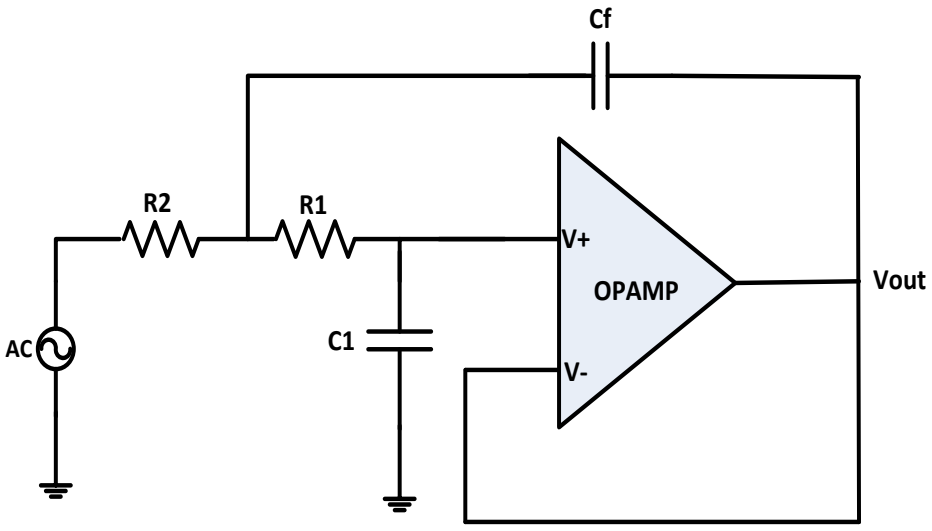

Figure 33: Sallen-Key second order low pass filter

with $R_1 = R_2$ and $C_1 = C_2$, and the value of f_{-3dB}derived from the specifications, the component values are designed.

Circuit parameter	Equation	Value
R_1=R_2	Assumption	10 Kohms
C_1=C_f	1 / (2πf_{3dB}R)	3.04 pF

4.4.2 Simulation results

4.4.2.1 Frequency response

AC analysis of the low pass filter shown in Fig 34,35 has unity gain for the passband with a 3-dB frequency around 5 MHz and a stop-band frequency corresponding to a voltage gain of -20dB (0.1) at 13.2 MHz .

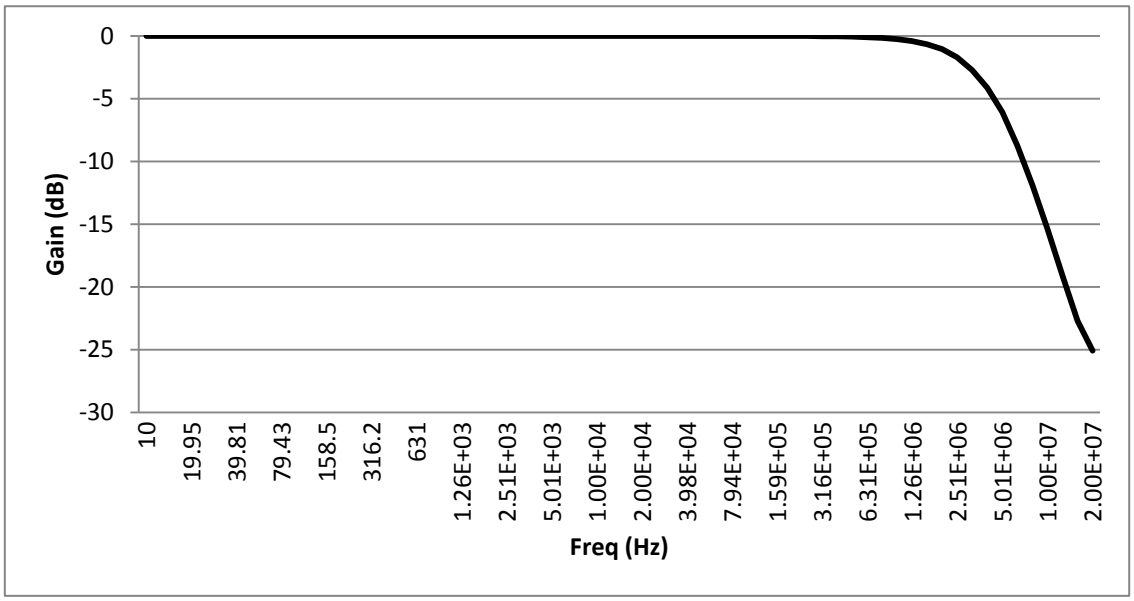

Figure 34: Magnitude response of the low pass filter

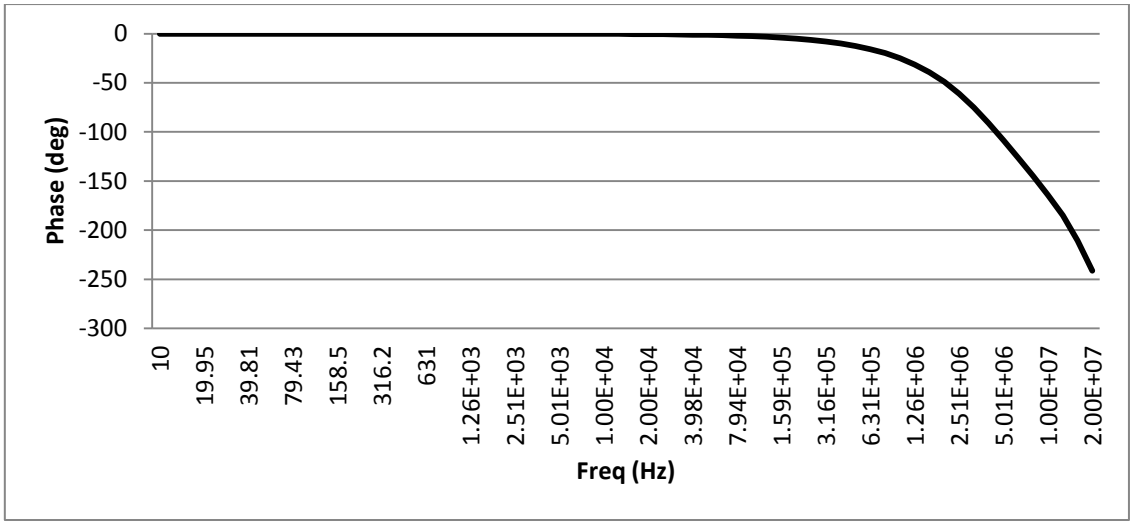

Figure 35: Phase response of the low pass filter

Fig 34, 35 shows that the passband has unity gain. The 3-dB frequency is around 5 MHz and a stop-band frequency at 13.2 MHz.

4.4.2.2 DC transfer characteristics

Fig 36 shows the plot of a large signal input voltage sweep with respect to the output. The characteristics confirm the unity gain response of the low pass filter.

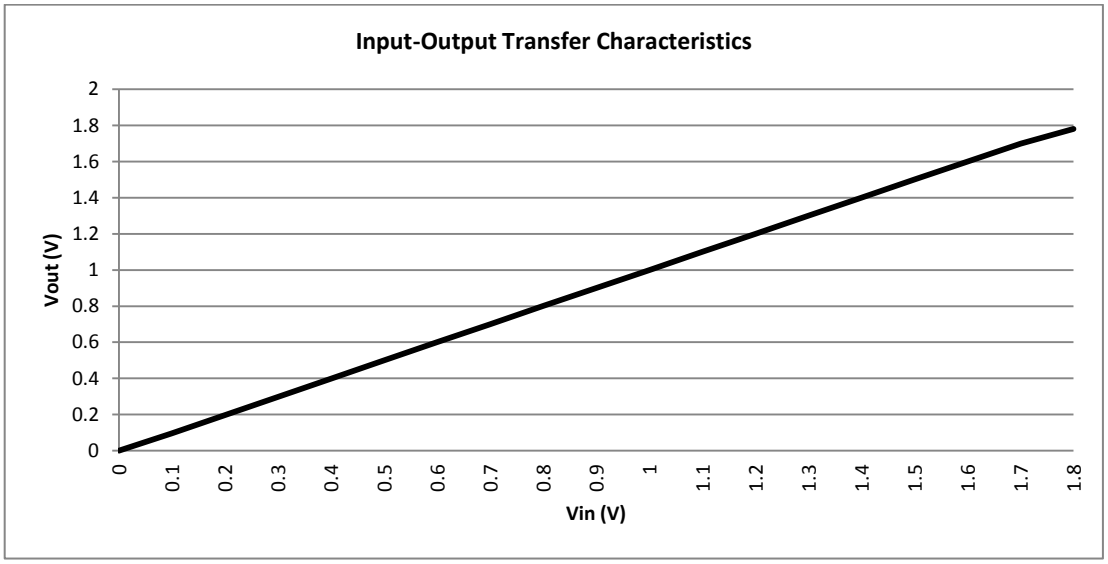

Figure 36: DC transfer characteristics

4.5 Comparator

A comparator converts the sinusoidal signal output from the low pass filter into a square wave for further digital processing (frequency counter).To prevent any spurious noise signal from causing unwanted transitions, an internal hysteresis is built in the comparator. Thus, the comparator can follow the low frequency signals without being affected by the noise around the threshold points. There can also be external hysteresis implemented in the comparator. The hysteresis consists of a positive feedback configuration. The propagation delay was chosen to be less than 1/ (10*maximum input frequency), where the maximum input frequency equals 3 MHz. The trip voltage was set to 1/5 times the amplitude of the signal (150 mV).

Design specifications	
Supply voltage	1.8V
Propagation delay	< 33 ns
Trip Voltage	30 mV

4.5.1 Operation

The positive feedback of the comparator consists of the gate-drain connections of the transistors M4 and M5 in the schematic shown in Fig 37. There is also a negative feedback path in the circuit through the common-source node of transistors M1 and M2, which is a current-series feedback configuration.

If the positive feedback factor is less than the negative feedback factor, then the overall feedback turns to be negative and no hysteresis will occur. Hence, for hysteresis, the

positive feedback factor is sufficiently larger than the negative feedback. This is realized by keeping the ratio β_4/β_3 greater than one [51]. The circuit parameters are:

Circuit parameter	Equation	Value
$A_v(0)$-small signal gain	assumption	1000
Input resolution ($_{Vin\text{-}min}$)	V_{oh} - V_{ol} / $A_v(0)$	1.8 mV
I_{11}	assumption	50 µA
$W/L_{3,6}$	assumption	10
$W/L_{4,5}$	From trip voltage calculation[51]	20

where V_{oh} (1.8V) and V_{ol} (0V) are the maximum and minimum output voltages.

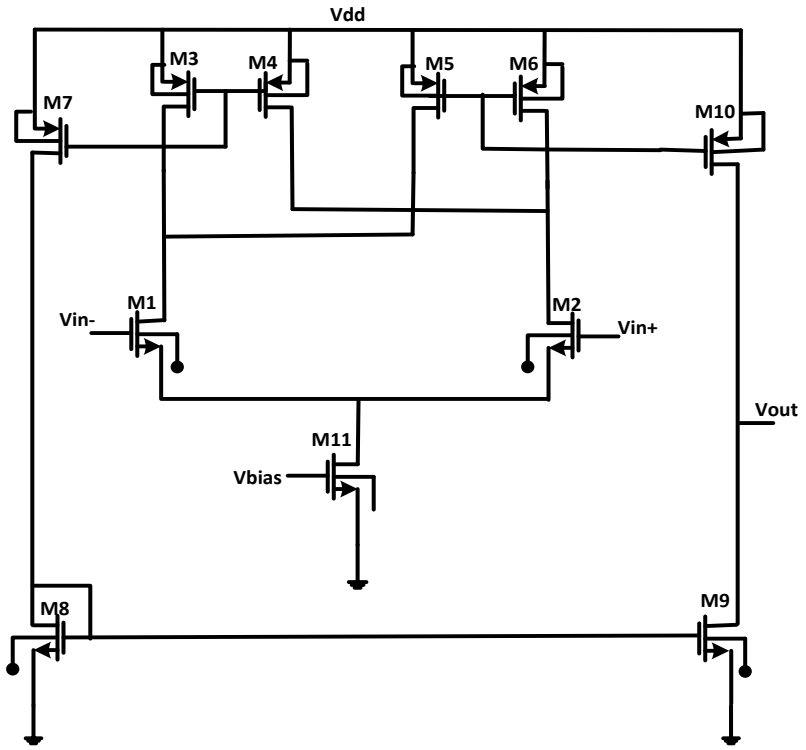

Figure 37: Comparator with internal hysteresis

4.5.2 Simulation results

4.5.2.1 Transient response

The response and the rise time were simulated for an input signal of frequency 3 MHz. The rise time as shown in Fig 38 is about 1.2 ns. The simulation was performed with no output capacitance load.

The propagation delays for different input voltages were simulated and for an input step of 1 mV amplitude (Fig 39) it was equal to a value of 10.4 ns. This ensures that any input voltage of higher amplitude would take less than 10 ns of propagation delay, which fits the design specifications of the comparator. The design specifications demands for the propagation delay to be less than 33ns ($\frac{1}{10*F_{max}}$).

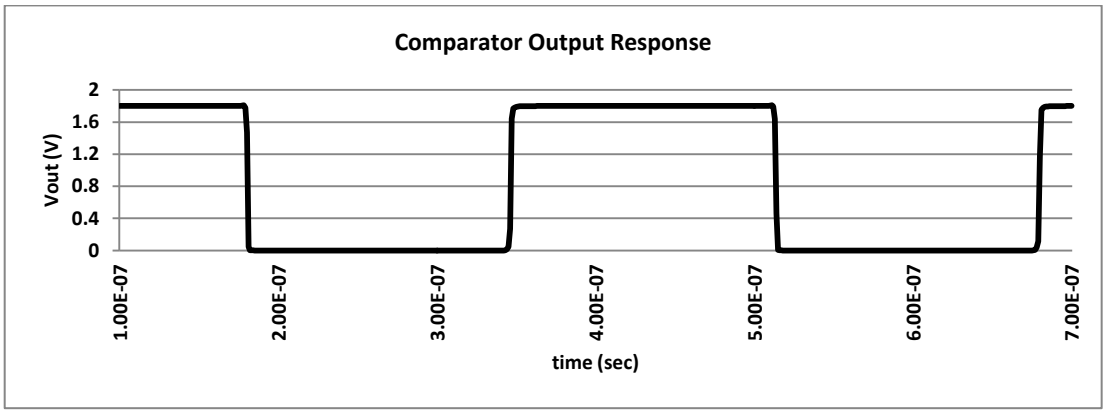

Figure 38: Comparator output for a input sine wave of 3 MHz frequency

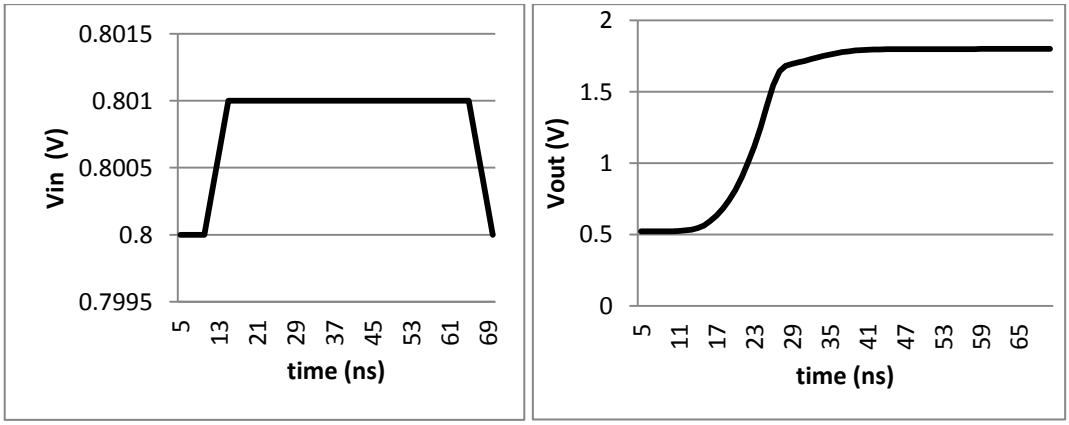

Figure 39: Input and output response for a pulse of 1 mV amplitude.

Fig 40 shows the simulation result for a dc sweep of the input voltage. The input voltage is swept from 0.4 to 1.7 and vice versa with the reference voltage fixed to a voltage of 0.8

V. When the positive input (Vin+) is swept from 0.4 to 1.6 with the negative input (Vin-) held at 0.8, the circuit switches state when the Vin+ is 22.57 mV above Vin- i.e. at a voltage of 0.82277 V. In the case of input being swept from 1.6 to 0.4, switching occurs when Vin+ is at 0.77749 V, or 22.51 mV less than 0.8 V. The theoretical calculation resulted in a trip voltage of magnitude equal to 26.9 mV.

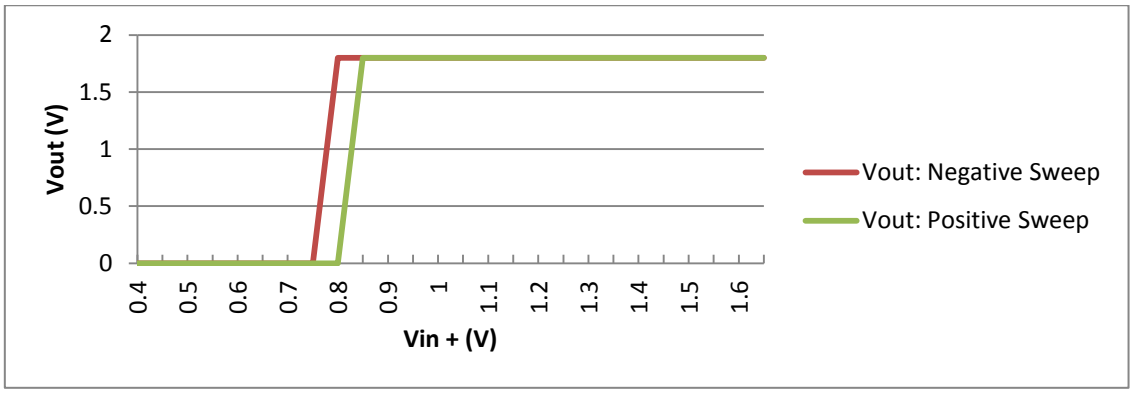

Figure 40: Hysteresis waveform for a dc input sweep.

The comparator circuit precise operation relies on the reference voltage against which the input signal is compared. The dc coupling from previous stages drifts the dc voltage level of the input signal from the reference voltage. Hence, it becomes necessary to generate a reference voltage, which automatically adjusts the reference voltage to the average value of the sinusoidal input signal. This involves a circuit, which extracts the dc component from the input signal. However, the presence of very low frequency components (1 KHz) in the input sets the cut-off frequency of the low pass filter to 500 Hz. However, realization of such a low cut-off frequency requires very high values of resistance and capacitance values, which satisfy the equation$\frac{1}{2\pi RC}$. Hence, due to requirement of large die area for implementing these high valued passive components, the low pass passive filter will be designed with external R and C components. The comparator output is given to an

inverter stage prior to driving the frequency counter, with a 5 pF capacitor load connected to the inverter output.

Thus, a propagation delay of ~10 ns (Fig 39) and a trip voltage of ~22 mV (Fig 40) is obtained, which meets the design specifications.

4.6 Bias generation circuits

The circuits implemented above requires the generation of reference voltages and currents which are stable to supply voltage variations [52]. The bootstrap technique acts as self-bias to generate the output current. A current source feeding a diode-connected load is the basic principle for creating references, which are relatively independent of supply voltage variations. Fig 41 shows the circuit topology.

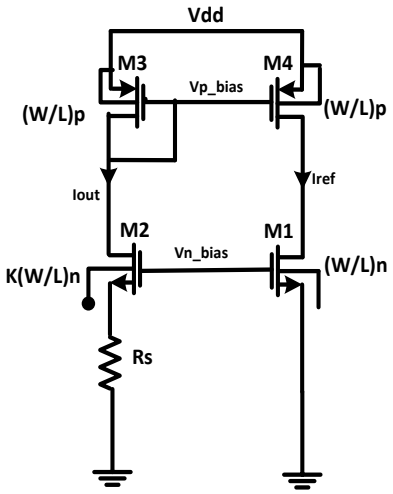

Figure 41: Master bias Circuit to establish supply-independent currents.

The resistor R_s uniquely defines the current with the output current as in Eq 4-18:

$$I_{out} = \frac{2}{\mu_n C_{ox}(W/L)_n} \cdot \frac{1}{{R_s}^2} \cdot (1 - \frac{1}{\sqrt{K}})^2 \qquad (4\text{–}19)$$

The circuit however consists of degenerate bias points. In the above circuit, when the supply turns on and if the transistors carry no current, then this state would continue indefinitely, as the loops can have zero current in the two branches. In other words, the circuit can settle in one of the two different operating conditions. This is referred to as the start up problem; the above issue is resolved by adding a mechanism to drive the circuit out of the degenerate bias point when the supply is turned on, and turning the additional circuitry off during normal operation. Fig 42 shows the start-up circuit. The bias voltages V_p_bias and V_n_bias generated during start up is connected to the Master bias circuit (Fig 41: connected through the same net name), this drives the master bias circuitry to the required initial state[53]. This acts as the master circuit, which provides the bias voltages and currents to the entire readout circuit by connecting the bias voltages V_p_bias and V_n_bias to diode-connected transistors.

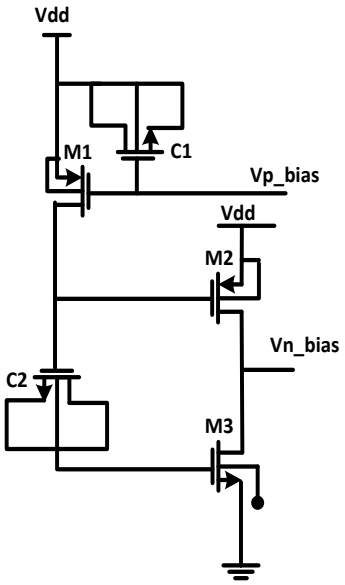

Figure 42: Start up circuit

Fig 43 shows the variation of the bias current with respect to the supply voltage drift. The graph shows an I_{ref} sensitivity of $\frac{\partial I_{ref}}{\partial Vdd} \approx 2.5\ uA/V$.

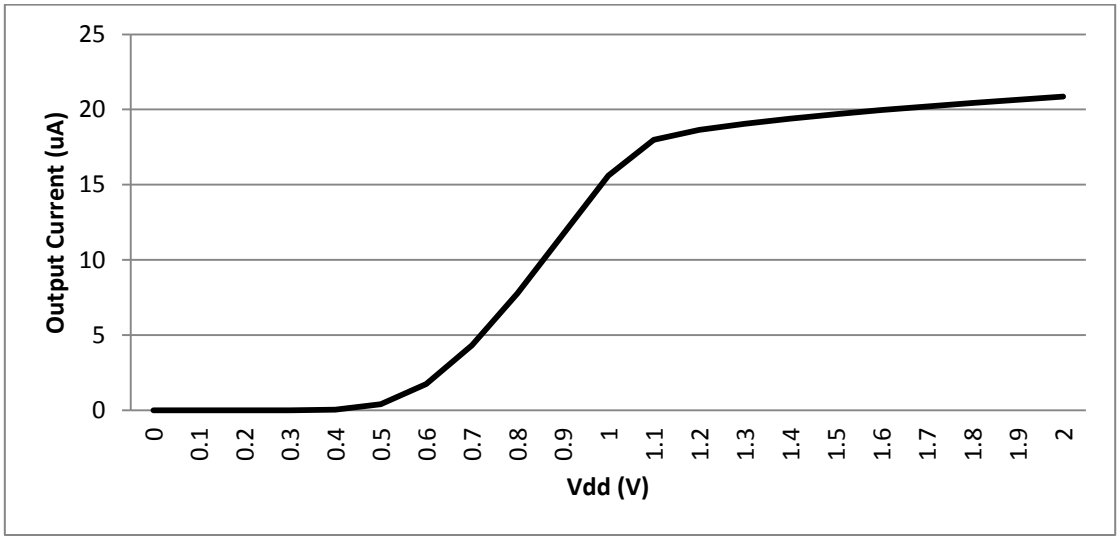

Figure 43: Reference current variation with supply voltage (Vdd) variation

4.7 Integrated system

Fig 44 shows the integration of the individual cells designed above, to represent the whole SAW biosensor system. A differential output (though the amplitudes differ at both the V_+ and V_-) from the SAW oscillator, cancels any spurious noise at the output. The sinusoidal output from the SAW oscillator connects to a passive low pass filter made up of the Resistor R_1 and Capacitor C_1 with the cut-off frequency ($1/2\pi R_1C_1$) set to 5 MHz, which is within the bandwidth of the input signal of 400 MHz. The sinusoidal output from the oscillator, with the dc bias designed using the bias generation circuit feeds the mixer. The out-off band (high frequency) signal from the mixer is filtered using the Sallen-key low pass filter. The output of the filter consists of the required frequency response corresponding to the mass-loading effect. A comparator converts the sinusoidal output from to a square wave. A frequency counter displays a quantized value of the frequency changes accompanying mass loading.

The result in Fig 45 shows the variation of the difference frequency with the change in the inductance value of the SAW resonator model, which is related to the mass loading phenomena (the mass is represented in the electrical domain by the use of the inductance value).

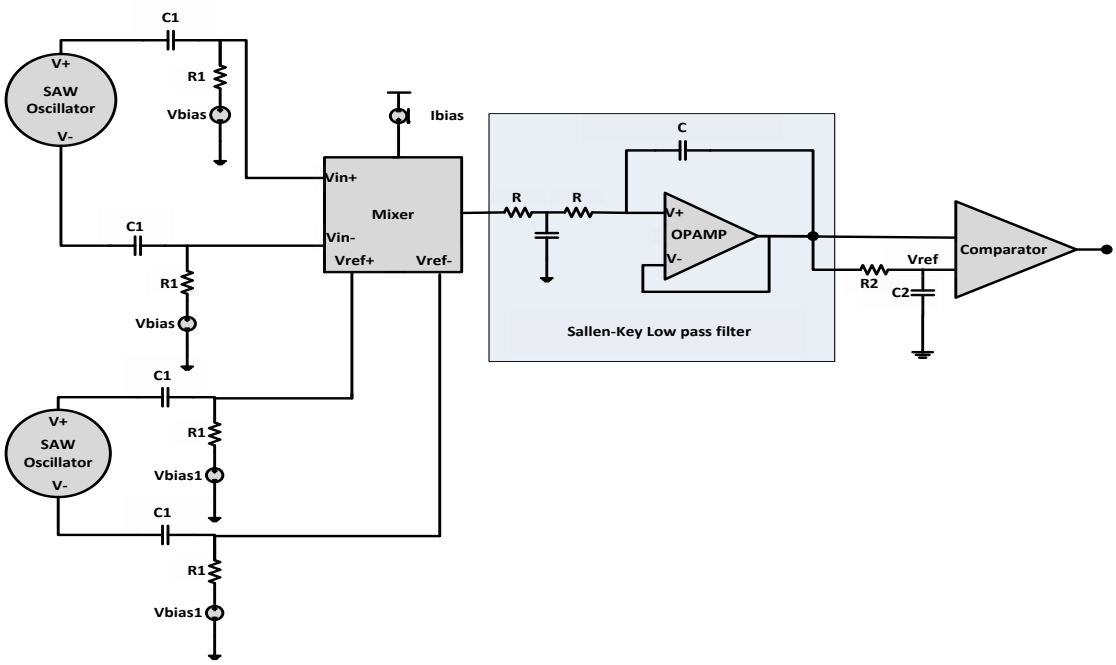

Figure 44: Complete schematic diagram

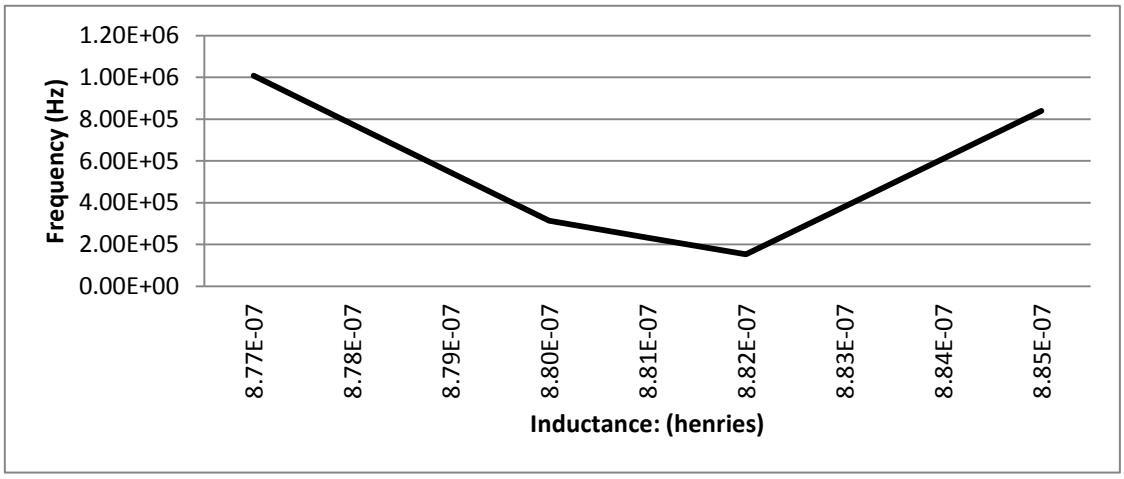

Figure 45: Variation of the output frequency with changes in inductance of the resonator (Reference L value of 881.36 nH)

The readout out circuit topology with an equivalent circuit model for the SAW device at a frequency of 400 MHz. is implemented The frequency drift due to mass changes is simulated by varying the series inductance value of the SAW model. A linear variation in frequency for a mass change (as shown in Eq.4-5) is obtained after simulation. This chapter mainly focussed on designing the circuit architecture for measuring the frequency drift. Rigorous simulations involving different corners are not done, as the aim of the thesis was to come up with circuit architecture with the SAW equivalent model. The readout circuit is implemented in Global Foundries 0.18 μm CMOS technology.

Chapter 5 SAW Micropump

Most biomolecule can endure only within liquids. To detect various biomolecule, it is important to handle small amounts of samples and reagents to affix the target molecules on the surface of the biosensors. When the sample volume decreases to a few microns, it becomes extremely difficult to move the liquid. The acoustic wave generated by a SAW device transfers the momentum and energy into the fluid, creating fluid motion. Section 2.5 compares the various micropump architectures and highlights the advantages of the SAW micropump architecture.

5.1 SAW structures for micropump designs

The SAW interaction with the fluid gives rise to acoustic streaming which is the principle behind the SAW microfluidics [54]. The propagation of the acoustic wave into the fluid and subsequent motions are influenced by many parameters like the applied voltage, acoustic frequency, the fluid density and viscosity and the transducer geometry (the focussed IDT structures generates concentrated streaming effects). By accounting for the viscous effects and density effects with a Rayleigh wave number K_i , the streaming velocity is given by Eq 5-1[55]:

$$U \approx \frac{5}{4}\alpha A^2 \omega K_i \qquad (5\text{–}1)$$

To study the effects of amplitude and frequency of SAW on the acoustic pump, many SAW designs were simulated and fabricated. The various design parameters are frequency, number of IDT pairs, electrode pattern and electrode aperture.

Varying Parameters	Advantages	Disadvantages
Increasing Frequency	Streaming velocity increases	The IDT width decreases and hence process resolution has to increase accordingly

Increasing the Number of IDT pairs	Streaming velocity increases	Insertion loss and device size increases
Electrode Pattern	λ/8 has lesser inter-electrode reflection. Focused IDT for effective streaming	λ/8 requires higher lithographic resolution compared to the λ/4 design.

Table 5-1: Advantages and disadvantages of varying the design parameters

Table 5-1 mentions the advantages and disadvantages of varying the various parameters. ANSYS transient analysis was done for simulating the effects of various parameters mentioned above.

5.1.1 Effect of the number of IDT pairs (N_{IDT}):

Fig 46 shows the effects of varying the number of IDT pairs on the acoustic amplitude. Adjusting the IDT width compensates for the velocity drifts. The result (Fig 46) shows the acoustic wave amplitude increase by 67% for N_{IDT} increase from 10 to 20. Fig 47, shows a linear variation in the acoustic amplitude with the number of IDT pairs which is also predicted by the analytical result Eq. 3.18

$$\varphi(z) = \mu_s \sum_{n=0}^{N_{IDT}} V_n e^{jk(Z-Z_n)} \qquad (5\text{–}2)$$

Where Z_n is the location of the n^{th} finger excited and the finger being excited with the voltage V_n; N_{IDT} gives the number of fingers in the IDT.

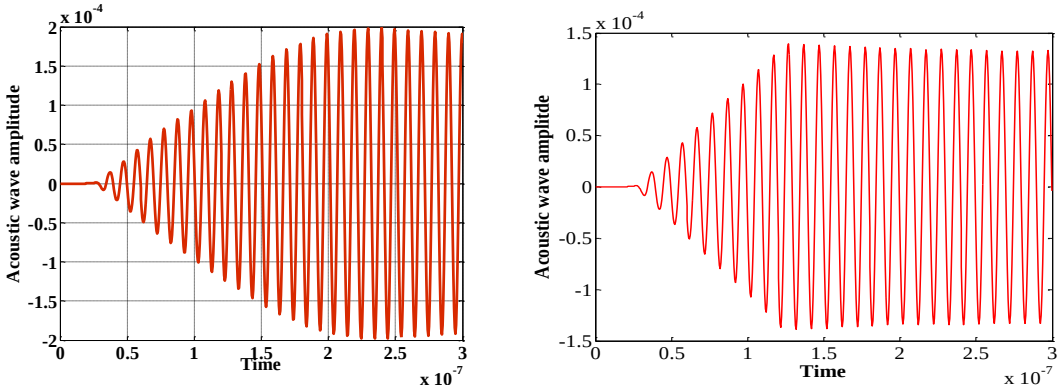

Figure 46: Acoustic amplitude with different number of IDT fingers. Left figure- N=10 and right for N=20.

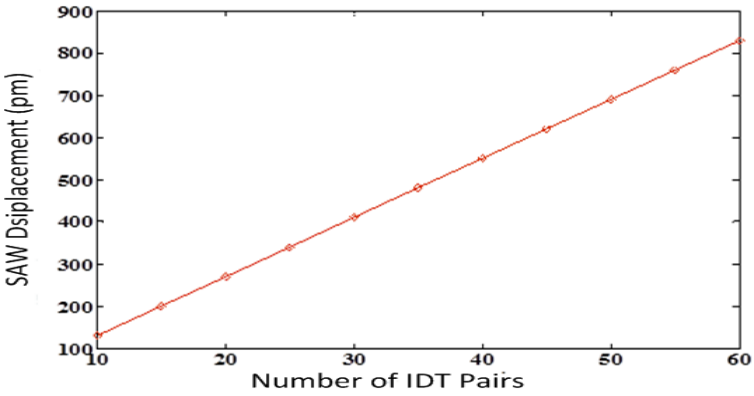

Figure 47: Linear increase in the acoustic amplitude with number of IDT

5.1.2 Effect of the frequency:

Fig 48 shows a decrease in the acoustic amplitude with increasing frequency. The simulated response was obtained for N_{IDT} equals 10. Varying the IDT width modifies the resonance frequency. As seen from the result, the acoustic wave amplitude decreases for the higher frequency device even though marginally by about 8%. The simulated response agrees with previous experimental results [56].

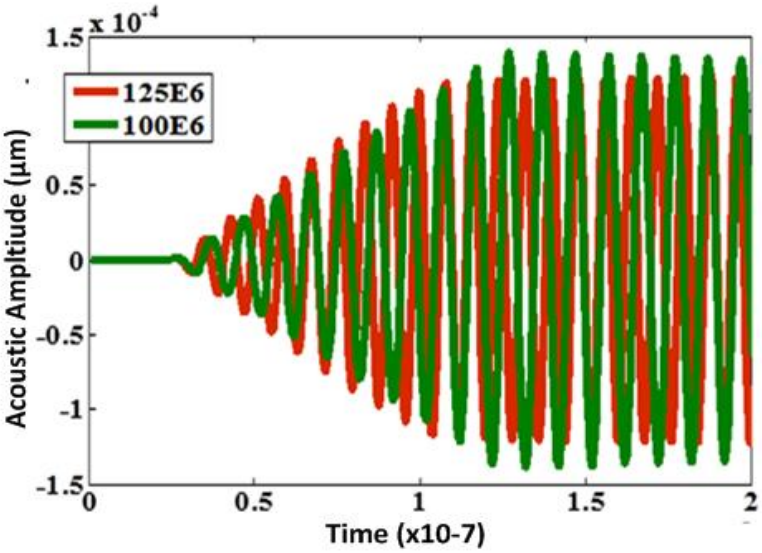

Figure 48: Effect of frequency on acoustic wave amplitude

5.1.3 Effect of device geometry:

The single electrode design has higher finger reflection compared to the split-electrode geometry. For electrode widths and spacing of λ/8 at center frequency, differential path lengths are such that the SAW reflections from each split-electrode pair cancel out at the center frequency rather than add as in the case of a single-electrode IDT [42]. The transient simulation Fig 49 also confirms the effect. A Focussed IDT structure as mentioned in a previous work [55] was simulated in ANSYS and is shown in Fig 50. 3D SAW structure simulation was used. Due to the computational complexity (number of elements) involved, a simpler structure with N_{IDT} of three, frequency of 100 MHz and the radius of curvature of the IDT with a focal length of 45 μm were simulated

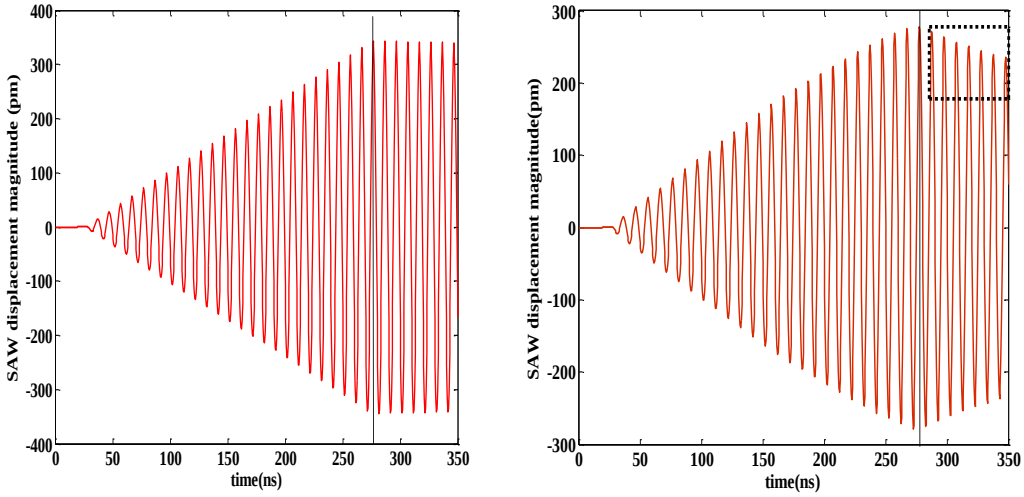

Figure 49: Difference in the single electrode and split-electrode designs on acoustic amplitude; a) shows the split-electrode design with no reflections and b) shows the effect of finger reflections in the acoustic amplitude

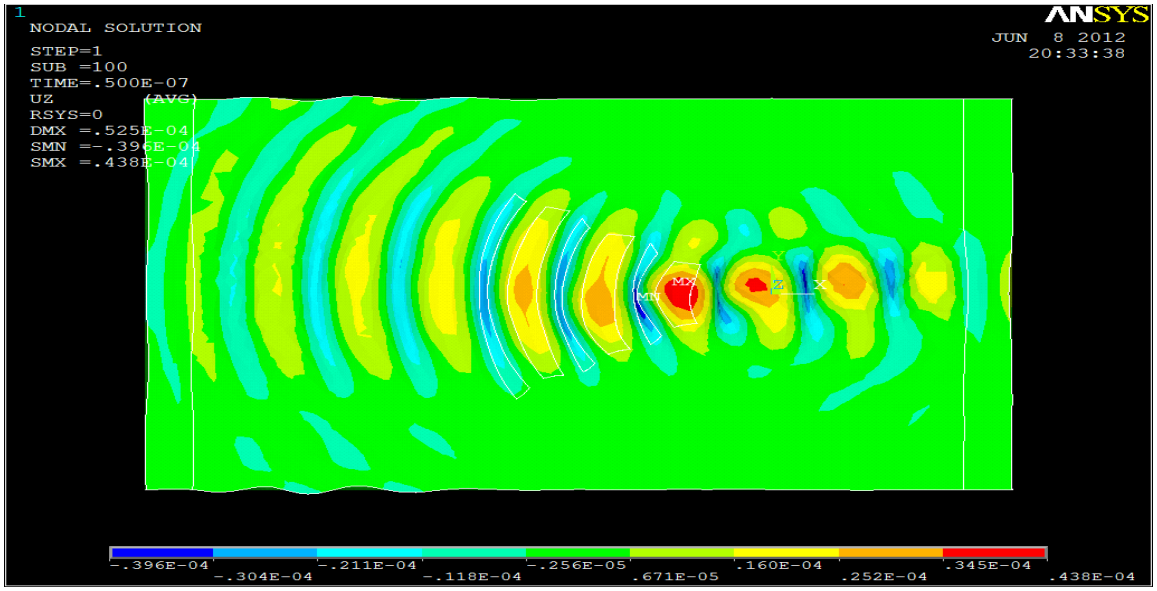

Figure 50: Focussed IDT-with the amplitude variation along the length of the device and the maximum amplitude concentrated at a point.

5.2 SAW micropump design

5.2.1 Polydimethylsiloxane (PDMS) as microchannel

PDMS is widely used for many biomedical applications from catheters to soft contact lens. The ease of manufacturing and lower cost has moved the microfluidic devices from using silicon/Glass substrates to PDMS. The microchannel in the microfluidic devices is fabricated using PDMS. A two part heat curable PDMS material- PDMS Sylgard® 184 (Dow Corning Corporation) is normally used for research purpose. The polymer is first mixed with a curing agent. It is then poured into a mold and thoroughly degassed. The mold with PDMS is heated for several hours. The demolded PDMS is sealed with the substrate. The sealing can be either reversible or irreversible (plasma oxidation) [57]. A reversible contact formed via van der Waals contact is watertight but cannot withstand pressures greater than 5 psi [58].

SAW particle manipulations in channel require the acoustical energy transfer to the fluid through the channel structure. The channel material can affect the coupling of energy into

the fluid. Hence the importance of acoustic attenuation by PDMS needs to be analyzed [59]

5.2.2 PDMS acoustic attenuation characteristics

We use ANSYS modelling of PDMS on a SAW structure to study the attenuation of the acoustic wave due to PDMS. This involves obtaining the material properties of the PDMS material for ANSYS model. PDMS is a visco-elastic material, and hence it behaves like a non-linear material. The Youngs modulus (stiffness) varies with frequency and temperature. A glass transition point (T_g and f_g) is defined to denote the change in material behaviour as shown in Fig 51. The loading frequency f_g is in the KHz region as seen in Fig 51. As the SAW device is operating at around 100 MHz, the Youngs modulus will be in the GPa range, which shows that PDMS attenuates the acoustic wave. The PDMS being viscoelastic has two regimes of operation 1)Glassy regime ($\omega\tau << 1$) and 2)Rubbery regime ($\omega\tau >> 1$) [60].

An equivalent Maxwell model represents the viscoelastic property by a spring and damper. For the SAW pump experiment, the condition (frequency) makes the PDMS to behave as a rubbery material.

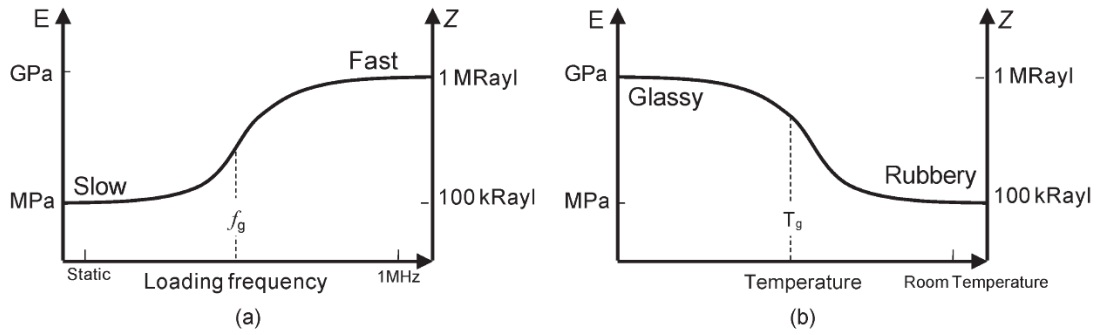

Figure 51: Youngs modulus and acoustic impedance as a function of frequency and temperature for PDMS [61]

The non-linear behaviour of such viscoelastic materials are modelled in ANSYS using prony series, which requires the shear relative modulus (G) and volumetric relative modulus (K) and their respective relaxation times (τ). As the non-linear simulation in ANSYS is time consuming, we approximated the PDMS to behave as an elastic material based on the region of our operation. The value of Youngs modulus, which we derived out of the operating frequency of 100 MHz, is 550 MPa.

5.2.3 Effect of PDMS on SAW- simulation

ANSYS prony series analysis was carried to compare the validity of our approximation. It closely fits to our approximate model. The calculated value of the shear relative modulus was 0.989 with relaxation time of 10^{-4} for the prony series. The transient simulation results in ANSYS closely agreed with each other. Table 5-2, shows the ANSYS linear model parameter for an elastic material assumption.

Parameter	Value
Youngs modulus (MPa)	550
Poisons ratio	0.4
Density (kg/ m^3)	965

Table 5-2: Material parameter for PDMS.

The ANSYS structure for simulating the effect of PDMS on acoustic wave as shown in Fig 52 consists of an input IDT on the substrate ($LiNbO_3$)

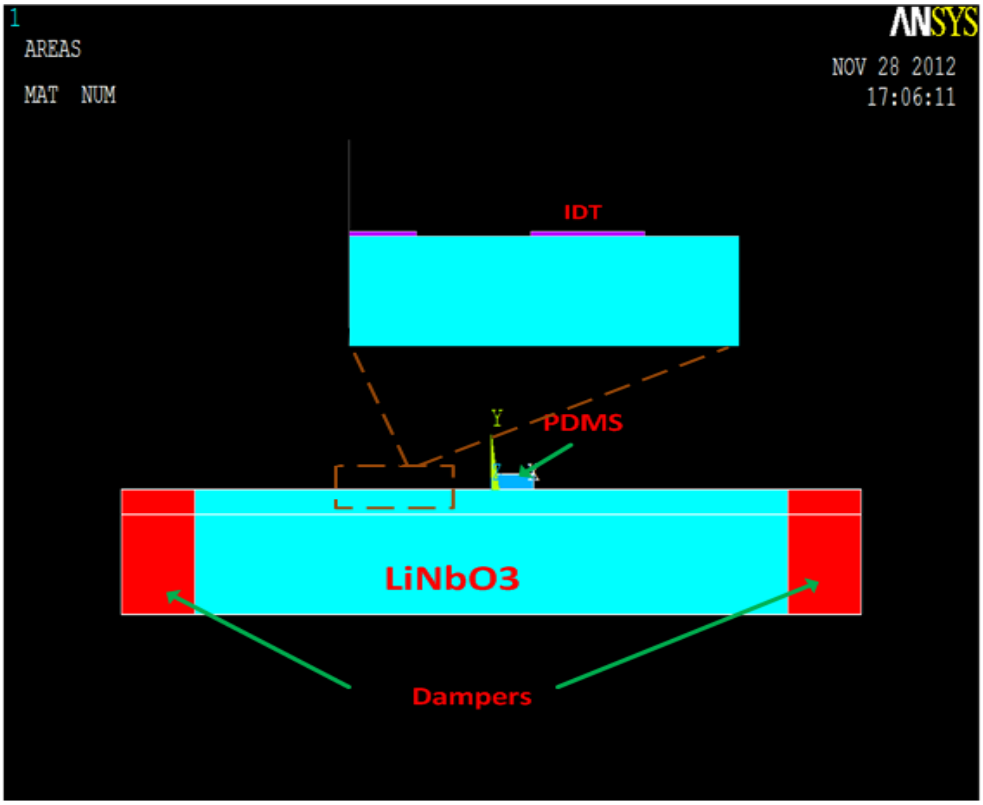

Figure 52: Structure for simulating effect of PDMS on acoustic wave

5.2.3.1 Effect of PDMS length on the acoustic wave:

As intuitively expected, the acoustic attenuation increased with distance. However, as seen from Fig 53, the acoustic attenuation shows a drop with increase in height from 50 µm to 100 µm. The reason is not very clear. A possible explanation can be made by studying the dynamics and response of polymer coating acoustic devices. The PDMS can be considered as an acoustic thick film, and the shear displacement varies across the thick film for various values of a parameter

$$\emptyset_3 \cong \omega h \left(\rho / G'\right)^{1/2} \qquad (5\text{–}3)$$

Where h is the film thickness.

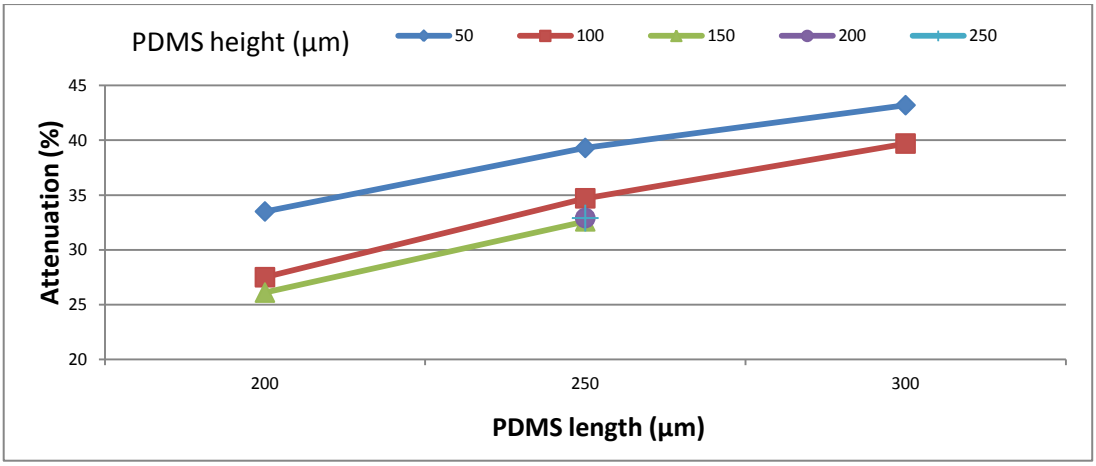

Figure 53: Effect of PDMS length on acoustic wave

As $\emptyset_3$ passes $\pi/2$, film motion at the upper surface goes from an in-phase to an out-of phase condition. Thus the particles in the upper regions of the film has smaller displacements, reducing the kinetic contribution to velocity response [62]. Thus, film mass loading is diminished as $\emptyset_3$ exceeds $\pi/2$. Also other works on fluids has also reported the acoustic attenuation increases to a maximum and then finally saturates [60]. Detailed examination of this effect can only be obtained after performing experiments with various lengths of the material.

5.2.3.2 Effect of acoustic attenuation with frequency:

As shown in Fig 51, the Youngs modulus increases with frequency. The acoustic attenuation increases with frequency as shown in Fig 54. At higher frequencies the film (PDMS) starts behaving as acoustically thick, hence cross-film gradients (normal to the film surface) arises, there happens to be a phase lag in the film bulk causing maximum coupling of acoustic energy from SAW to the film, thus causing increased attenuation [62].

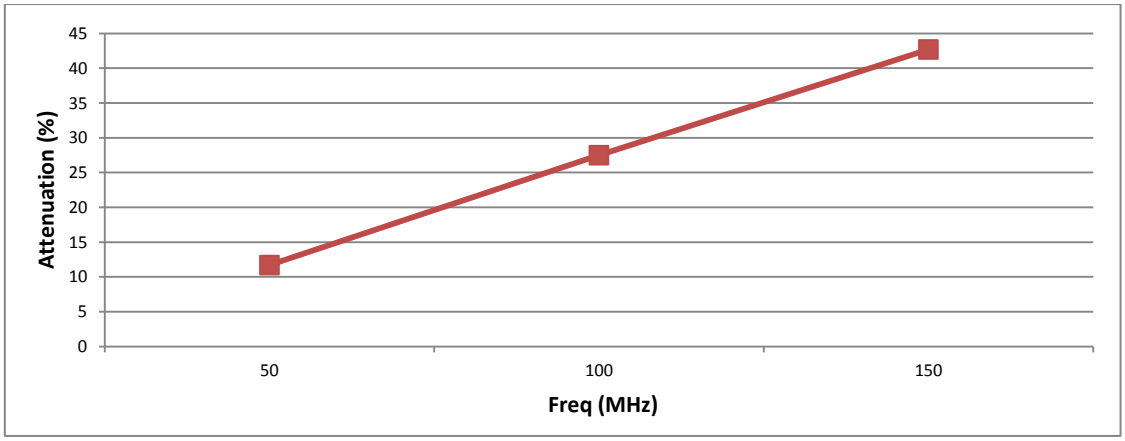

Figure 54: Acoustic attenuation with frequency.

5.3 SAW process steps - fabrication

Optical Lithography and electron beam lithography are two primarily used techniques for SAW device fabrication. The required metal lines width and hence the frequency of operation decides the process used for fabrication. Diffraction effects limit the maximum frequency possible with optical lithography to around 800 MHz. Hence, higher frequency devices make use of electron beam lithography.

The SAW device was fabricated using the conventional two-step optical lithographic process. The critical dimensions of the first mask for creating the IDT patterns was 4 μm and the metal pads had a critical dimension of 100 μm followed by evaporation and lift off. Fig 55 shows the SAW device fabrication steps.

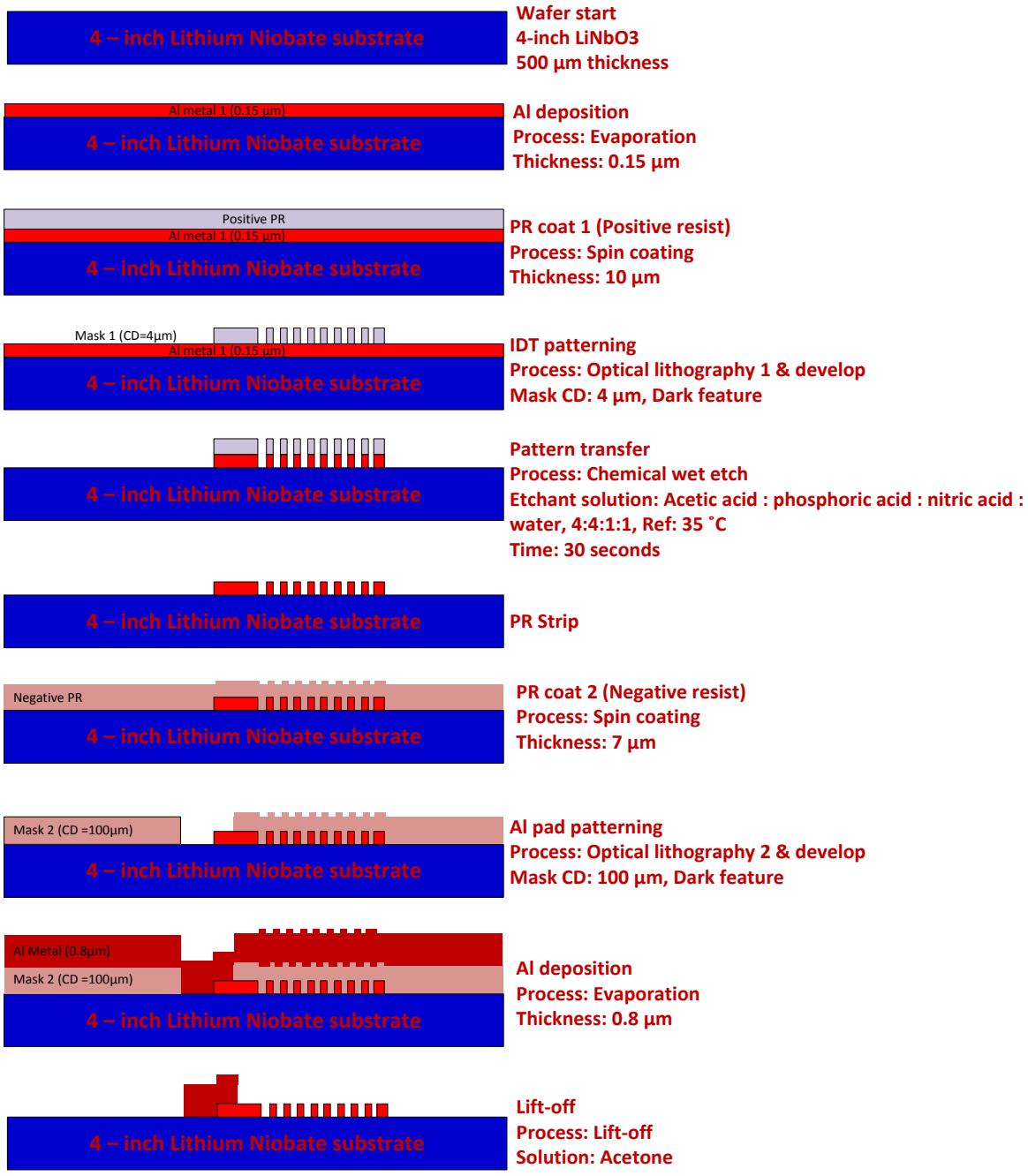

Figure 55: SAW fabrication process

Fig 56 shows the image of our fabricated devices.

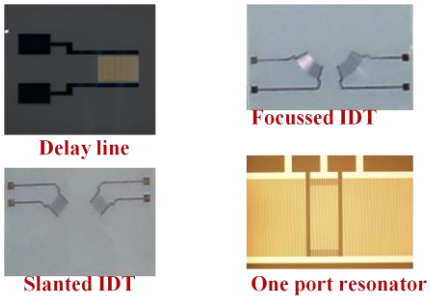

Figure 56: Fabricated IDT structures.

5.4 SAW device characterization

Fig 57 shows our device structure with PDMS designs fabricated for the micropump experiment.

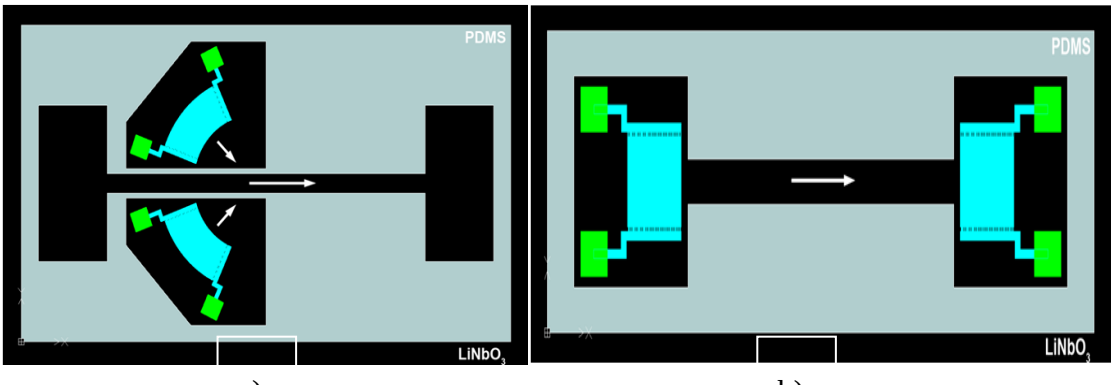

Figure 57: SAW devices for droplet actuation a) Focussed IDT b) Delay line

The E5061B ENA Series Network Analyzer Agilent technology was used for characterizing the SAW devices. Fig 58 shows the measured S11 characteristic of a delay line designed for a frequency of 100 MHz with 50 pairs of IDT, 2 mm long Al fingers and periodicity (2d) of 38.4 µm. The measured resonance frequency is around 98.2 MHz; the slight shift from the designed frequency can be because of the fabrication process errors. By observing the IDT pattern under the microscope shows slight over etching of the IDT, which can be the reason for the deviation in the frequency. The center frequency as obtained from the reflection characteristics is the frequency used to observe the SAW pumping effect.

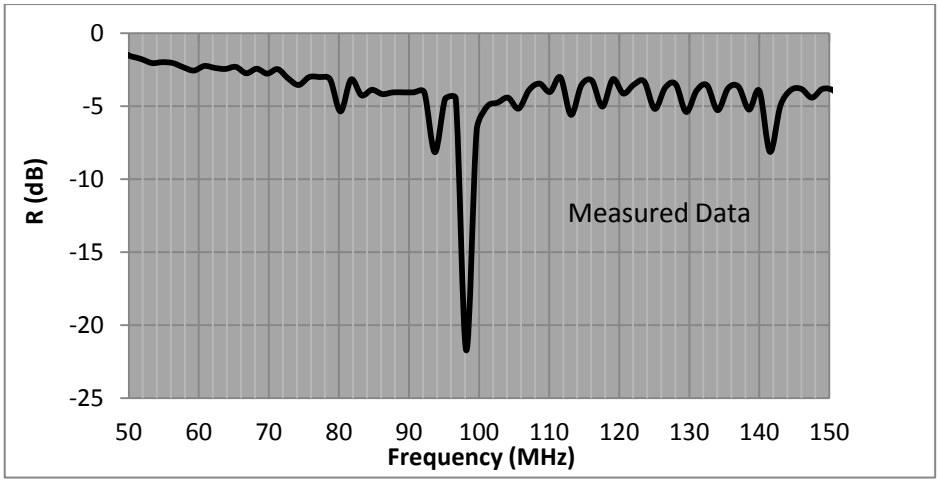

Figure 58: Radio frequency (RF) power reflected by IDT as a function of frequency.

Even though the higher order harmonics shows a significant reflection, they do not create sufficient acoustic streaming effect. This is due to the lower insertion loss compared to the harmonics, where there is significant bulk wave [38].

5.5 SAW pump testing setup

For the current work, the SAW pump experiment was done on an open channel without any surface treatment. These tests were used to study the droplet motion on the substrate. These results will be used to compare against droplet motion on surface with hydrophobic coatings like Octadecyltrichlorosilane (OTS). So as expected the current tests would require a larger voltage to pump the droplets due to higher surface forces acting on untreated $LiNbO_3$ surface given by the Eq.5-4[63]

$$F_s = \gamma_{LG}(1 + cos\theta)2\pi R sin\theta \qquad (5\text{–}4)$$

Where R is the droplet radius,θ is the droplet contact angle and γ_{LG} denotes the liquid-gas surface free energy.

The RF signal from an HP E4433B signal generator mixed with the burst signal generated from an Agilent Technologies 33250A is fed into a pulsed power amplifier giving a power

gain of almost 27 dB. Fig 59 shows the test setup and Fig 60 explains the block diagram of the test bench. Deionised water droplets with sizes ranging from 0.5-10 μL were released using Eppendorf micropipette. Droplet movement was measured using Olympus SZ61 stereomicroscope attached to a video camera.

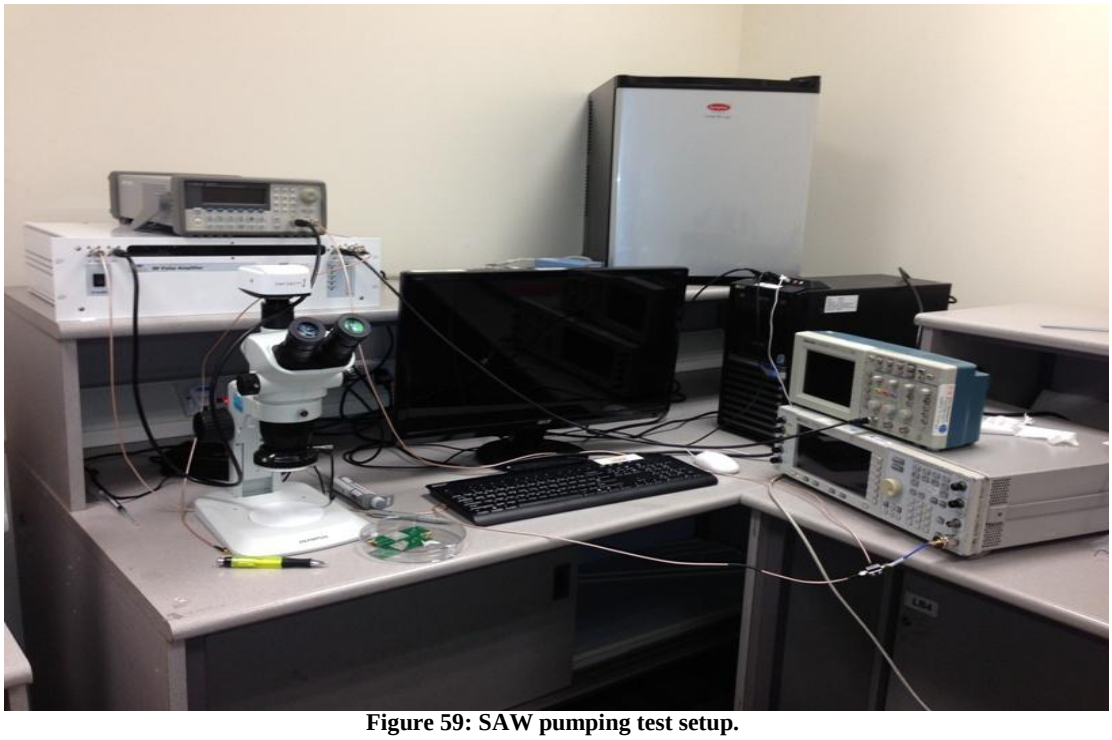

Figure 59: SAW pumping test setup.

.

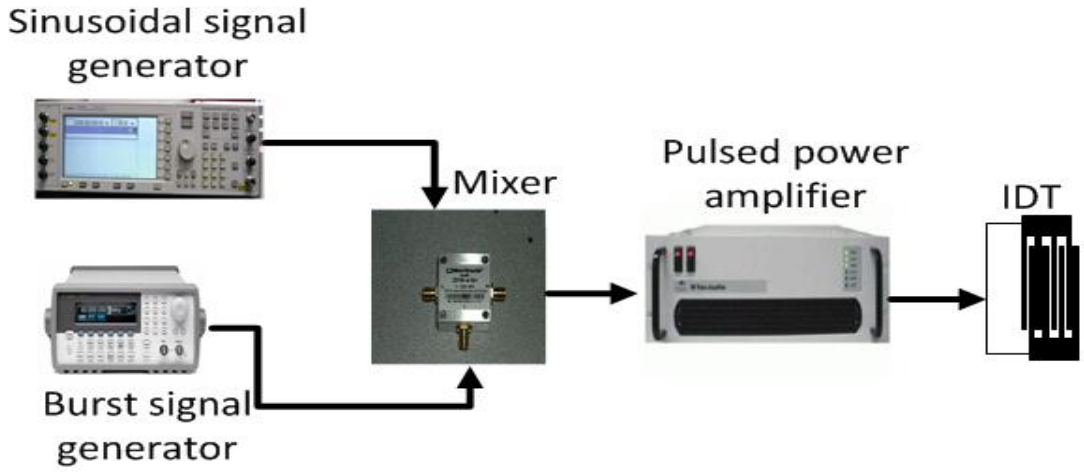

Figure 60: Block representation of the SAW pumping experiment.

5.5.1 SAW pump testing results

The testing which was carried on initially with open channels and a continuous signal excitation has resulted in droplet evaporation without any pumping effects as was mentioned in previous works [64]. Applying pulsed excitation to the droplet overcomes the above-mentioned problem with a precise control of the droplets position and distance. As mentioned above, there was no surface treatment to increase the hydrophobic nature of the substrate. Hence, the required electrical excitation voltage is higher compared to surface treated ones.

5.5.1.1 Droplet distance with time plot

This plot is the basis for computing the velocity of the droplet. The commercial software ImageJ [65] was used to extract the distance for various times (frames). The calculation was done for distinct times from droplet excitation. The time instants were adjusted so that closed points were obtained, to minimize error in the calculation of velocity from the slope of the distance-time curve.

A 1 μL drop excited with a voltage of 56 V produces a velocity of about 0.503cm/sec. The burst period was 10 msec. Fig 61, shows the distance-time curve used to find the velocity. From the curve, we find that the droplet has certain inertia, which increases the time taken for the droplet to move at relatively lower voltages. Using Matlab, we found the slope along the curve and used the *mean* function to compute the average velocity for the curves.

The curve shown in Fig 61 was plotted for different droplet size ranging from 0.5 to 10 μL; the resultant velocity profile obtained is shown in Fig 62.

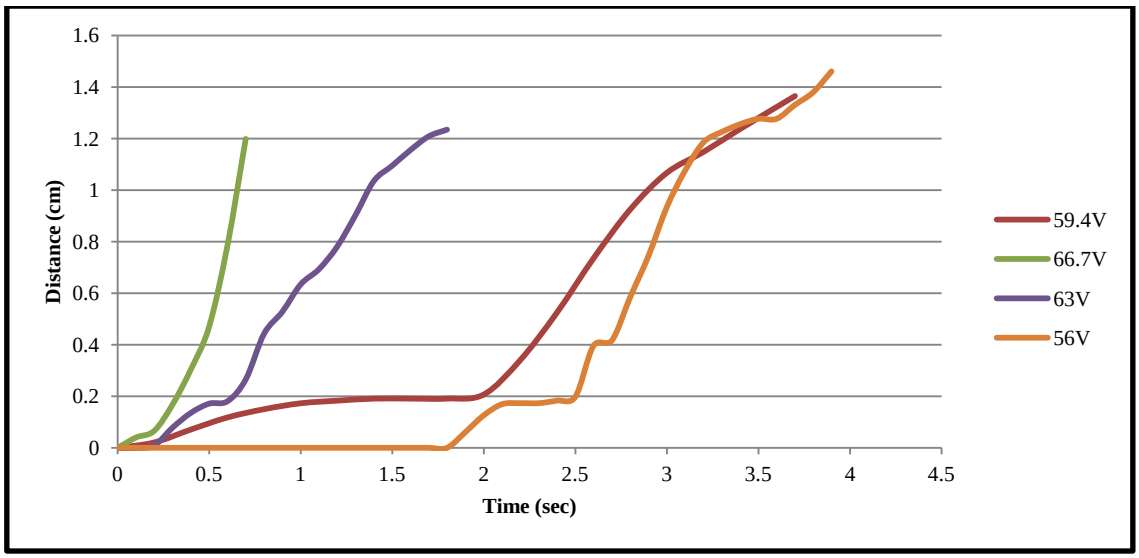

Figure 61: Distance vs. time plot for a 1 µL droplet as function of input excitation

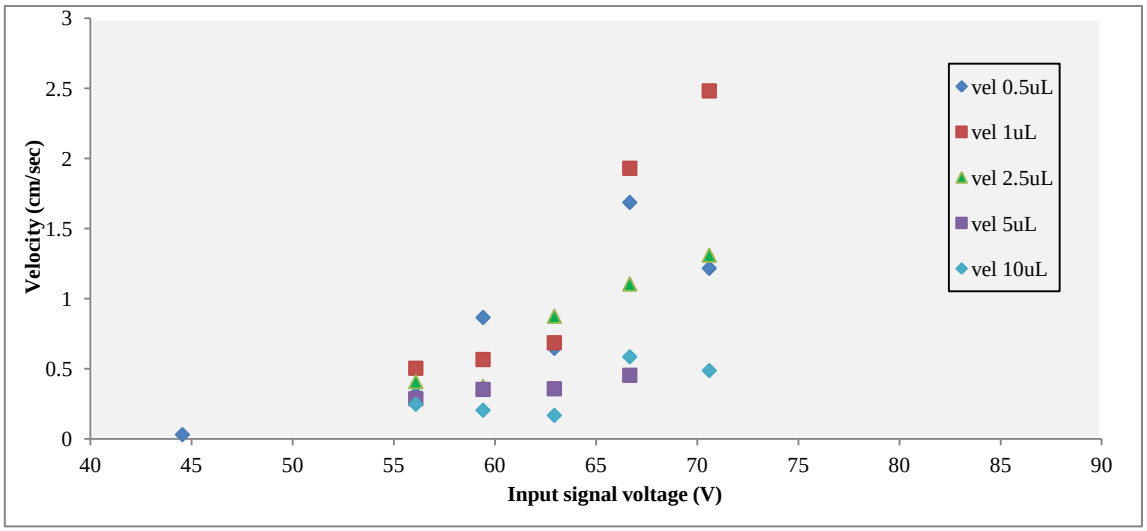

Figure 62: Droplet velocity vs. signal voltage for different droplet sizes

Explanation of the velocity curves:

From the velocity profile in Fig 61, there are two observations made:

1. For any droplet size, the general trend is an increasing velocity with increasing signal voltage. However, the velocity profile is not linear over the full range of input voltages. A similar non linear behaviour for the drop velocity with acoustic

displacement is shown in other works[66]. However, some other works shows a linear velocity increase[67] with signal voltage. A fundamental explanation for the droplet motion does not exist until now. Since the other works mentioned, made use of a hydrophobic coating. The same has to be done in our experiment to prove the behaviour.

The 10 μL drop displayed a lower velocity at 70 V; this can be due to change in surface property during course of time of the experiment. However, this effect needs to be validated after the hydrophobic coating is applied, as this can cause difficulties in practical system implementations.

2. There is an increase in the droplet velocity for a 1 μL drop when compared with a 0.5 μL. An explanation for the droplet velocity with varying size was given in [66]. According to which, there is an intermediate droplet volume where the maximum drop velocity is obtained. In case of a very small droplet, a significant part of the acoustic wave propagates after the drop with only a small part of it transferred into the drop. Larger drops use the energy to cause droplet displacement and deformation. Still larger drops possess large inertia, which reduces their velocity.
3. The attenuation length of the longitudinal component of the wave in the solid medium determines the droplets optimal size. This is related to the imaginary component in the complex Rayleigh wavenumber.

   The droplets shapes was deformed and there was droplet breakup involved, during testing in an untreated substrate and is shown in Fig 63

Further works involving surface treatment should be done to study the improvements obtained. This can predict and even used for analyzing the issues towards practical micropumps using surface acoustic waves. Future works on microfluidic channels, which

enclose the liquid droplets, may be of help to prevent evaporation, which is present in the open channels.

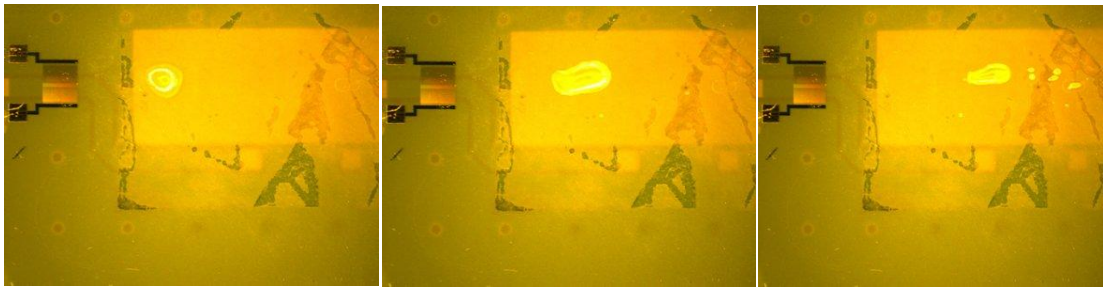

Figure 63: Sequential top views of droplet displacement in the substrate without surface treatment.

This chapter discusses the effects of SAW device and PDMS microchannels on the acoustic wave. The effects of various parameters like frequency, number of IDT and various device geometries on acoustic streaming is simulated using ANSYS. Further, we have come up with a simplified model instead of the complex prony series analysis for studying the effect of PDMS on acoustic attenuation. This can be used in the future works to design various microchannel architectures and study its effect on SAW micropumping. The SAW devices were fabricated, characterized and tested for micropumping of droplets on an open channel. The droplet motion was observed, with a velocity of around 2 cm/sec (Fig 62).

Chapter 6 Conclusion and Future Works

6.1 Conclusion

The main objectives of the thesis were- to derive an equivalent circuit model for the SAW sensor and use it to design and simulate the readout circuit architecture and secondly to implement a SAW micropump considering the effects of acoustic attenuation due to the microchannel.

An equivalent electrical model was derived with the analytical equations and FEM simulation. This model was used in the design and simulation of the readout circuit, in CMOS 0.18 μm technologies. It consists of an oscillator in the pierce oscillator topology. The drifts in the output frequency due to temperature changes was eliminated by employing a reference SAW device, which is free from any biological events. Thus, combining the output from the reference and active SAW device using a mixer discarded the environmental effects. A low pass filter using the Sallen-Key architecture was designed, which selects the desired low frequency component, and converts it into a square wave using a comparator for the frequency counter.

The effects of the PDMS material on the acoustic attenuation were studied and various IDT structures were simulated and fabricated to study its effect on droplet actuation on an open channel. The fabrication process along with the results of the droplet pumping experiment was presented.

6.2 Future works

The current work is a part of the project to build a microfluidic platform for implementing future microfluidic applications. The pump and the sensor form two of the main

components towards achieving the whole system. The further works will involve development of the micropump system with surface treatment and microchannels. The associated portable electronics for actuation will also be developed. This will follow implementing the other modules like -mixing, separation and concentration. The final aim would be to integrate these structures in a common substrate, to make them suitable for a point-of-care application.

Authors Publication & Awards

1. Rahul Kishor, Yuanjin Zheng, Zhenfeng Wang, Seah Daphne, Haijing Lu, Huanming Xia, "Frequency and Amplitude Effects on Microdroplet Displacement by Surface Acoustic Waves", International Symposium on Microchemistry and Microsystems, 2013 (accepted).
2. Rahul kishor, Zheng Yuanjin, "A uniform SAW based biosensing platform with integrated micropumping on a common susbstrate", Lab on a chip, 2013 (to be submitted).
3. Best Paper Award Certificate for the paper presented at the Workshop on Microfluidics for Biomedical Applications held in Singapore on 14th December 2012.

Reference

[1] P. Yager, T. Edwards, E. Fu, K. Helton, K. Nelson, M. R. Tam, *et al.*, "Microfluidic diagnostic technologies for global public health," *Nature*, vol. 442, p. 31, 2006.

[2] D. J. Laser and J. G. Santiago, "A review of micropumps," *J. Micromech. Microeng*, vol. 14 2004.

[3] S. Haeberle and R. Zengerle, "Microfluidic platforms for lab-on-a-chip applications," *Lab on a Chip*, vol. 7, pp. 1094-1110, 2007.

[4] ANSYS. Ansys 12.0 Documentation. *Inc. Theory Reference*.

[5] X. Guanshui, "Finite element analysis of second order effects on the frequency response of a SAW device," in *Ultrasonics Symposium, 2000 IEEE*, 2000, pp. 187-190 vol.1.

[6] E. de Boer and R. R. Beumer, "Methodology for detection and typing of foodborne microorganisms," *International Journal of Food Microbiology*, vol. 50, pp. 119-130, 1999.

[7] J. Meng and M. P. Doyle, "Introduction. Microbiological food safety," *Microbes and Infection*, vol. 4, pp. 395-397, 2002.

[8] V. Velusamy, K. Arshak, O. Korostynska, K. Oliwa, and C. Adley, "An overview of foodborne pathogen detection: In the perspective of biosensors," *Biotechnology Advances*, vol. 28, pp. 232-254, 3// 2010.

[9] N. Moll, E. Pascal, D. H. Dinh, J.-P. Pillot, B. Bennetau, D. Rebière, *et al.*, "A Love wave immunosensor for whole E. coli bacteria detection using an innovative two-step immobilisation approach," *Biosensors and Bioelectronics*, vol. 22, pp. 2145-2150, 4/15/ 2007.

[10] D. R. Davies and S. Chacko, "Antibody structure," *Accounts of Chemical Research*, vol. 26, pp. 421-427, 1993/08/01 1993.

[11] B. Leca-Bouvier and L. J. Blum, "Biosensors for Protein Detection: A Review," *Analytical Letters*, vol. 38, pp. 1491-1517, 2005/07/01 2005.

[12] B. Liedberg, C. Nylander, Lundstr, ouml, and I. m, *Biosensing with surface plasmon resonance--how it all started* vol. 10, 1995.

[13] J. Homola, S. S. Yee, and G. Gauglitz, "Surface plasmon resonance sensors: review," *Sensors and Actuators B: Chemical*, vol. 54, pp. 3-15, 1999.

[14] G. Sauerbrey, "Verwendung von Schwingquarzen zur Wägung dünner Schichten und zur Mikrowägung," *Zeitschrift für Physik A Hadrons and Nuclei*, vol. 155, pp. 206-222, 1959.

[15] J. Waswa, J. Irudayaraj, and C. DebRoy, "Direct detection of E. Coli O157:H7 in selected food systems by a surface plasmon resonance biosensor," *LWT - Food Science and Technology*, vol. 40, pp. 187-192, 3// 2007.

[16] M. Varshney, L. Yang, X.-L. Su, and Y. Li, "Magnetic Nanoparticle-Antibody Conjugates for the Separation of Escherichia coli O157:H7 in Ground Beef," *Journal of Food Protection*, vol. 68, pp. 1804-1811, // 2005.

[17] D. S. Ballantine, Jr., R. M. White, S. J. Martin, A. J. Ricco, G. C. Frye, E. T. Zellars, *et al.*, "Acoustic Wave Sensors - Theory, Design, and Physico-Chemical Applications," ed: Elsevier.

[18] R. Peach, "On the existence of surface acoustic waves on piezoelectric substrates," *Ultrasonics, Ferroelectrics and Frequency Control, IEEE Transactions on*, vol. 48, pp. 1308-1320, 2001.

[19] R. Lucklum and P. Hauptmann, "Acoustic microsensors—the challenge behind microgravimetry," *Analytical and Bioanalytical Chemistry*, vol. 384, pp. 667-682, 2006.

[20] J. W. Grate and G. C. Frye, "Acoustic Wave Sensors," *Sensors Update*, vol. 2, pp. 37-83, 1996.

[21] G. S. Calabrese, H. Wohltjen, and M. K. Roy, "Surface acoustic wave devices as chemical sensors in liquids. Evidence disputing the importance of Rayleigh wave propagation," *Analytical Chemistry*, vol. 59, pp. 833-837, 1987/03/01 1987.

[22] V. Michael J, "Acoustic wave sensors and their technology," *Ultrasonics*, vol. 36, pp. 7-14, 1998.

[23] M. Tom-Moy, R. L. Baer, D. Spira-Solomon, and T. P. Doherty, "Atrazine measurements using surface transverse wave devices," *Analytical Chemistry*, vol. 67, pp. 1510-1516, 1995/05/01 1995.

[24] G. Kovacs, G. W. Lubking, M. J. Vellekoop, and A. Venema, "Love waves for (bio)-chemical sensing in liquids," in *Ultrasonics Symposium, 1992. Proceedings., IEEE 1992*, 1992, pp. 281-285 vol.1.

[25] D. J. Laser and J. G. Santiago, "A review of micropumps," *Journal of Micromechanics and Microengineering*, vol. 14, p. R35, 2004.

[26] T. Gerlach and H. Wurmus, "Working principle and performance of the dynamic micropump," *Sensors and Actuators A: Physical*, vol. 50, pp. 135-140, 1995.
[27] N.-T. Nguyen, X. Huang, and T. K. Chuan, "MEMS-Micropumps: A Review," *Journal of Fluids Engineering*, vol. 124, pp. 384-392, 2002.
[28] A. Nisar, N. Afzulpurkar, B. Mahaisavariya, and A. Tuantranont, "MEMS-based micropumps in drug delivery and biomedical applications," *Sensors and Actuators B: Chemical*, vol. 130, pp. 917-942, 2008.
[29] L. Yeo and J. R. Friend, "Ultrafast microfluidics using surface acoustic waves," *Biomicrofluidics*, vol. 3, p. 012002, 2009.
[30] Z. Guttenberg, H. Muller, H. Habermuller, A. Geisbauer, J. Pipper, J. Felbel, *et al.*, "Planar chip device for PCR and hybridization with surface acoustic wave pump," *Lab on a Chip*, vol. 5, pp. 308-317, 2005.
[31] A. Renaudin, P. Tabourier, J.-C. Camart, and C. Druon, "Surface acoustic wave two-dimensional transport and location of microdroplets using echo signal," *Journal of Applied Physics*, vol. 100, pp. 116101-116101-3, 2006.
[32] A. Wixforth, "Acoustically driven planar microfluidics," *Superlattices and Microstructures*, vol. 33, pp. 389-396, 2003.
[33] D. L. T. Bell, Jr. and R. C. M. Li, "Surface-acoustic-wave resonators," *Proceedings of the IEEE*, vol. 64, pp. 711-721, 1976.
[34] S.-M. Chang, H. Muramatsu, C. Nakamura, and J. Miyake, "The principle and applications of piezoelectric crystal sensors," *Materials Science and Engineering: C*, vol. 12, pp. 111-123, 2000.
[35] E. J. Staples, "UHF Surface Acoustic Wave Resonators," in *28th Annual Symposium on Frequency Control. 1974*, 1974, pp. 280-285.
[36] E. K. Sittig and G. A. Coquin, "Filters and Dispersive Delay Lines Using Repetitively Mismatched Ultrasonic Transmission Lines," *Sonics and Ultrasonics, IEEE Transactions on*, vol. 15, pp. 111-118, 1968.
[37] G. L. Matthaei, B. P. O'Shaughnessy, and F. Barman, "Relations for Analysis and Design of Surface-Wave Resonators," *Sonics and Ultrasonics, IEEE Transactions on*, vol. 23, pp. 99-106, 1976.
[38] C. Campbell, *Surface Acoustic Wave Devices for Mobile and Wireless Communications*, 1998.
[39] K. T., "Finite Element Analysis of Surface Acoustic Wave Resonators," Master of Science, Department of Electrical Engineering, University of Saskatchewan, 2006.
[40] Y. Yook-Kong, "Analysis of periodic structures for BAW and SAW resonators," in *Ultrasonics Symposium, 2001 IEEE*, 2001, pp. 781-790 vol.1.
[41] D. Morgan, *Surface Acoustic Wave Filters with applications to electronic communication and signal processing*, Second ed.: Elsevier Ltd, 2007.
[42] R. F. Mitchell and D. W. Parker, "Synthesis of acoustic-surface-wave filters using double electrodes," *Electronics Letters*, vol. 10, pp. 512-512, 1974.
[43] W. H. Haydl, P. Hiesinger, R. S. Smith, B. Dischler, and K. Heber, "Design of Quartz and Lithium Niobate SAW Resonators Using Aluminum Metallization," in *30th Annual Symposium on Frequency Control. 1976*, 1976, pp. 346-357.
[44] P. S. Cross, W. H. Haydl, and R. S. Smith, "Design and applications of two-port SAW resonators on YZ-lithium niobate," *Proceedings of the IEEE*, vol. 64, pp. 682-685, 1976.
[45] M. Hofer, N. Finger, G. Kovacs, J. Schoberl, S. Zaglmayr, U. Langer, *et al.*, "Finite-element simulation of wave propagation in periodic piezoelectric SAW structures," *Ultrasonics, Ferroelectrics and Frequency Control, IEEE Transactions on*, vol. 53, pp. 1192-1201, 2006.
[46] R. Lucklum and F. Eichelbaum, "Interface Circuits for QCM Sensors Piezoelectric Sensors." vol. 5, A. Janshoff and C. Steinem, Eds., ed: Springer Berlin Heidelberg, 2007, pp. 3-47.
[47] M. von Schickfus, R. Stanzel, T. Kammereck, D. Weiskat, W. Dittrich, and H. Fuchs, "Improving the SAW gas sensor: device, electronics and sensor layer," *Sensors and Actuators B: Chemical*, vol. 19, pp. 443-447, 1994.
[48] J. W. M. R. a. C. Plett, *Radio Frequency Integrated Circuit Design (RFIC)*: Artech House Publishers, 2010
[49] H. G. Dimopoulos, *Analog Electronic Filters Theory, Design and Synthesis*, 2012.
[50] T. Instruments. (2002, 12/5/2013). Analysis of the Sallen-Key Architecture. [Application report]. Available:

http://www.ti.com/analog/docs/litabsmultiplefilelist.tsp?literatureNumber=sloa024b&docCategoryId=1&familyId=1463
[51] D. H. Phillip Allen, *CMOS Analog Circuit Design* Second ed.: Oxford University Press, 2002
[52] B. Razavi, *Design of Analog CMOS Integrated Circuits*: McGraw-Hill 2001.
[53] T. Delbrück and A. V. Schaik, "Bias Current Generators with Wide Dynamic Range," *Analog Integrated Circuits and Signal Processing,* vol. 43, pp. 247-268, 2005.
[54] N. S. K. Chono, Y. Matsui, J. Kondoh, and S. Shiokawa, "Development of Novel Atomization System Based on SAW Streaming," *Jpn. J. Appl. Phys,* vol. 43, 2004.
[55] S. K. R. S. Sankaranarayanan and V. R. Bhethanabotla, "Design of efficient focused surface acoustic wave devices for potential microfluidic applications," *Journal of applied physics,* vol. 103, p. 064518, 2008.
[56] A. Sano, Y. Rlatsui, and S. Shiokawa, "A new manipulator based on surface acoustic wave streaming," in *Ultrasonics Symposium, 1997. Proceedings., 1997 IEEE*, 1997, pp. 467-470 vol.1.
[57] J. Kuncova-Kallio and P. J. Kallio, "PDMS and its Suitability for Analytical Microfluidic Devices," in *Engineering in Medicine and Biology Society, 2006. EMBS '06. 28th Annual International Conference of the IEEE*, 2006, pp. 2486-2489.
[58] J. C. McDonald and G. M. Whitesides, "Poly(dimethylsiloxane) as a Material for Fabricating Microfluidic Devices," *Accounts of Chemical Research,* vol. 35, pp. 491-499, 2002/07/01 2002.
[59] L. Johansson, J. Enlund, S. Johansson, I. Katardjiev, and V. Yantchev, "Surface acoustic wave induced particle manipulation in a PDMS channel—principle concepts for continuous flow applications," *Biomedical Microdevices,* vol. 14, pp. 279-289, 2012/04/01 2012.
[60] G. McHale, M. K. Banerjee, M. I. Newton, and V. V. Krylov, "Surface acoustic wave resonances in the spreading of viscous fluids," *Physical Review B,* vol. 59, pp. 8262-8270, 1999.
[61] D. S. Lin, X. F. Zhuang, S. H. Wong, M. Kupnik, and B. T. Khuri-Yakub, "Encapsulation of Capacitive Micromachined Ultrasonic Transducers Using Viscoelastic Polymer," *Journal of Microelectromechanical Systems,* vol. 19, pp. 1341-1351, Dec 2010.
[62] S. J. Martin, G. C. Frye, and S. D. Senturia, "Dynamics and Response of Polymer-Coated Surface-Acoustic-Wave Devices - Effect of Viscoelastic Properties and Film Resonance," *Analytical Chemistry,* vol. 66, pp. 2201-2219, Jul 15 1994.
[63] A. Kawai and K. Suzuki, "Effect of low surface tension liquid on pattern collapse analyzed by dynamical meniscus observation," in *Microprocesses and Nanotechnology Conference, 2005 International*, 2005, pp. 70-71.
[64] S. Girardo, M. Cecchini, F. Beltram, R. Cingolani, and D. Pisignano, "Polydimethylsiloxane-LiNbO3 surface acoustic wave micropump devices for fluid control into microchannels," *Lab on a Chip,* vol. 8, pp. 1557-1563, 2008.
[65] C. A. Schneider, W. S. Rasband, and K. W. Eliceiri, "NIH Image to ImageJ: 25 years of image analysis," *Nat Meth,* vol. 9, pp. 671-675, 2012.
[66] P. Brunet, M. Baudoin, O. B. Matar, and F. Zoueshtiagh, "Droplet displacements and oscillations induced by ultrasonic surface acoustic waves: A quantitative study," *Physical Review E,* vol. 81, p. 036315, 2010.
[67] X. Y. Du, M. E. Swanwick, Y. Q. Fu, J. K. Luo, A. J. Flewitt, D. S. Lee, *et al.*, "Surface acoustic wave induced streaming and pumping in 128° Y-cut LiNbO 3 for microfluidic applications," *Journal of Micromechanics and Microengineering,* vol. 19, p. 035016, 2009.